

A MEMS based Valveless Micropump for Biomedical Applications

by

Schalk Willem van der Merwe

*Thesis presented at the University of Stellenbosch in
partial fulfillment of the requirements for the degree*

of

Master of Science in Engineering



Department of Mechanical and Mechatronic Engineering
University of Stellenbosch
Private Bag X1, 7602 Matieland, South Africa

Supervisors:

Prof. A.A. Groenwold

Prof. G.D. Thiart

Dr. P. Loveday

March 2010

Declaration

By Submitting this thesis electronically, I declare that the entirety of the work contained therein is my own, original work, that I am the owner of the copyright thereof (unless to the extent explicitly otherwise stated) and that I have not previously in its entirety or in part submitted it for obtaining any qualification.

Signature:
S.W. van der Merwe

Date:

Copyright © 2010 University of Stellenbosch
All rights reserved

Abstract

A MEMS based Valveless Micropump for Biomedical Applications

S.W. van der Merwe

Department of Mechanical and Mechatronic Engineering

University of Stellenbosch

Private Bag XI, 7602 Matieland, South Africa

Thesis: MScEng (Mechatronic)

March 2010

The valveless micropump holds great potential for the biomedical community in applications such as drug delivery systems, blood glucose monitoring and many others. It is also a critical component in many a lab-on-a-chip device, which in turn promises to improve our treatment and diagnosis capabilities for diseases such as diabetes, tuberculosis, and HIV/AIDS.

The valveless micropump has attracted attention from researchers on the grounds of its simple design, easy manufacturability and sensitive fluid handling characteristics, which are all important in biomedical applications.

The pump consists of a pump chamber with a diffuser and nozzle on opposing sides of the pump chamber. The flow into the diffuser and nozzle is induced by an oscillating piezoelectric disc located on top of the pump chamber. The nozzle and diffuser rectify the flow in one direction, due to different pressure loss coefficients.

The design process however is complex. In this study, we investigate the characteristics of a diffuser / nozzle based micropump using detailed computational fluid dynamic (CFD) analyses. Significant parameters are derived using the Buckingham-Pi theorem. In part based on this, the respective shapes of the diffuser and of the nozzle of the micropump are selected for numerical investigation. Hence the influence of the selected parameters on the flow rate of the micropump is studied using three-dimensional transient CFD analyses. Velocity profiles from the CFD simulations are also compared to the Jeffery-Hamel solution for flow in a wedge shaped channel. Significant similarities exist between the data and the predicted Jeffery-Hamel velocity profiles near the exit of the diffuser.

Three different diffuser geometries were simulated at three frequencies. The flow rate and direction of flow are shown to be highly sensitive to inlet and outlet diffuser shapes, with the absolute flow rate varying by as much as 200% for the geometrical perturbations studied. Entrance losses at both the diffuser inlet and nozzle inlet appear to dominate the flow resistance at extremely laminar flow conditions with the average Reynolds number of $Re_{ave} \approx 500$.

Uittreksel

'n MEMS-gebaseerde Kleplose Mikropomp vir Biomediese Toepassings

S.W. van der Merwe

Departement Meganiese en Megatroniese Ingenieurswese

Universiteit Stellenbosch

Privaatsak X1, 7602 Matieland, Suid-Afrika

Tesis: MScIng (Megatronies)

Maart 2010

Die kleplose mikropomp hou groot potensiaal in vir die biomediese gemeenskap in toepassings soos medisyne dosering sisteme, bloed glukose monitering en baie ander. Dit is ook 'n kritiese komponent in "lab-on-chip" sisteme, wat belooft om die behandeling en diagnose van siektes soos suikersiekte, tuberkulose en MIV/VIGS te verbeter.

Die kleplose mikropomp het tot dusver die aandag van navorsers geniet as gevolg van sy eenvoudige ontwerp, maklike vervaardiging en sensitiewe vloeistof hantering. Hierdie kenmerke is krities in menige biomediese toepassings.

Die pomp bestaan uit 'n pompkamer met 'n diffusor en 'n mondstuk aan teenoorstaande kante van die pompkamer. Vloei in die diffusor en mondstuk in word geïnduseer deur 'n ossillerende piëso-elektiese skyf wat bo-op die pompkamer geleë is. Weens verskillende drukverlies koëffisiënte van die diffusor en die mondstuk word die vloei in een rigting gerig.

Die ontwerp-proses is egter kompleks. In hierdie studie word die eienskappe van die diffusor / mondstuk ondersoek deur gebruik te maak van gedetailleerde numeriese vloei-dinamiese analises. Belangrike parameters word afgelei deur gebruik te maak van die Buckingham-Pi teorema. Gedeeltelik gebaseer hierop word die onderskeidelike vorms van die diffusor en die mondstuk van die mikropomp geselekteer vir numeriese ondersoek. Gevolglik word die invloed van die geselekteerde parameters op die vloei tempo van die mikropomp ondersoek deur gebruik te maak van drie-dimensionele tyd afhanklike numeriese vloei-dinamiese analises. Snelheids profiele van hierdie simulaties word vergelyk met die Jeffrey-Hamel oplossing vir die vloei in 'n wigvormige kanaal. Daar is oorwegende ooreenkomstighede tussen hierdie data en die voorspelde Jeffrey-Hamel snelheids profiele veral by die uitgang van die diffusor.

Drie verskillende diffusor vorms is by drie frekwensies gesimuleer. Daar is bewys dat die vloei tempo en vloei rigting baie sensitief is vir inlaat- en uitlaat diffusor vorms en dat die absolute vloei tempo kan varieer met soveel as 200% vir die geometriese verstuurings wat ondersoek is. Inlaat verliese by beide die diffusor inlaat en die mondstuk inlaat, blyk om die vloei weerstand te domineer waar die vloei uiters laminêr is met 'n gemiddelde Reynolds getal van $Re_{gem} \approx 500$

Acknowledgements

I would like to express my sincere gratitude to the following people and organizations who have contributed to making this work possible:

- The CSIR for funding the research.
- My study leader Prof Albert Groenwold of the University of Stellenbosch, Dr Philip Loveday of the CSIR and Prof Gerrie Thiart of the University of Stellenbosch as co-study leaders.
- Theuns Dirkse van Schalkwyk for his manufacturing facilities and inputs on the manufacturing.

Contents

Declaration	i
Abstract	ii
Uittreksel	iii
Acknowledgements	iv
Contents	v
List of Figures	viii
List of Tables	xii
Nomenclature	xiii
1 Introduction	1
1.1 Definition of MEMS	1
1.2 Problem statement	1
1.3 Objectives	2
1.4 Overview	2
2 Background and literature review	3
2.1 MEMS	3
2.1.1 Applications of MEMS	3
2.1.2 Advantages of MEMS and bio-MEMS	4
2.2 Literature review of micropump design	4
2.2.1 Origins of micropump design	5
2.2.2 Actuation sources	5
2.2.3 Types of micropumps	9
2.2.4 Mechanical micropumps	9
2.2.5 Non-mechanical micropumps	13
3 Micro manufacturing technologies and materials	16
3.1 Materials in bio-MEMS	16
3.1.1 Silicon	17
3.1.2 PDMS	17

3.2	Manufacturing techniques for MEMS	18
3.2.1	Deposition processes	18
3.2.2	Photolithography	18
3.2.3	Etching processes	19
3.2.4	Wafer bonding	20
3.2.5	Surface micromachining	21
4	Micropump design	23
4.1	Design phases	23
4.2	Problem statement	23
4.3	Concept evaluation	24
4.3.1	Pump mechanism	25
4.3.2	Actuation mechanism	25
4.4	Final concept	26
5	Theoretical model	29
5.1	Scaling down	29
5.2	Governing equations of microfluidics	30
5.2.1	Continuity equation	30
5.2.2	Navier-Stokes equation	31
5.3	Microchannels	32
5.4	Diffusers and nozzles	33
5.4.1	Jeffery-Hamel flow in a wedge-shaped region	35
5.4.2	Micropump efficiency	37
5.4.3	Experimental analysis	40
5.4.4	Dimensional analysis using Buckingham π -theorem	40
6	Numerical simulations	44
6.1	Method	44
6.2	Model	45
6.2.1	Model setup: Two-dimensional	45
6.2.2	Model setup: Three-dimensional	46
6.3	Two-dimensional analysis	47
6.3.1	Results of two-dimensional analysis	49
6.4	Three-dimensional analysis	50
6.4.1	Sharp edged diffuser/nozzle configuration	52
6.4.2	Round edged diffuser/nozzle configuration	55
6.4.3	Round edged diffuser and sharpened edge nozzle configuration	57
7	Results and discussion	59
7.1	CFD solution	59
7.1.1	Transient simulation of sharp edged diffuser and nozzle inlet	59
7.1.2	Transient simulation of rounded diffuser inlet edge model	65
7.1.3	Transient simulation of rounded diffuser inlet edge and sharpened nozzle inlet edge	69
7.2	Frequency dependence analysis	75

8	Conclusions and recommendations	76
8.1	Recommendations	77
8.1.1	Further analyses	77
8.1.2	Manufacturing recommendations	77
	List of References	78
A	Appendices	80
A.1	Manufacturing of micropump	80
A.2	Non-dimensionalised Navier-Stokes equation	80
A.3	Pressure contour plots	82
A.4	Velocity contour plots	88
A.5	Velocity profiles during flow cycle	92

List of Figures

2.1	Piezoelectric actuated peristaltic micropump and actuation sequence for displacing one stroke volume.	6
2.2	Electromagnetic actuation.	7
2.3	Electrostatic actuation.	7
2.4	Piezoelectric actuation.	7
2.5	Pneumatic actuation.	8
2.6	Shape memory alloy actuation.	8
2.7	Thermopneumatic actuation.	9
2.8	Bimetallic actuation.	10
2.9	Classification of micropumps according to their actuation mechanism and flow rectification methods.	10
2.10	(a) Illustration of a reciprocating pump with inlet and outlet valves, (b) outlet stroke, and (c) inlet stroke.	12
2.11	(a) An example of a positive displacement micropump, (b) piezoelectric stack actuation with disk valves in pump and supply mode, and (c) piezoelectric disk actuation with disk valves and silicon as piezoelectric mount [1].	14
2.12	Schematic presentation of a diffuser/nozzle type micropump.	15
2.13	Schematic presentation of the Tesla type microvalve [1].	15
2.14	Schematic illustration of electroosmotic flow through a pore with a finite EDL [2]. . .	15
3.1	Illustration of main planes in the cubic lattice of silicon [3].	17
3.2	Illustration of planes manipulation in the cubic lattice of silicon to form diffusers and nozzles for a valveless micropump [4].	18
3.3	Illustration of photo-patterning in positive and negative photoresist [3].	19
3.4	The difference between isotropic and anisotropic wet etching [3].	20
3.5	Direct wafer bonding process.	21
3.6	Anionic wafer bonding process.	21
3.7	Illustration of the surface micromachining process. [5]	22
4.1	Illustration of the different design aspects.	24
4.2	The basic design of a diffuser / nozzle type valveless micropump.	27
4.3	A flat walled diffuser / nozzle element.	28
5.1	Cube down sizing to illustrate scaling effect [3].	29
5.2	Velocity profile development from entrance region [6].	32

5.3	(a) Longitudinal view of microchannel with fully developed velocity profile, and (b) cross-sectional view of microchannel.	33
5.4	Newtonian shear stress distribution near the wall.	34
5.5	Schematic presentation diffuser flow [6].	35
5.6	Conical and flat-walled diffusers [7].	35
5.7	Stability map of a typical diffuser [8; 9].	36
5.8	Geometry and parameters of Jeffery-Hamel flow.	36
5.9	A numerical solution to Equation (5.4.7) for $Re\alpha > 0$ and $\alpha = 3.5^\circ$	38
5.10	A numerical solution to Equation (5.4.7) for $Re\alpha \leq 0$ and $\alpha = 3.5^\circ$	38
5.11	Typical diffuser performance map for flat walled diffuser under highly turbulent operating conditions [8].	41
5.12	Planar diffuser performance plot for a fully developed entrance boundary layer at various Reynolds numbers [10].	42
6.1	Two-dimensional layout of the diffuser element model.	45
6.2	Three dimensional layout of the micropump model.	46
6.3	A two-dimensional mesh of the diffuser section comprising of 12500 mesh elements.	48
6.4	Results for number of mesh elements vs flow rate for a two dimensional steady state analysis.	48
6.5	Steady state velocity magnitude contours for two dimensional diffuser flow.	49
6.6	Steady state velocity magnitude contours for two dimensional nozzle flow.	50
6.7	A meshed three-dimensional model showing the elements in the diffuser.	51
6.8	(a) An illustration of a diffuser model with sharp diffuser and nozzle inlet radii. (b) An illustration of a diffuser model with a rounded diffuser inlet edge and a sharp nozzle inlet edge. (c) An illustration of a diffuser model with a rounded diffuser inlet edge and a sharpened nozzle inlet edge.	52
6.9	Inlet and outlet flow rates for the sharp edged diffuser nozzle configuration exited at 10 Hz for 0.2 seconds and with $\Delta t = 1$ ms.	53
6.10	Inlet and outlet flow rates for the sharp edged diffuser nozzle configuration exited at 100 Hz for 0.02 seconds and with $\Delta t = 0.1$ ms.	54
6.11	Inlet and outlet flow rates for the sharp edged diffuser nozzle configuration exited at 1000 Hz for 0.002 seconds and with $\Delta t = 0.01$ ms.	54
6.12	Inlet and outlet flow rates for the rounded diffuser inlet and sharp nozzle inlet configuration exited at 10 Hz for 0.2 seconds and with $\Delta t = 1$ ms.	55
6.13	Inlet and outlet flow rates for the rounded diffuser inlet and sharp nozzle inlet configuration exited at 100 Hz for 0.02 seconds and with $\Delta t = 0.1$ ms.	56
6.14	Inlet and outlet flow rates for the rounded diffuser inlet and sharp nozzle inlet configuration exited at 1kHz for 0.002 seconds and with $\Delta t = 0.01$ ms.	56
6.15	Inlet and outlet flow rates for the rounded diffuser inlet and sharpened nozzle inlet configuration exited at 10 Hz for 0.2 seconds and with $\Delta t = 1$ ms.	57
6.16	Inlet and outlet flow rates for the rounded diffuser inlet and sharpened nozzle inlet configuration exited at 100 Hz for 0.02 seconds and with $\Delta t = 0.1$ ms.	58
6.17	Inlet and outlet flow rates for the rounded diffuser inlet and sharpened nozzle inlet configuration exited at 1000 Hz for 0.002 seconds and with $\Delta t = 0.01$ ms.	58
7.1	Flow rates for the three different diffuser / nozzle edge configurations vs frequency.	60

7.2	A two dimensional view of the velocity gradients around the diffuser inlet.	61
7.3	An illustration of the diffuser lengths where data were recorded.	61
7.4	A cross section of the diffuser showing the depths where data were recorded.	62
7.5	A comparison between the predicted Jeffery-Hamel velocity profiles and the calculated CFD velocity vectors for $x = 0 \mu\text{m}$, $t = 1.20 \text{ ms}$, @ 1 kHz and at three depths in the diffuser for the sharp edged model (see Figure 6.8(a)).	62
7.6	A comparison between the predicted Jeffery-Hamel velocity profiles and the calculated CFD velocity vectors for $x = 286 \mu\text{m}$, $t = 1.20 \text{ ms}$, @ 1 kHz and at three depths in the diffuser for the sharp edged model (see Figure 6.8(a)).	63
7.7	A comparison between the predicted Jeffery-Hamel velocity profiles and the calculated CFD velocity vectors for $x = 572 \mu\text{m}$, $t = 1.20 \text{ ms}$, @ 1 kHz and at three depths in the diffuser for the sharp edged model (see Figure 6.8(a)).	63
7.8	A comparison between the predicted Jeffery-Hamel velocity profiles and the calculated CFD velocity vectors for $x = 858 \mu\text{m}$, $t = 1.20 \text{ ms}$, @ 1 kHz and at three depths in the diffuser for the sharp edged model (see Figure 6.8(a)).	64
7.9	A comparison between the predicted Jeffery-Hamel velocity profiles and the calculated CFD velocity vectors for $x = 1144 \mu\text{m}$, $t = 1.20 \text{ ms}$, @ 1 kHz and at three depths in the diffuser for the sharp edged model (see Figure 6.8(a)).	64
7.10	A comparison between the predicted Jeffery-Hamel velocity profiles and the calculated CFD velocity vectors for $x = 0 \mu\text{m}$, $t = 1.20 \text{ ms}$, @ 1 kHz and at three depths in the diffuser for the rounded diffuser inlet edge model (see Figure 6.8(b)).	65
7.11	A comparison between the predicted Jeffery-Hamel velocity profiles and the calculated CFD velocity vectors for $x = 286 \mu\text{m}$, $t = 1.20 \text{ ms}$, @ 1 kHz and at three depths in the diffuser for the rounded diffuser inlet edge model (see Figure 6.8(b)).	66
7.12	A comparison between the predicted Jeffery-Hamel velocity profiles and the calculated CFD velocity vectors for $x = 572 \mu\text{m}$, $t = 1.20 \text{ ms}$, @ 1 kHz and at three depths in the diffuser for the rounded diffuser inlet edge model (see Figure 6.8(b)).	67
7.13	A comparison between the predicted Jeffery-Hamel velocity profiles and the calculated CFD velocity vectors for $x = 858 \mu\text{m}$, $t = 1.20 \text{ ms}$, @ 1 kHz and at three depths in the diffuser for the rounded diffuser inlet edge model (see Figure 6.8(b)).	67
7.14	A comparison between the predicted Jeffery-Hamel velocity profiles and the calculated CFD velocity vectors for $x = 1144 \mu\text{m}$, $t = 1.20 \text{ ms}$, @ 1 kHz and at three depths in the diffuser for the rounded diffuser inlet edge model (see Figure 6.8(b)).	68
7.15	A comparison between the predicted Jeffery-Hamel velocity profiles and the calculated CFD velocity vectors for $x = 0 \mu\text{m}$, $t = 1.20 \text{ ms}$, @ 1 kHz and at three depths in the diffuser for the rounded diffuser inlet edge and sharpened nozzle inlet edge model (see Figure 6.8(c)).	69
7.16	A comparison between the predicted Jeffery-Hamel velocity profiles and the calculated CFD velocity vectors for $x = 286 \mu\text{m}$, $t = 1.20 \text{ ms}$, @ 1 kHz and at three depths in the diffuser for the rounded diffuser inlet edge and sharpened nozzle inlet edge model (see Figure 6.8(c)).	70
7.17	A comparison between the predicted Jeffery-Hamel velocity profiles and the calculated CFD velocity vectors for $x = 572 \mu\text{m}$, $t = 1.20 \text{ ms}$, @ 1 kHz and at three depths in the diffuser for the rounded diffuser inlet edge and sharpened nozzle inlet edge model (see Figure 6.8(c)).	71

7.18	A comparison between the predicted Jeffery-Hamel velocity profiles and the calculated CFD velocity vectors for $x = 858 \mu\text{m}$, $t = 1.20 \text{ ms}$, @ 1 kHz and at three depths in the diffuser for the rounded diffuser inlet edge and sharpened nozzle inlet edge model (see Figure 6.8(c)).	71
7.19	A comparison between the predicted Jeffery-Hamel velocity profiles and the calculated CFD velocity vectors for $x = 1144 \mu\text{m}$, $t = 1.20 \text{ ms}$, @ 1 kHz and at three depths in the diffuser for the rounded diffuser inlet edge and sharpened nozzle inlet edge model (see Figure 6.8(c)).	72
7.20	A comparison between the predicted Jeffery-Hamel velocity profiles and the calculated CFD velocity vectors for nozzle flow in the rounded diffuser inlet model and the rounded diffuser inlet model with extension at the nozzle entrance.	72
7.21	Velocity profile plot of nozzle flow in the sharp nozzle inlet edge model near the nozzle entrance.	73
7.22	Velocity profile plot of nozzle flow in the sharpened nozzle inlet edge model near the nozzle entrance.	73
7.23	Velocity contour plot of the nozzle flow for the sharp nozzle inlet edge model.	74
7.24	Velocity contour plot of the nozzle flow for the sharpened nozzle inlet edge model.	74
A.1	Proposed manufacturing solution.	81
A.2	The diffuser and outlet of the micropump under $20\times$ magnification.	82
A.3	The top of the diffuser / nozzle, viewed with $20\times$ magnification.	83
A.4	Pressure contour plot of diffuser flow.	83
A.5	Pressure contour plot of nozzle flow.	84
A.6	Pressure contour plot @ 1 kHz.	84
A.7	Pressure contour plot @ 1 kHz.	85
A.8	Pressure contour plot @ 1 kHz.	85
A.9	Pressure contour plot @ 1 kHz.	86
A.10	Pressure contour plot @ 1 kHz.	86
A.11	Pressure contour plot @ 1 kHz.	87
A.12	Pressure contour plot @ 1 kHz.	87
A.13	Velocity magnitude contour plot @ 1 kHz.	88
A.14	Velocity magnitude contour plot @ 1 kHz.	89
A.15	Velocity magnitude contour plot @ 1 kHz.	89
A.16	Velocity magnitude contour plot @ 1 kHz.	90
A.17	Velocity magnitude contour plot @ 1 kHz.	90
A.18	Velocity magnitude contour plot @ 1 kHz.	91
A.19	Velocity magnitude contour plot @ 1 kHz.	91
A.20	Velocity profile in diffuser @ 1 kHz.	92
A.21	Velocity profile in diffuser @ 1 kHz.	93
A.22	Velocity profile in diffuser @ 1 kHz.	93
A.23	Velocity profile in diffuser @ 1 kHz.	94
A.24	Velocity profile in diffuser @ 1 kHz.	94
A.25	Velocity profile in diffuser @ 1 kHz.	95
A.26	Velocity profile in diffuser @ 1 kHz.	95

List of Tables

2.1	Characteristics of mechanical micropumps from literature [4; 11; 12; 13; 14; 15; 16; 17; 18; 19].	11
4.1	Evaluation of the pumping method against different weighted criteria.	26
4.2	Evaluation of the actuation method against different weighted criteria.	27
6.1	The exact values of mesh size vs flow rate, for diffuser and nozzle directions	49
7.1	Results of the three geometries as depicted in Figure 6.8 at three excitation frequencies.	60

Nomenclature

Abbreviations:

AIDS	Acquired immune deficiency syndrome
ASTM	American society for testing and materials
CNC	Computer numerical controlled
CFD	Computational fluid dynamics
CPU	Central processing unit
CVD	Chemical vapor deposition
DLP	Digital light projection
DMD	Digital mirror devices
EDL	Electric double layer
EHD	Electro-hydrodynamic
EOF	Electroosmotic flow
FDA	Food and drug administration
HPC	High performance computing
IC	Integrated circuit
I/O	Input - output
μ TAS	Micro total analysis system

MEMS	Micro-electro-mechanical systems
PDMS	Polydimethylsiloxane
PVD	Physical vapor deposition
SMA	Shape memory alloy
USD	United States Dollars

Symbols:

A	Cross-sectional area
AR	Area ratio
d	Hydraulic diameter
f	Oscillating frequency
g	Gravitational acceleration
H	Depth of flat-walled diffuser
K	Pressure loss coefficient
L	Length of diffuser
p	Hydrostatic pressure
Q	Volumetric flow rate
r_1	Radius of rounded entrance
Re	Reynolds number
Re_D	Reynolds number with regards to hydraulic diameter
s	Surface
t	Time

u	Axial velocity
V	Mean velocity
v	Volume
W	Width of flat-walled diffuser
x	Coordinate

Greek Symbols:

α	Diffuser angle
α_e	Kinetic energy correction factor
ε	Pump stroke efficiency
μ	Fluid viscosity
η_{nd}	Diffuser efficiency
θ	Diffuser half angle
ρ	Water density
ξ	Total pressure loss coefficient
ΔP	Frictional pressure loss
τ	Shear stress

Subscripts:

a	Atmosphere
c	Chamber
cs	Control surface

<i>cv</i>	Control volume
<i>d</i>	Diffuser
<i>e</i>	Diffuser outlet
<i>en</i>	Entrance
<i>ex</i>	Exit
<i>i</i>	Inlet
<i>n</i>	Nozzle
<i>o</i>	Outlet
<i>s</i>	Sum
<i>t</i>	Diffuser throat
<i>w</i>	Wall

Superscripts:

<i>t</i>	Total
----------	-------

Chapter 1

Introduction

During his famous speech, “*There is plenty of room at the bottom*” in 1959, world renown physicist Richard P. Feynman discussed the possibilities of micromachines and microrobots [20]. He envisioned a world made simpler by miniaturized systems. At that stage Feynman’s idea seemed farfetched, unattainable and impractical, but in 2004 the world wide investment in micro- and nanotechnology exceeded USD 3.5 billion [21]. Today we find MEMS in a large range of applications such as accelerometers in automobiles, micromirrors in DLP and a range of biomedical applications.

The past two decades have shown an explosive growth in research and development of bio-MEMS and μ TAS or Lab-on-a-Chip devices. The field emerged as a result of intergrating the well established technology of MEMS with that of bio-analytical chemistry [22]. These devices combine sensing mechanisms (physical, electrical, chemical or optical) with actuators and microfluidics. Micro-systems can mimic conventional sample handling techniques performed in hospitals and laboratories and holds great potential to enable both research and healthcare advances [1].

1.1 Definition of MEMS

MEMS was developed in the early 1980’s as an extension of microelectronics. MEMS is the technology of the very small. These devices generally range in size from a micrometer to a millimeter. At these small scales, our intuitive sense of physics may be deceiving, and thus we need to rely more heavily on CAD tools than on our intuition. Depending on the continent of origin, MEMS are sometimes referred to as micromechanics, micro machines and micro-system-technology (MST).

Due to MEMS’ large surface area to volume ratio, surface effects such as electrostatics and friction dominate over volume effects such as inertia (this effect is disused in detail in Section 5). MEMS devices are fabricated using modified silicon fabrication technologies. This fabrication process is also used to make electronics for IC’s and are described to some extent in Section 3.

1.2 Problem statement

Bio-MEMS refers to a special type of MEMS, where biological material is manipulated through analysis and measurements using scientific methods. The μ TAS chip is the preferred technol-

ogy for implementing Bio-MEMS. Bio-MEMS generally consists of micromixers, microflow sensors, microfilters and micropumps, the latter of which can be described as the heart of the μ TAS chip. MEMS and specifically bio-MEMS are currently a limited research area in South Africa due to the lack of funding and expertise in this area. The need for μ TAS is increasing in South Africa as a result of the increase of AIDS and diabetes among patients [23].

A major objective of the bio-MEMS and MEMS research is to develop a μ TAS capable of performing a wide variety of functions more effectively than possible by current standards. This means sensors, actuators and processors that will function in unison, to fulfill a specific scientific task.

The micropump is a key factor in the success of the μ TAS chip. By being able to provide an accurate volumetric flow rate and pump characteristics the micropump is an important factor in the design and efficiency of all Lab-on-a-Chip devices.

1.3 Objectives

The principal objective of this project is to conceptually evaluate a micropump for the biomedical environment capable of delivering a minimum volumetric flow rate of 2000 μ l/min. The secondary objective of the project is to determine the volumetric flow rate sensitivity of the micropump as a function of the geometry and other characteristic performance variables such as excitation frequency. The evaluation of specific parameters are done numerically and are compared to the literature and a theoretical model.

Supplementary to the design is the manufacturing of the micropump. A major necessity of the manufacturing is that the manufacturing processes utilized should be local and inexpensive. The main goal of the manufacturing is to prove the concept functions as intended and give qualitative feedback on the volumetric flow rate.

1.4 Overview

The design of the micropump is preceded by a literature study of MEMS, micropumps (Section 2) and manufacturing techniques (Section 3). The design of the micropump is discussed in Section 4, detailing the design process followed and concept evaluation.

The effects of down scaling on the fluid-dynamic governing equations are investigated in Section 5. The section utilizes the Buckingham π -theorem to determine the functional relationship between key design parameters. Section 5.4.1 derives the Jeffery-Hamel flow in a wedge shaped channel in polar coordinates. The solution is plotted for a range of $Re\alpha$ values.

In Section 6, a two-dimensional mesh dependence study precedes the three-dimensional CFD simulations. In this section the volumetric flow rate of three geometrically different micropumps are calculated using detailed three-dimensional CFD simulations.

In Section 7, the solution to the Jeffery-Hamel flow is compared to velocity profiles from CFD simulations. The section evaluates and discuss the sensitivity of the volumetric flow rate to parameter adjustments.

The conclusions follow in Section 8 to give the concluding remarks and recommendations. The appendices provides further CFD Results and give an overview of the manufacturing.

Chapter 2

Background and literature review

This section provides the background and advantages of MEMS and focus on microfluidics and the manufacturing techniques involved. Previous work in microfluidics and micropumps is discussed as part of a literature review.

2.1 MEMS

MEMS refer to devices that have a characteristic length ranging between 1 μm and 1 mm, and combines electrical and mechanical components, that are fabricated using IC batch-processing technologies [21]. This section provides the background of MEMS, bio-MEMS and the manufacturing technologies involved.

2.1.1 Applications of MEMS

This multidisciplinary field has experienced explosive growth during the last two decades. MEMS devices are found in a wide variety of applications and used mainly as sensors and actuators. Common applications include [21; 24]:

- Inkjet printers, which use piezoelectrics or bubble ejection to deposit ink on paper.
- Accelerometers in modern cars for airbag deployment in collisions.
- Keyless entry systems in luxury cars.
- MEMS gyroscopes are used in modern cars and other applications to detect yaw.
- Pressure sensors used in automobile tire pressure sensors and disposable blood pressure sensors.
- Bio-medical applications such as:
 - blood glucose monitoring,
 - retina replacements,
 - heart pacemakers,

- drug delivery systems,
 - reactors for separating biological cells,
 - manufacturing of nanoliters of chemicals,
 - development of artificial pancreas, and
 - lab-on-a-chip devices.
- Displays when used in DMD chips.
 - Micro heat exchangers for cooling electronic circuits in computers.
 - Optical switching technology is used in data communications.

2.1.2 Advantages of MEMS and bio-MEMS

Bio-MEMS utilize chemical, mechanical, electrical and neural functions of microstructures in ways that mimic or interact with the human body. Some of the specific advantages of Bio-MEMS are [25]:

- silicon which is generally used to manufacture micro components is bio-compatible,
- silicon surfaces can be microtextured to increase acceptance by the surrounding tissue,
- greater uniformity and reliability,
- reproducibility,
- miniaturized implants,
- fast response to inputs,
- ability to provide and receive an electrical stimulus,
- low power consumption,
- optical and electrical sensitivity,
- ability to integrate electronics, sensors and actuators (closed loop systems are possible),
- precision control,
- ability to interact with fluids (microfluidics, biochemical sensors, etc.), and
- ability to measure physiological signals as well as the ability to provide electrical impulses as for heart pace maker applications.

2.2 Literature review of micropump design

As mentioned in the preceding section, the advantages of MEMS and especially bio-MEMS provide the incentive for this literature study.

2.2.1 Origins of micropump design

The first documented reports of a miniaturized pump or micropump date back to as early as 1975, Tay [22]. The proposed concept was to be implanted into a human body, and consisted of two opposing piezoelectric disks that formed a cavity inbetween. The two piezoelectric disks acted on the fluid between them to generate a pressure in the fluid. The micropump was coupled to a solenoid valve to rectify the flow direction, and was designed to deliver a stroke volume of $0.2\mu\text{L}$. Realizing the potential of the micropump in industries such as heat transfer, biomedicine and printing, researchers continued their investigations in later years.

It was only in the early 1980's that the first micropump was manufactured using integrated circuit manufacturing techniques. The micropump was designed by J.G. Smits and was a peristaltic micropump with three active valves [22]. The micropump forced fluid in a direction by contracting each of its three active valves in a wave like sequence as seen in Figure 2.1. The work presented by Smits was genesis for the micropumps and micromanufacturing, and patents using IC manufacturing technologies surfaced in subsequent years.

In 1993, Stemme and Stemme designed and tested a valveless micropump based on the flow rectification property of diffusers [11]. The design proposed by Stemme and Stemme, was simple and offered advantages like low fabrication cost, reduced wear, increased valve reliability and less clogging of the valves, prevalent in most passive check valve models.

The design of micropumps have changed significantly throughout the years and currently we utilize various aspects of physics to move fluids through a micropump.

2.2.2 Actuation sources

All mechanical micropumps require an actuation source to provide a pressure differential or change in volume, to transfer fluid from one point to another. This section investigates the different actuation sources and how they are utilized within a mechanical micropump.

2.2.2.1 External actuators

This type of actuator is termed external because it is not integrated into the device as part of the manufacturing process. The actuator usually requires external components and other couplings to the micro device. The advantage of this system is that these actuators are capable of producing large forces and stroke displacements independent of each other. A disadvantage of using this type of actuator is that the actuator is usually larger than the micropump and significantly increases the system's volume.

2.2.2.2 Electromagnetic actuators

This actuation source works similar to a solenoid valve. It consists of a coil and a plunger as depicted in Figure 2.2. When current is passed through the coil a magnetic field produces a force on the ferromagnetic plunger which is coupled to a membrane. The advantage of using this actuator is that it can produce large stroke displacements and the force can be varied according to the current passed through the coil. The disadvantage of this system is that it is relatively large due to the size of the coils.

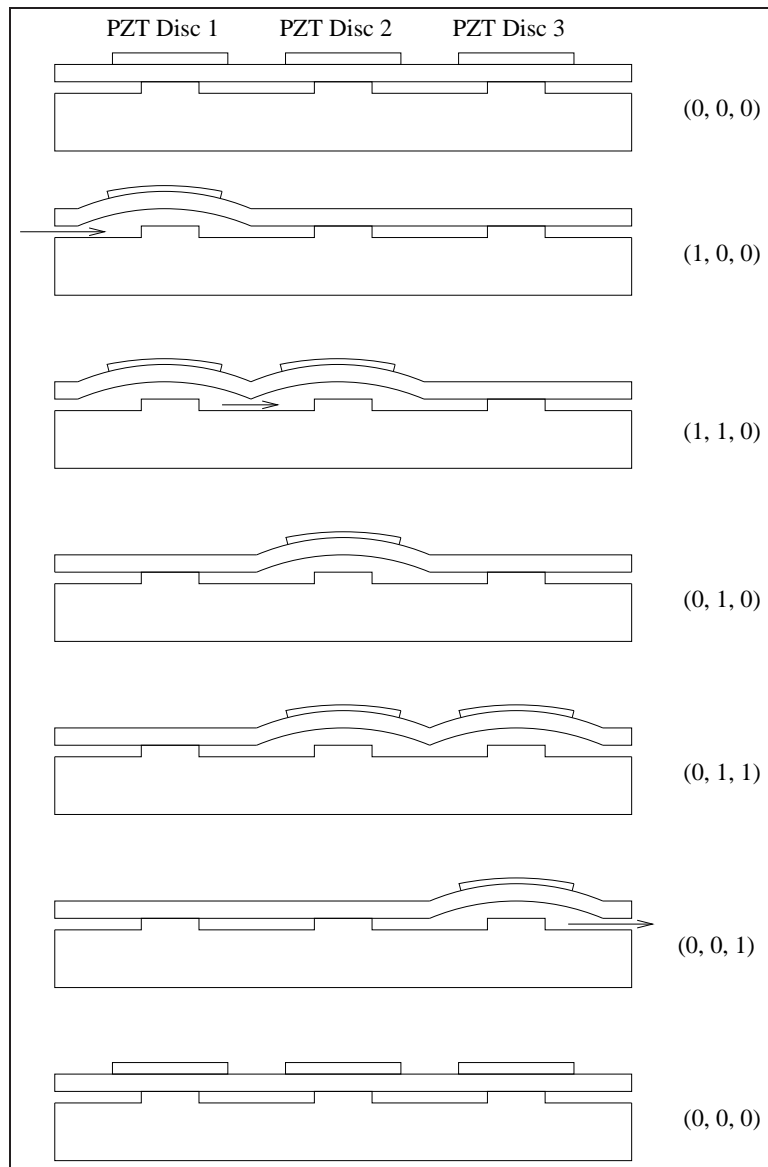


Figure 2.1: Piezoelectric actuated peristaltic micropump and actuation sequence for displacing one stroke volume.

2.2.2.3 Electrostatic actuators

The design of this actuator is based on the capacitive charging of two parallel plates when subjected to a voltage differential. One of the parallel plates can move under electrostatic force producing a displacement as depicted in Figure 2.3. The advantage of this system is low power consumption. The disadvantage is that the actuation force is directly proportional to the distance between the plates. Thus the pressure and stroke volume are tradeoffs in the design.

2.2.2.4 Piezoelectric actuators

This actuation technique is most commonly used when coupled with a membrane. Piezoelectric materials such as lead zirconate titanate (PZT) produce a mechanical displacement when

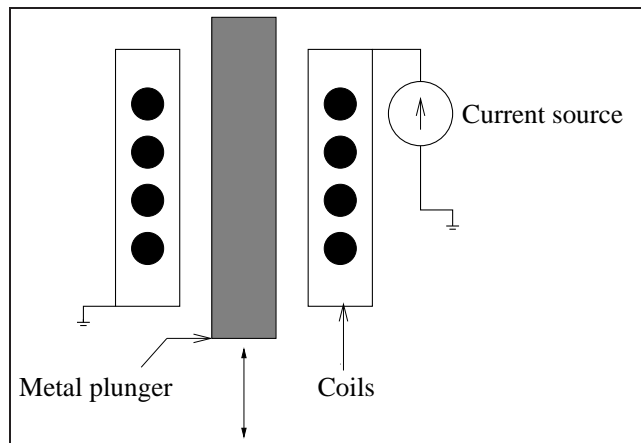


Figure 2.2: Electromagnetic actuation.

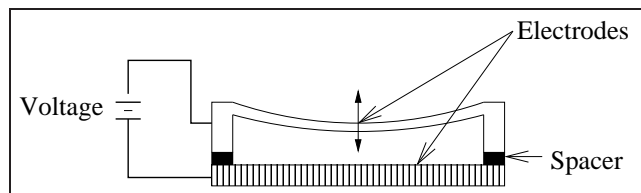


Figure 2.3: Electrostatic actuation.

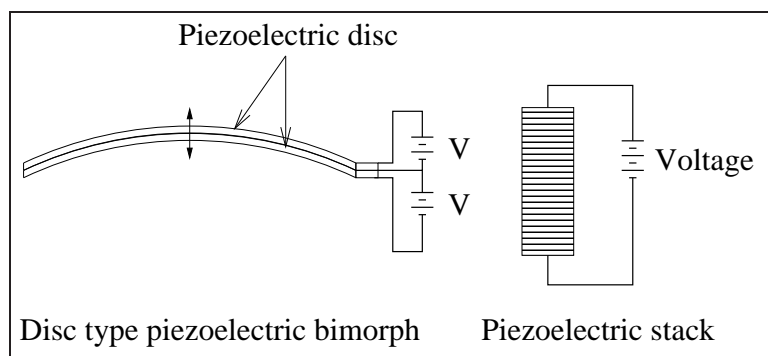


Figure 2.4: Piezoelectric actuation.

subjected to a voltage potential. The advantages of using this type of actuator is fast response times and large stroke displacements. The disadvantage of this actuation technique is that although the displacement is relatively large the force is low. The force of the actuator can be improved by using a stack actuator as depicted in Figure 2.4.

2.2.2.5 Pneumatic actuators

Pneumatic actuation uses pressurised gas to actuate a pump membrane. The pressure is controlled by two solenoid valves as depicted in Figure 2.5. The advantage of this actuation tech-

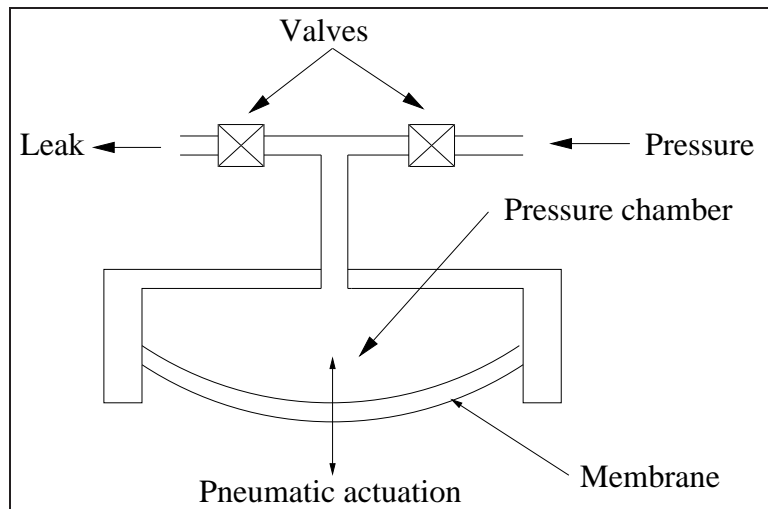


Figure 2.5: Pneumatic actuation.

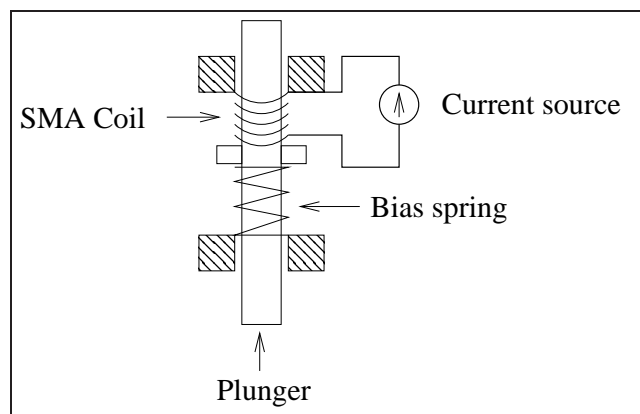


Figure 2.6: Shape memory alloy actuation.

nique is that large forces can be generated. The disadvantage of this mechanism is that the system needs high pressured gas mostly from external sources and the response time is limited to the response time of the solenoid valves.

2.2.2.6 Shape memory alloy actuators

The SMA is initially memorized in its cold state as a stretched out coil. The coil is then compressed when placed onto the actuator. The SMA is actuated by passing current through a coil and heating the SMA to critical temperature causing the SMA to expand to its initial state. This displacement causes pressure on a pump membrane as depicted in Figure 2.6. As the SMA cools down the bias spring returns the SMA to its previous shape. The advantage of this actuator is light weight and the disadvantage is energy inefficiency and slow response times.

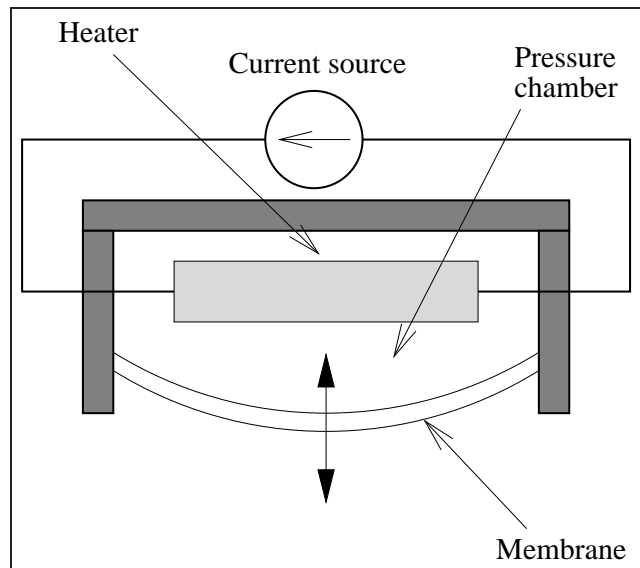


Figure 2.7: Thermopneumatic actuation.

2.2.2.7 Thermopneumatic actuators

This actuation technique utilizes the expansion of a gas when heated to produce a displacement as depicted by Figure 2.7. The advantage of this system is that it's capable of producing large forces and high stroke volumes. The disadvantage is that the resistive heating requires large quantities of power and the response time is limited.

2.2.2.8 Bimetallic thermal actuators

This actuation technique functions by manipulating the different thermal expansion coefficients of two materials. Heating the two structures will cause them to expand in a different manner to each other. This difference in expansion causes displacement (See Figure 2.8).

2.2.3 Types of micropumps

This section details the various types of micropumps and how they function. Micro-pumps can be divided into mechanical and non-mechanical micropumps as depicted in Figure 2.9.

2.2.4 Mechanical micropumps

Three classes of mechanical micropumps have been identified as favorites among researchers. These classes are peristaltic, reciprocating and rotary. Reciprocating micropumps enjoys preference among researchers as is evident from Table 2.1. These pumps offer simple design and manufacturing, thus making them the more feasible option of the three. Reciprocating micropumps can be divided into two groups namely, positive displacement and fixed geometry rectification pumps.

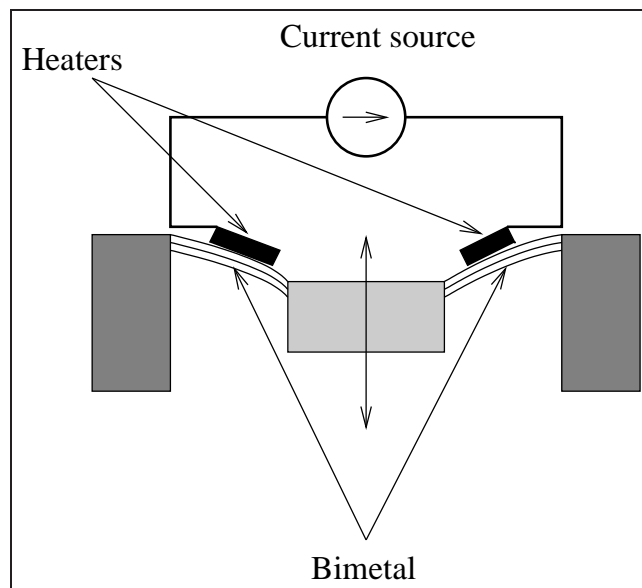


Figure 2.8: Bimetallic actuation.

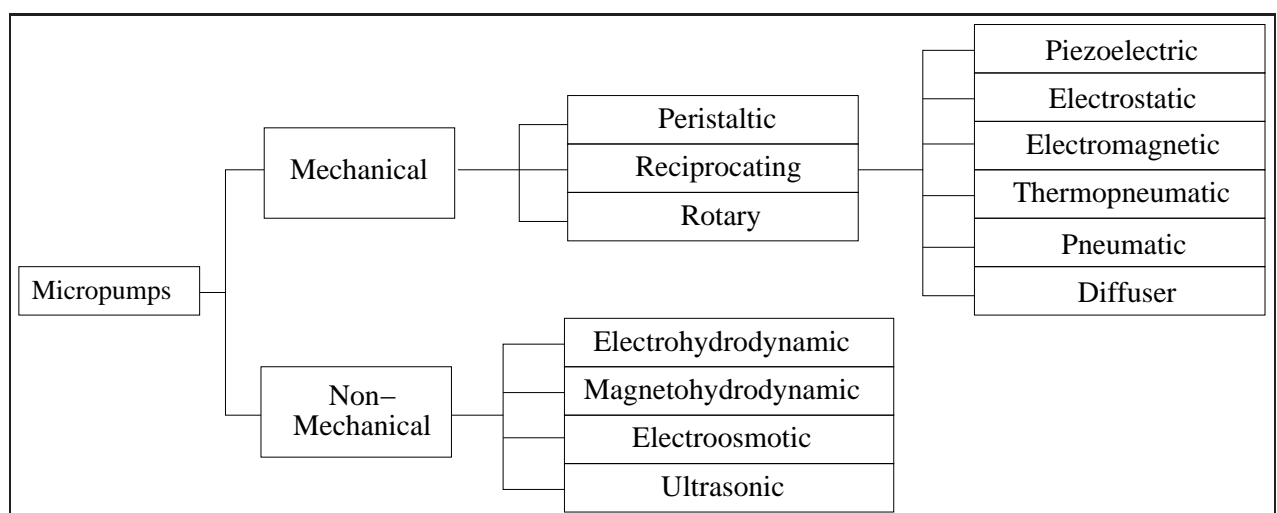


Figure 2.9: Classification of micropumps according to their actuation mechanism and flow rectification methods.

2.2.4.1 Peristaltic micropumps

Peristalsis is the rhythmic contraction of actuation sources to propel contents through a desired tract. These micropumps are popular due to its dual-directional capability, simplicity and relatively low manufacturing costs. The actuation membranes are normally closed as depicted in Figure 2.1 for (0, 0, 0). By displacing the membrane in a peristaltic manner as depicted in Figure 2.1, a volume is displaced. Pumping direction is therefore only dependent on the actuation sequence of the membranes.

Table 2.1: Characteristics of mechanical micropumps from literature [4; 11; 12; 13; 14; 15; 16; 17; 18; 19].

Year	Author	Pump Principle	Actuation Mechanism	Operation Frequency (Hz)	Volume Flow ($\mu\text{l}/\text{min}$)	Maximum Pressure
1988	H. T. G. Van Lintel et al.	Reciprocating Displacement	Piezoelectric Disk		<10	2.0 mH ₂ O
1989	Jan G. Smits	Peristaltic	Piezoelectric Disk		3	0.6 mH ₂ O
1990	Jan G. Smits	Peristaltic	Piezoelectric Disk	15	100	0.6 mH ₂ O
1990	F.C.M. Van De Pol	Reciprocating Displacement	Thermo Pneumatic	1	34	0.5 mH ₂ O
1990	Shuichi Shoji et al.	Reciprocating Displacement	Piezoelectric Stack	40	40	1.5 mH ₂ O
1991	Jack W. Judy et al.	Reciprocating Displacement	Electrostatic		12 - 640nl per cycle	n/a
1992	Hideo Mizoguchi et al.	Peristaltic with 4 valves	Laser light driven (thermal)	3	5.4	0.03 mH ₂ O
1992	R. Zengerle et al.	Reciprocating Displacement	Electrostatic	25	70	0.25 mH ₂ O
1993	Lammerink et al.	Reciprocating Displacement	Thermo Pneumatic	5	60	0.4 mH ₂ O
1993	Erik Stemme et al.	Reciprocating Displacement	Piezoelectric Disk		16ml/min	2.0 mH ₂ O
1993	Stemme & Stemme	Reciprocating, valveless, diffuser	Piezoelectric Disk	300	3000	2.5 mH ₂ O
1994	B. Bustgens et al.	Reciprocating Displacement	Thermo Pneumatic		44	3.8 mH ₂ O
1994	R. Rapp et al.	Reciprocating Displacement	External Pneumatic drive		83 (gas)	0.47 mH ₂ O
1994	Anders Olsson et al.	Reciprocating, valveless, diffuser	Piezoelectric Disk	560	16ml/min	1.7 mH ₂ O
1994	Gerlach et al.	Reciprocating, valveless, diffuser	Piezoelectric Disk	8000	480	0.33 mH ₂ O
1995	C. H. Ahn and M. G. Allen	Jet-type rotary	Electromagnetic	83	24 (Insulin)	n/a
1995	Anders Olsson et al.	Reciprocating, valveless, diffuser	Piezoelectric Disk	1300	225	1.7 mH ₂ O
1996	Thomas Weisener et al.	Rotary Positive Displacement	Driven by external motor	100	100	500 mH ₂ O
1996	M. Stehr et al.	Reciprocating Displacement	Piezoelectric Disk (bimorph and cantilever type)		1600	1.7 mH ₂ O
1996	Anders Olsson et al.	Reciprocating Displacement	Piezoelectric Disk	3000-4000	2300	7.6 mH ₂ O
1996	J. Dopfer et al.	Rotary Positive Displacement	Miniaturized stepping motors		200	0.7 mH ₂ O
1996	J. Dopfer et al.	Reciprocating Displacement	Piezoelectric Disk		300	10.0 mH ₂ O
1996	P. Dario et al.	Reciprocating Displacement	Electromagnetic		780000	0.55 mH ₂ O
1997	W.L. Benard	Reciprocating Displacement	Shape Memory Alloy		50	n/a
1997	Ingo Ederer et al.	Reciprocating Displacement	Piezoelectric Disk		48 g/h of RME fuel	n/a
1997	M. Koch et al.	Reciprocating Displacement	Piezoelectric (Thick Film)		120	0.2 mH ₂ O
1997	Torsten Gerlach	Reciprocating Displacement	Piezoelectric Disk		7800 (gas)	0.28 mH ₂ O
1997	Andrew S. Dewa et al.	Rotary Positive Displacement	Electromagnetic		350	0.14 mH ₂ O
1998	William L. Bernard et al.	Reciprocating Displacement	Shape Memory Alloy		50	0.053 mH ₂ O
1998	R. Linnemann	Reciprocating Displacement	Piezoelectric Disk		1400	1.0 mH ₂ O
1998	K. P. Kamper et al.	Reciprocating Displacement	Piezoelectric Disk		400	21.0 mH ₂ O
1998	Norbert Schwesinger et al.	Peristaltic	Pneumatic		800	n/a
1999	Didier Maillefer et al.	Reciprocating Displacement	Piezoelectric Disk		1667	2.0 mH ₂ O
1999	Jung-Ho Park et al.	Reciprocating Displacement	Piezoelectric Stack		4.8	32.0 mH ₂ O

2.2.4.2 Positive displacement reciprocating micropumps

This type of micropump usually consists of a actuation mechanism coupled to a flexible membrane on top of a pressure chamber. As the membrane actuates at a given frequency, valves at the inlet and outlet rectifies the flow in one direction as depicted in Figure 2.10(a-c). Positive displacement micropumps are designed to maximize pump pressure and stroke volume ΔV and minimize the dead volume V_o . The compression ratio of the pump can thus be defined as [1]

$$\varepsilon = \frac{\Delta V}{V_o} . \quad (2.2.1)$$

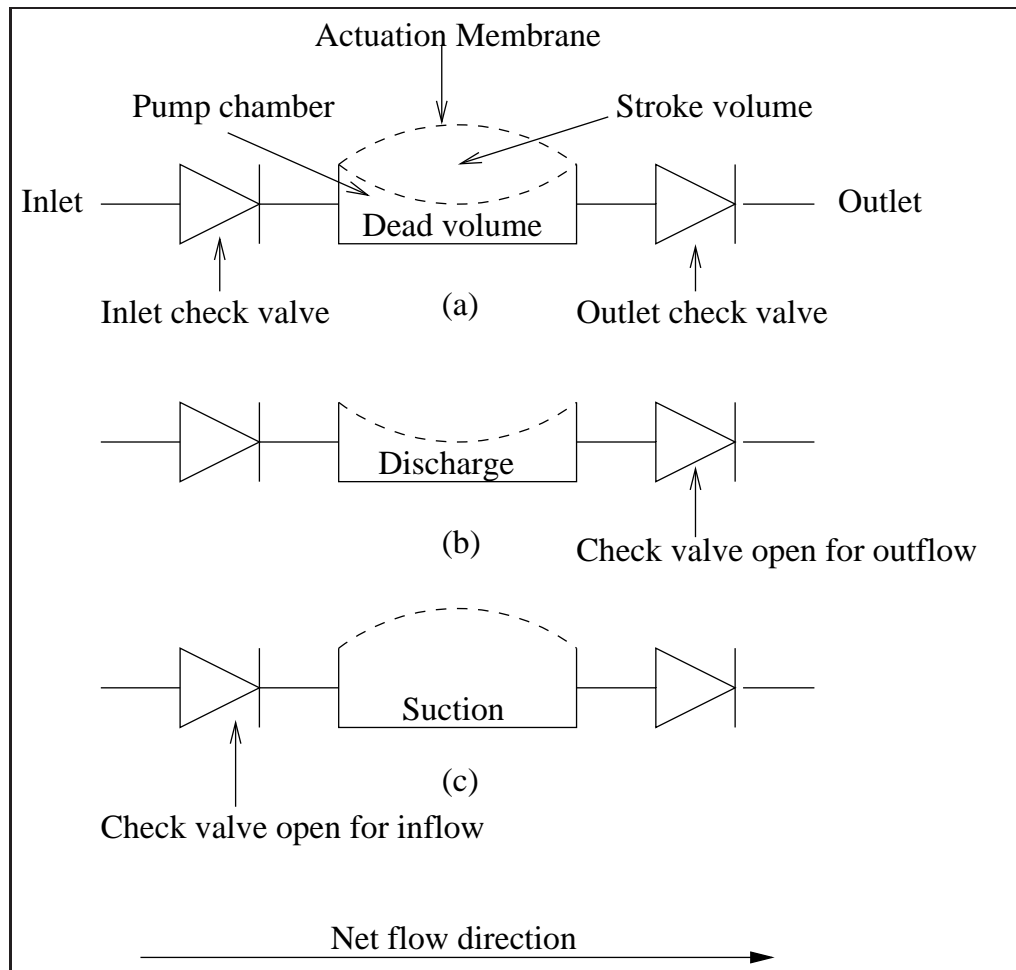


Figure 2.10: (a) Illustration of a reciprocating pump with inlet and outlet valves, (b) outlet stroke, and (c) inlet stroke.

The compression ratio of these pumps is characteristically low due to their small membrane displacement. The compression ratio is of little importance if the pump is operated with an incompressible fluid such as water.

The compression ratio becomes significant if the micropump is used with a compressible media such as air. The valves of a positive displacement pump have a critical pressure at which they will open. A compressible gas in a fluid such as water can cause a decreased pressure in the chamber and the valves may fail to open at the lower pressure. Figure 2.11 depicts examples of positive displacement micropumps and their different valve designs.

2.2.4.3 Fixed geometry rectification micropumps

Another type of reciprocating micropumps is the fixed geometry rectification pump, also known as a valveless micropump. Unlike positive displacement pumps, these micropumps rely on specifically designed microchannels to rectify the net flow in one direction. The advantage of this type of micropump is that they are simpler than the positive displacement pumps. They are therefore simple to manufacture and less susceptible to clogging and valve failure. There are

two types of rectification valves used in fixed geometry rectification pumps, diffuser / nozzle and Tesla-type.

In the diffuser/nozzle type, diffuser flow has a different flow resistance than that of a nozzle flow. A net flow is thus achieved during repeated actuation of the membrane as depicted in Figure 2.12. The difference in flow resistances can be explained by studying the flow through a diffuser. This is discussed in more detail in Section 5.4.

Depending on the angle of the diverging walls and edge rounding, different flow directions can be achieved as presented by Olsson *et al.* [26].

The Tesla type valve uses the valvular conduit as a flow directing element as depicted in Figure 2.13. Little data is available for this type of micropump [22].

2.2.5 Non-mechanical micropumps

In contrast to mechanical micropumps, non-mechanical micropumps generally have no moving parts or valves. They convert non-mechanical energy into kinetic energy of the fluid. This gives these micropumps the advantage of simplicity in design and fabrication. They are also less susceptible to clogging. The disadvantage of this type of micropump is that it has inferior performance when compared to mechanical micropumps and is restricted to certain types of working fluid.

There are numerous types of non-mechanical micropumps being researched, only the most popular choices are described in the following sections.

2.2.5.1 Electroosmotic micropump

EOF is a subset of electrokinetic phenomena related to the movement of electric charges in an applied electric field. This type of micropump is used to pump electrically conductive solutions. This theory is described by Zeng *et al.* [2]: “*Most surfaces spontaneously develop an EDL when brought into contact with either weak and strong electrolyte solutions. This charge generation is caused by electrochemical reactions at the liquid solid interface. When an external field is applied parallel to the wall, ions will move in response to the field and drag surrounding liquid with them. This ion drag causes a net motion of bulk along the wall that is called electroosmotic flow.*” This phenomena is depicted in Figure 2.14.

2.2.5.2 Electro-hydrodynamic micropump

An EHD micropump achieves flow when an applied electrical field acts on induced charges within the fluid to move the fluid. Fluid forces are generated by the interaction of the electric fields with the charges they induce in the fluid. The fluid must be of low conductivity and dielectric in nature in order for EHD pumping to occur [22].

2.2.5.3 Ultrasonic micropump

Ultrasonic micropumps, also known as flexural plate wave micropump, utilize the properties of acoustic streaming to set the working fluid in motion. This acoustic field is set up by flexural plate waves, generated by an array of piezoelectric actuators. These waves propagate along a thin plate that constitutes one wall of a flow channel [22].

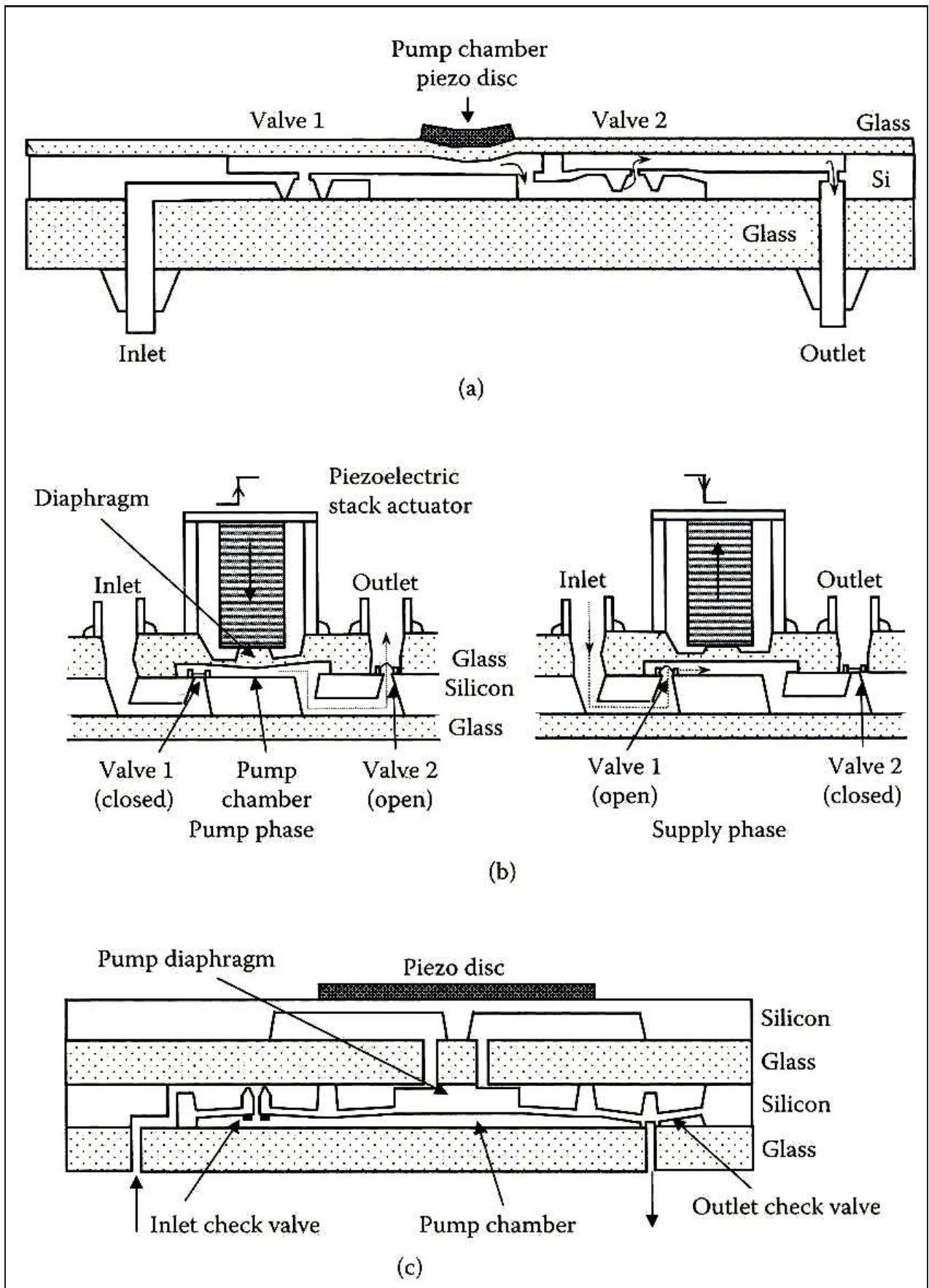


Figure 2.11: (a) An example of a positive displacement micropump, (b) piezoelectric stack actuation with disk valves in pump and supply mode, and (c) piezoelectric disk actuation with disk valves and silicon as piezoelectric mount [1].

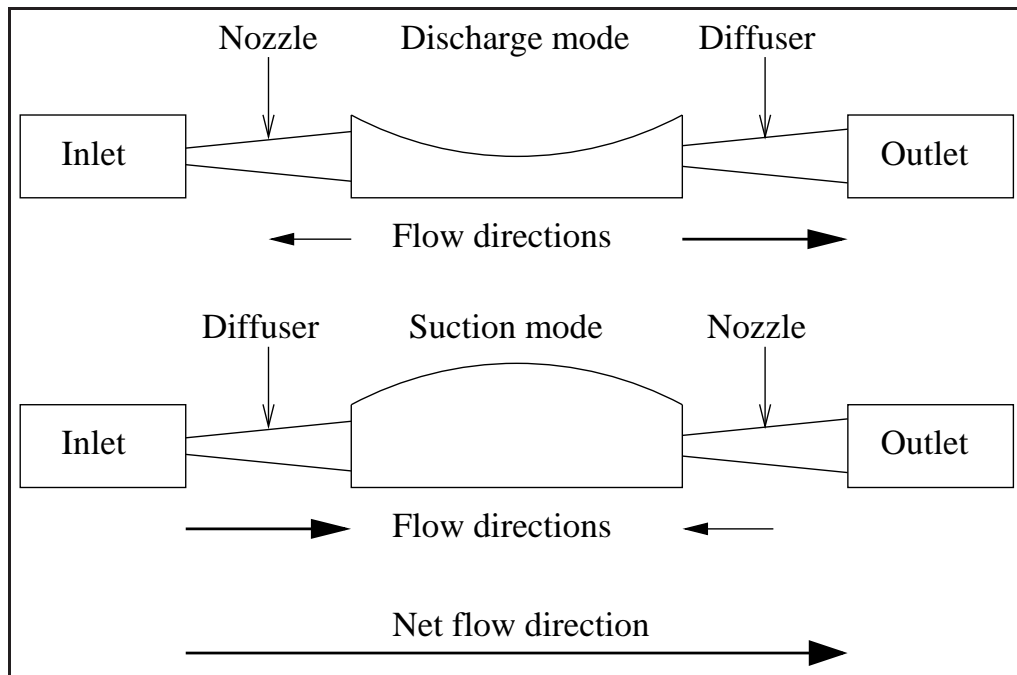


Figure 2.12: Schematic presentation of a diffuser/nozzle type micropump.

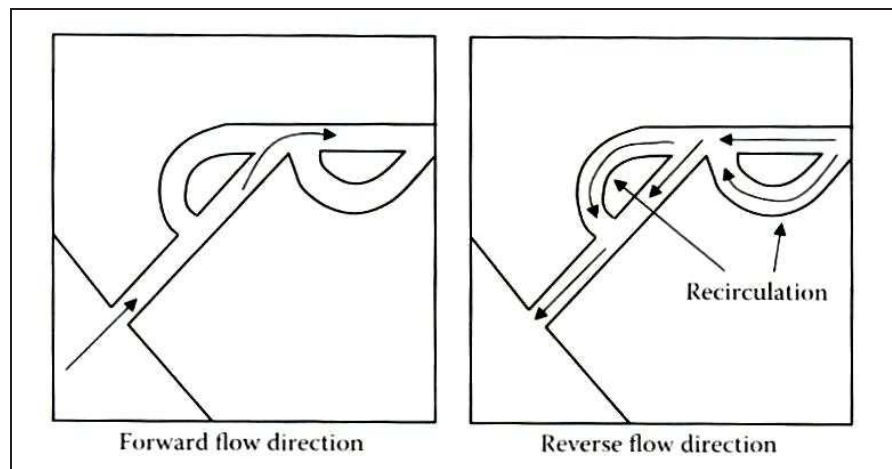


Figure 2.13: Schematic presentation of the Tesla type microvalve [1].

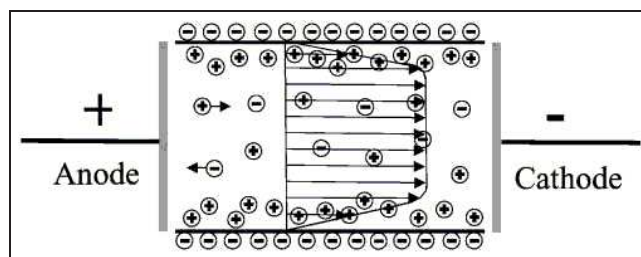


Figure 2.14: Schematic illustration of electroosmotic flow through a pore with a finite EDL [2].

Chapter 3

Micro manufacturing technologies and materials

“Micro-fabrication is the set of technologies used to manufacture structures with micrometric features. This task can unfortunately not rely on the traditional fabrication techniques such as milling, drilling, turning, forging and casting because of the scale” [3].

This chapter explores the different processes that are utilized in order to manufacture MEMS devices and specifically micropumps. Only a few of these processes are described in this chapter as most of the manufacturing processes are not available or are very limited in South Africa. Manufacturing processes will also be limited due to the bio-compatibility of materials.

MEMS manufacturing processes are usually associated with the manufacturing of IC's. All the etching processes use a variation of a masking techniques to pattern a desired geometry on a substrate. The advantage of using IC manufacturing processes is that thousands of devices can be made from a single silicon wafer. It is this characteristic that makes this process capable of bulk manufacturing at a very low cost per unit. Most of the processes rely on the material properties of silicon for accuracy and certain characteristic features.

3.1 Materials in bio-MEMS

This section details the different materials used for bio-MEMS manufacturing. In order for a material to be classified as a bio-compatible material it must comply with ASTM and FDA standards. General areas of compliance include [27]:

- mechanical properties,
- interaction with blood plasma and proteins,
- healing response after implantation,
- metallic corrosion,
- biomaterial degradation and resorption, and
- immunogenicity (ability to stimulate the immune response).

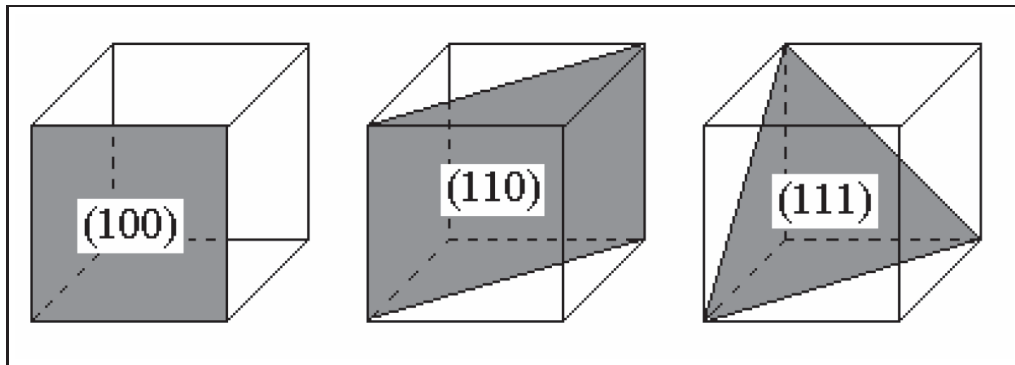


Figure 3.1: Illustration of main planes in the cubic lattice of silicon [3].

3.1.1 Silicon

Silicon is the material used to create the majority of IC's used in consumer electronics in the modern world. Silicon is a hard and brittle material that deforms elastically until it reaches fracture point, at which point it breaks.

The use of silicon in MEMS have considerable advantages, motivated through its variety of material properties. In single crystal form, silicon is an almost perfect Hookean material, meaning that when it is flexed there are virtually no hysteresis effects. This feature of silicon makes it ideal for sensors and actuators to avoid accumulating errors.

Silicon is an ideal material for highly repeatable motion as it suffers very little from fatigue. Some fabrication techniques rely on the lattice structure of silicon for accuracy and geometry. Figure 3.1 depicts the main lattice structures that influence etching of silicon. These planes in the silicon lattice can be manipulated to etch diffusers, nozzles and other structures for micropumps as depicted in Figure 3.2.

Properties of silicon include, good thermal conductivity (comparable to steel and aluminum) with a low thermal expansion coefficient [28]. It is also a material with piezoresistive properties and a yield strength that surpasses that of stainless steel.

Bio-compatibility of silicon remains somewhat of an enigma for researchers. This is because surface characteristics of bio-MEMS materials that should be considered include not only chemistry and surface texture but also hydrophilicity, charge, polarity and energy, heterogeneous distribution of functional groups and water absorption [28].

3.1.2 PDMS

PDMS is a silicon-based organic polymer, and is particularly known for its unusual flow properties. This polymer is a viscoelastic material, meaning that at long flow times or high temperatures, it acts like a viscous liquid and at short flow times acts rubber like. PDMS is a commonly used bio-compatible material and has been used in breast implants.

This material also has the ability to conform to small shapes and channels making it ideal for microfluidic devices.

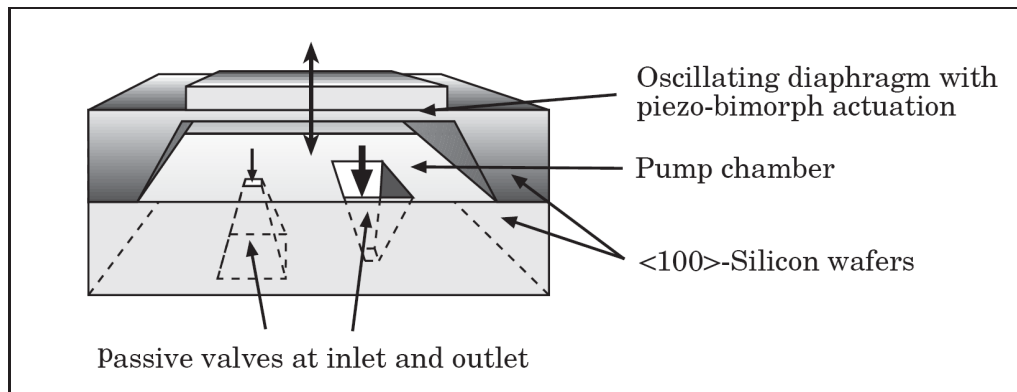


Figure 3.2: Illustration of planes manipulation in the cubic lattice of silicon to form diffusers and nozzles for a valveless micropump [4].

3.2 Manufacturing techniques for MEMS

This section details the most common manufacturing techniques and processes that can be utilized for this project. In general, MEMS fabrication strive to use batch processes to benefit from the same economical advantages as that of IC's.

3.2.1 Deposition processes

Deposition processes is one of the basic building blocks of micro-fabrication. It involves the deposition and subsequent patterning of a thin film, on a layer of silicon. This method is regularly used in process integration, and consists of techniques like PVD, CVD and sputtering.

In a typical CVD process the substrate is exposed to one or more volatile vapors. The vapors react and decompose on the silicon surface to produce the desired deposit.

PVD is the condensation of a vaporized form of the material onto a semiconductor.

Sputtering occurs when a plasma discharge bombards the material sputtering some away as a vapor.

3.2.2 Photolithography

Photolithography can be defined as the transfer of a pattern on a mask, to a photosensitive material by selective exposure to a radiation source such as UV light. A photosensitive material, or photoresist, is a material that experiences a change in its physical properties when exposed to a radiation source. The photoresist is spin coated on the substrate as a thin-film using a spinning process. Photoresist can be classified as positive photoresist or negative photoresist. The exposed region in a positive photoresist is removed during etching, leaving only the unexposed photosensitive material as depicted in Figure 3.3. Photolithography is generally used with a variety of etching steps and manufacturing processes.

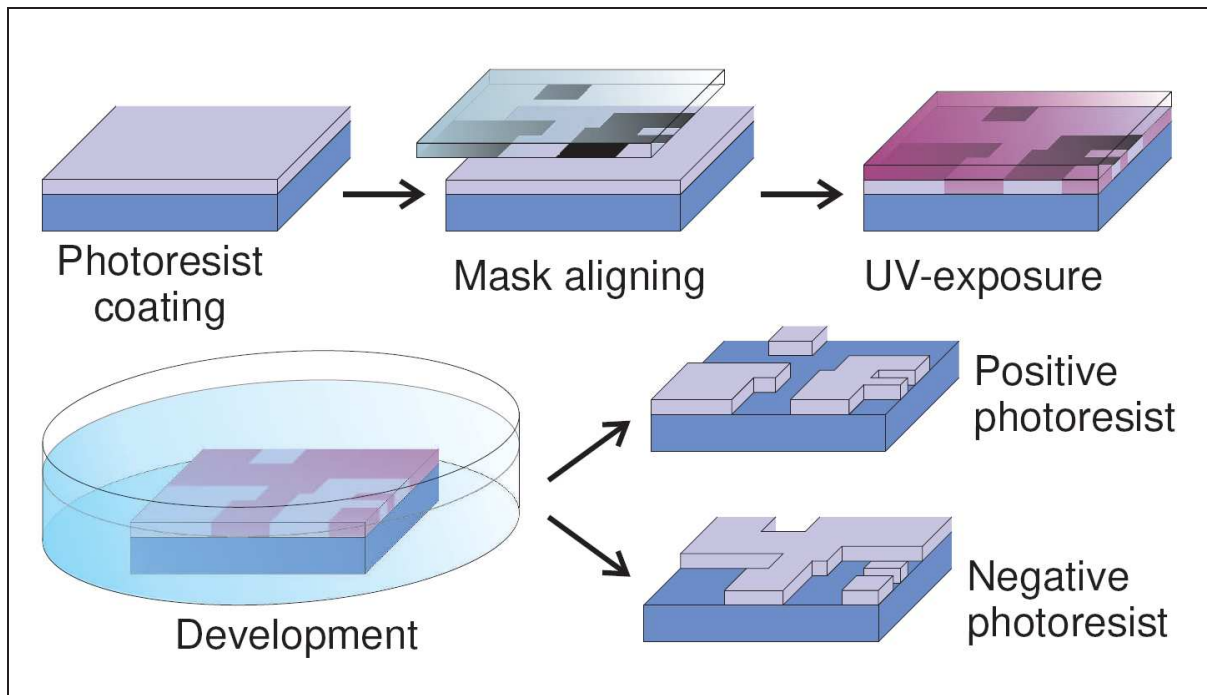


Figure 3.3: Illustration of photo-patterning in positive and negative photoresist [3].

3.2.3 Etching processes

Etching processes consists of two basic types, wet etching and dry etching. Wet etching is when the desired material is etched away, when immersed in a chemical solution. Dry etching is when the material is dissolved using reactive ions or a vapor phase etchant.

3.2.3.1 Wet etching

Wet etching normally consists of an etchant, usually a strong alkali such as potassium hydroxide (KOH) or tetramethyl ammonium hydroxide (TMAH), and a sacrificial material. When etching a single crystal materials such as silicon, two types of wet etching can be identified:

- anisotropic wet etching and
- isotropic wet etching.

During anisotropic wet etching, the etching rate is dependent on the orientation of the lattice structure. Figure 3.4 depicts a $\langle 100 \rangle$ oriented wafer aligned with $\langle 110 \rangle$ directions is placed in anisotropic etchant. The exposed $\langle 100 \rangle$ planes etches rapidly, but the $\langle 111 \rangle$ planes etch slowly. Isotropic wet etching etches away at the same rate in all directions as depicted in Figure 3.4. Anisotropic wet etching is used for more precision while isotropic is used for undercutting certain materials that's required to move [29].

3.2.3.2 Dry etching

Dry etching as explained by Chollet and Liu [3]: “Dry etching is a series of methods where the solid substrate surface is etched by gaseous species. Plasma is usually involved in the process to

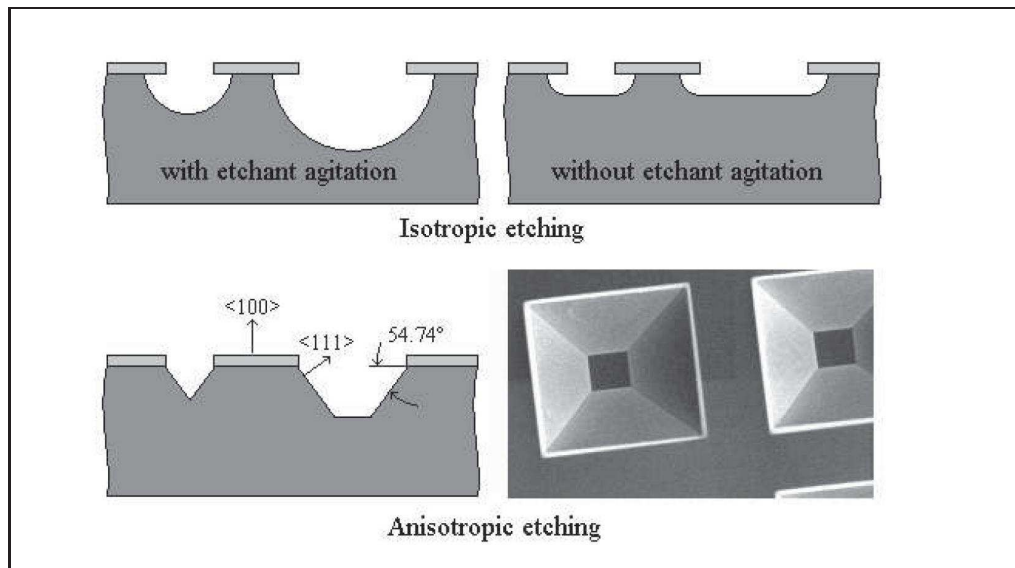


Figure 3.4: The difference between isotropic and anisotropic wet etching [3].

increase etching rate and supply reacting ions and radicals.” The etching can be introduced in a number of ways:

- physically by ion bombardment,
- chemically through a chemical reaction occurring at the solid surface, and
- by mechanisms combining both physical and chemical effects.

The selectivity of these etching processes are usually more anisotropic for physical etching and isotropic for chemical etching.

3.2.4 Wafer bonding

Wafer bonding is used for joining two silicon wafers to create a stacked wafer layer. Two main types of wafer bonding processes is:

- **Direct wafer bonding**

This process involves hydrating the two surfaces to be bonded then pressing them together. The contacted pair is then placed in a high-temperature furnace to fuse the wafers together as depicted in Figure 3.5 [29]. The resulting bond is as strong as the silicon itself and the top layer of silicon can be thinned.

- **Anodic bonding**

This bonding technique is restricted to specific glasses that can be bonded to silicon wafers. This process relies on a voltage source and heat to bind the two materials. The two materials is heated to 500°C and a positive charge of ± 600 Volts is applied. The silicon repels sodium ions from the glass surface, creating a net negative charge at the glass

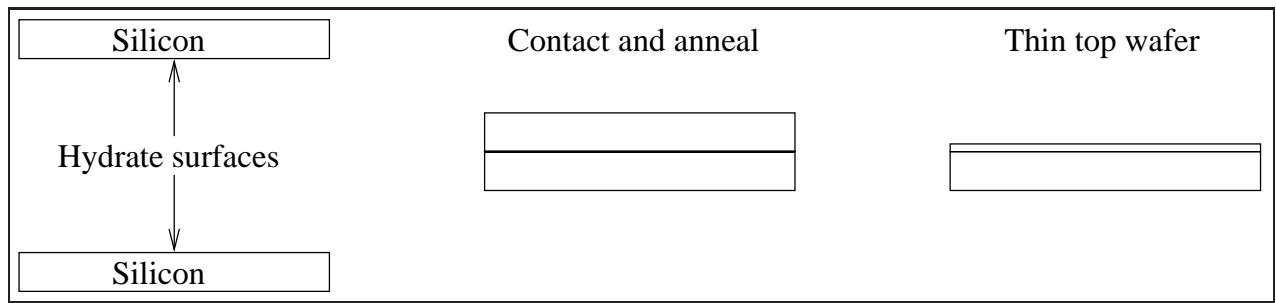


Figure 3.5: Direct wafer bonding process.

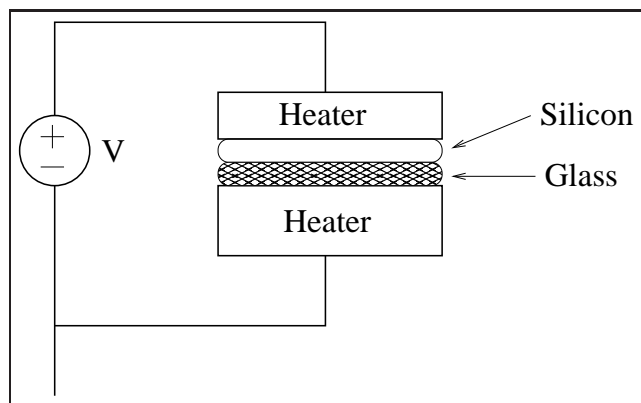


Figure 3.6: Anionic wafer bonding process.

surface [29]. This nett charge creates a large attraction force between the two materials, bringing them in close contact. The heat then fuses them together as depicted in Figure 3.6.

3.2.5 Surface micromachining

Unlike bulk micromachining in which microstructures are formed by etching into a substrate, surface micromachining builds up structures by adding materials, layer by layer. The thin film layers deposited are typically 1-5 μm thick, some acting as structural layer and others as sacrificial layers.

Dry etching is usually used to define the shape of the structure layers, and a final wet etching step releases them from the substrate by removing the supporting sacrificial layer as depicted in Figure 3.7.

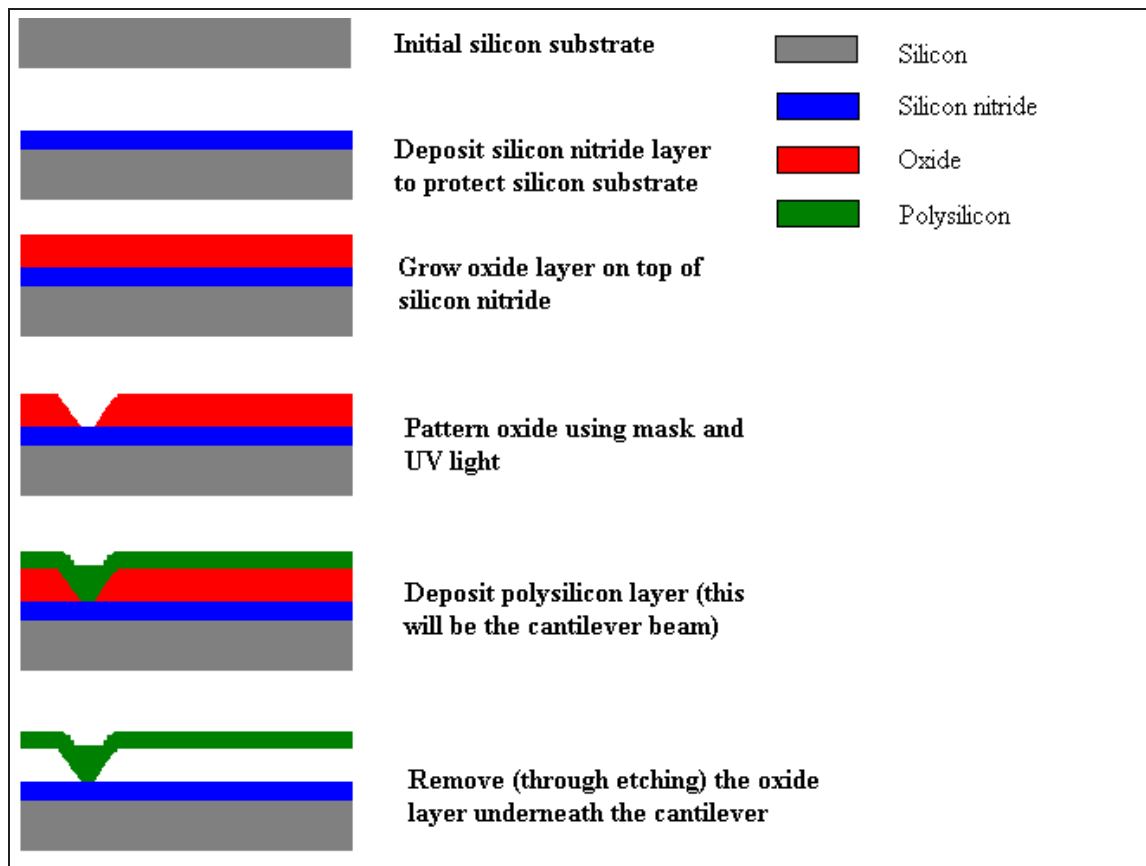


Figure 3.7: Illustration of the surface micromachining process. [5]

Chapter 4

Micropump design

This chapter outlines the different phases involved in micropump design. These design aspects are depicted in Figure 4.1.

4.1 Design phases

MEMS design differs from that of macro design. Challenges include physical scaling laws (see Section 5), manufacturing inaccuracies and the availability of manufacturing processes. Relative manufacturing accuracy of MEMS decrease when scaling down, thus the design has to be tolerant of manufacturing inaccuracies. Manufacturing techniques and processes in South Africa are not abundant and most processes are costly.

Figure 4.1 depicts the various design phases the designer has to navigate in order to limit the cost and time of the design. This chapter details each of the steps in the design process.

4.2 Problem statement

As explained in Section 1.2 and Section 2.1.2 there are numerous advantages and challenges when scaling down to MEMS size. The necessity for micropumps arose out of the advantages posed by μ TAS devices, which will revolutionize drug delivery systems as we know them.

The proposed micropump should meet the following objectives:

- the micropump must be made from a bio-compatible material,
- it should be able to deliver a minimum flow rate of $\pm 2000 \mu\text{L}/\text{min}$,
- should be integrable with existing manufacturing techniques and processes,
- be of a simple design to allow for manufacturing in South Africa,
- as the micropump will be used in the bio-medical field the micropump should have moderate fluid handling characteristics to keep from damaging biological material, and
- the micropump should also be highly reliable as it can be inaccessible for replacement or maintenance.

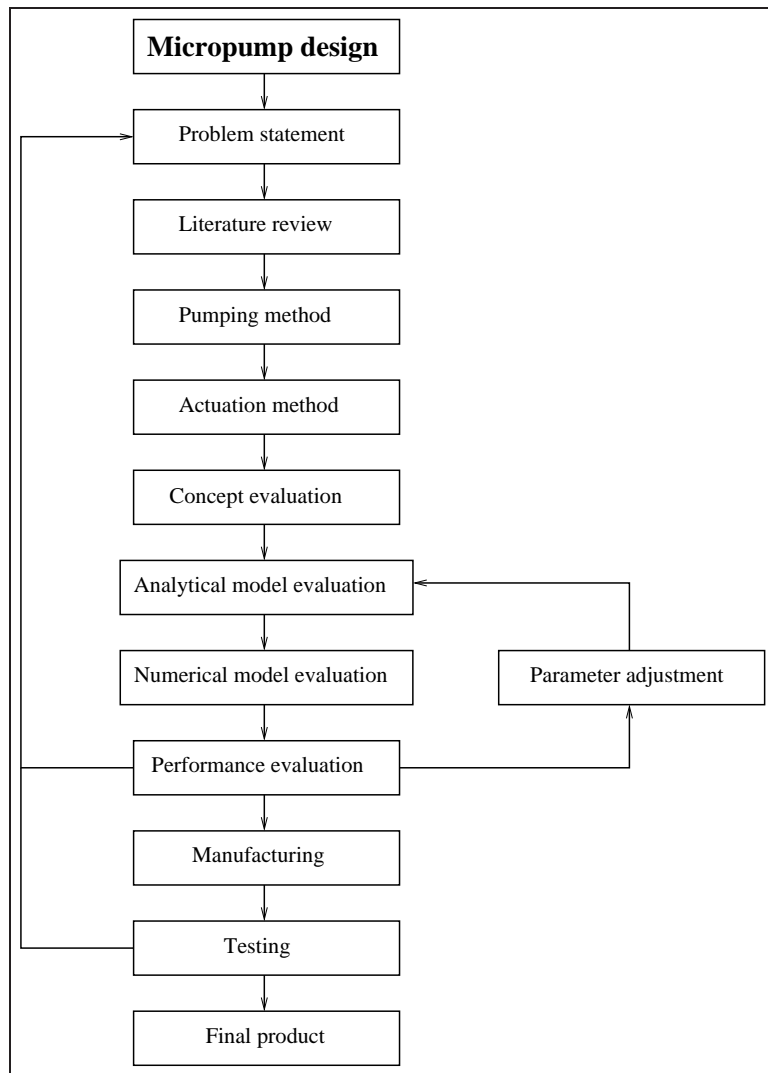


Figure 4.1: Illustration of the different design aspects.

4.3 Concept evaluation

Evaluating different concepts from the literature provides a clear understanding of the objective and goals for the project. Dividing the micropump into actuation mechanism and pump method provides freedom and flexibility in the design. Once the pumping method is determined the corresponding actuation mechanism can be decided on. The primary influences on the design are:

- availability of materials and manufacturing technologies,
- simplicity of the design to improve manufacturability,
- bio-compatibility of the materials and design used, and
- flexibility to pump different fluids such as blood plasma and water.

All of the above mentioned criteria are used to determine the most suitable concept.

4.3.1 Pump mechanism

Non-mechanical micropumps

These micropumps have the advantage of being relatively easy to manufacture, but pose implementation problems. When considering the design criteria and the properties of the various pumping methods as set out in Section 2.2.3 these micropumps are not a rational choice. They are limited to certain types of fluids and they have low characteristic flow rates.

Positive displacement micropumps

These micropumps are also described in Section 2.2.4.2. They are the most common choice in the literature as illustrated by Table 2.1. They have the advantage of producing high pressures and high efficiencies, but have reliability problems. They are also complex to manufacture and have high wear on valves and moving parts. The main concern with operating these pumps in a biomedical application is their jagged fluid handling characteristics and their susceptibility to clogging.

Peristaltic micropumps

The operation of peristaltic micropumps are described in Section 2.2.4.1. Peristaltic micropumps have advantages that include bi-directional pumping capability, high operating pressures and high efficiencies. They are relatively simple to manufacture but are also unreliable as a result of moving parts. They are also prone to clogging and therefore have unwanted biological fluid handling characteristics.

Fixed geometry rectification pumps

Fixed geometry rectification micropumps have no moving parts or valves, and are therefore referred to as valveless micropumps. They rely on asymmetrical geometries of the microchannels to rectify the flow in a direction as explained in Section 2.2.4.3. These micropumps are simple to manufacture due to uncomplicated design and are therefore the most cost effective to manufacture. They are reliable due to the absence of moving parts and have moderate fluid handling characteristics for biological-fluids. The limitation of valveless micropumps is that they operate at relatively low pressures as shown in Table 2.1.

4.3.2 Actuation mechanism

Electromagnetic actuators

Electromagnetic actuators as explained in Section 2.2.2.2, have large strokes and are usually coupled to membranes. Their disadvantage is that they are relatively large and draw large currents.

Electrostatic actuators

Electrostatic actuators is described in Section 2.2.2.3, and rely on the capacitive force when charging two parallel opposed plates. The advantage of this actuator is low energy consumption. The disadvantage of this actuator is that the force is inversely proportional to the square of the distance between the plates.

Piezoelectric actuators

Table 4.1: Evaluation of the pumping method against different weighted criteria.

Evaluated criteria	Pump principal			
	Non-mechanical	Positive displacement	Peristaltic	Fixed geometry
Fluid handling - (20)	20	5	5	15
Reliability - (20)	15	8	5	20
Simplicity - (10)	5	3	5	10
Flow rate - (5)	1	5	5	4
Pressure - (5)	1	5	5	3
Total	42	26	25	52

Piezoelectric actuators is detailed in Section 2.2.2.4, and are the most commonly used actuator for micropumps as seen in Table 2.1. Piezoelectric disks can be stacked to produce a larger force but at cost of the, otherwise fast, response time. They are energy efficient when used in the form of small disks.

Pneumatic actuators

Pneumatic actuators are described in Section 2.2.2.5, and have large forces and stroke lengths. They are limited to the response time of the valves and the supply of pressurized gas.

SMA Actuators

SMA's response time is limited to the cooling of the alloy, and the coil draws a large current. SMA actuators are detailed in Section 2.2.2.6.

Thermopneumatic actuators

Thermopneumatic actuators function by the expansion of heating a gas, as explained in Section 2.2.2.7. These actuators have large stroke lengths and produce large forces, they however use large quantities of energy to heat the gas inside the pressure chamber. These type of actuators also have undesirable response times.

4.4 Final concept

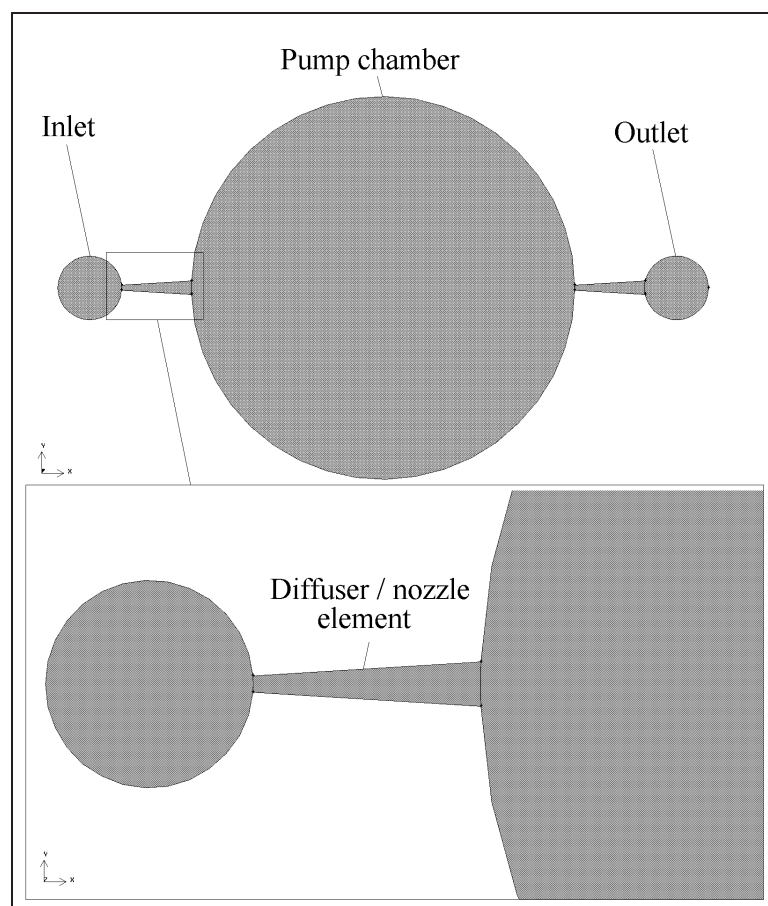
Tables 4.1 and 4.2 illustrate the importance of fluid handling characteristics for a bio-medical micropump. These tables are therefore only to provide perspective of the importance of biocompatibility. The advantages offered by the valveless micropump combined with the piezoelectric actuator are overwhelming as illustrated by Tables 4.1 and 4.2. These two concepts merge to form the solution that best satisfies the evaluation criteria. The fluid handling characteristics are good compared to that of positive displacement and peristaltic micropumps. The literature gives enough motivation to believe that the desired flow rate is achievable. The simplicity of the valveless micropump is also ideal for the manufacturing techniques available.

The valveless micropump design will utilize the diffuser / nozzle concept, as depicted in Figure 4.2, to direct the flow in the desired direction.

The micropump is designed and manufactured in planar two dimensions, with the third dimension a constant thickness. The diffuser / nozzle elements are flat and not conical. Under

Table 4.2: Evaluation of the actuation method against different weighted criteria.

Evaluated criteria	Actuation principal					
	Electromagnetic	Electrostatic	Piezoelectric	Pneumatic	SMA	Thermopneumatic
Bio-compatibility - (25)	10	20	23	10	23	10
Stroke size - (20)	20	5	10	20	10	20
Size - (20)	5	15	15	5	10	15
Availability - (10)	5	5	10	10	5	8
Force - (10)	8	5	10	10	5	10
Simplicity - (5)	1	5	5	1	2	3
Total	49	55	73	56	55	66

**Figure 4.2:** The basic design of a diffuser / nozzle type valveless micropump.

the same operating conditions, flat walled diffusers have been shown to be 10-80% shorter than conical diffusers for similar efficiency [9; 26]. Figure 4.3 shows the significant parameters of the flat walled diffuser / nozzle element and will be discussed in detail in Section 5.4.4.

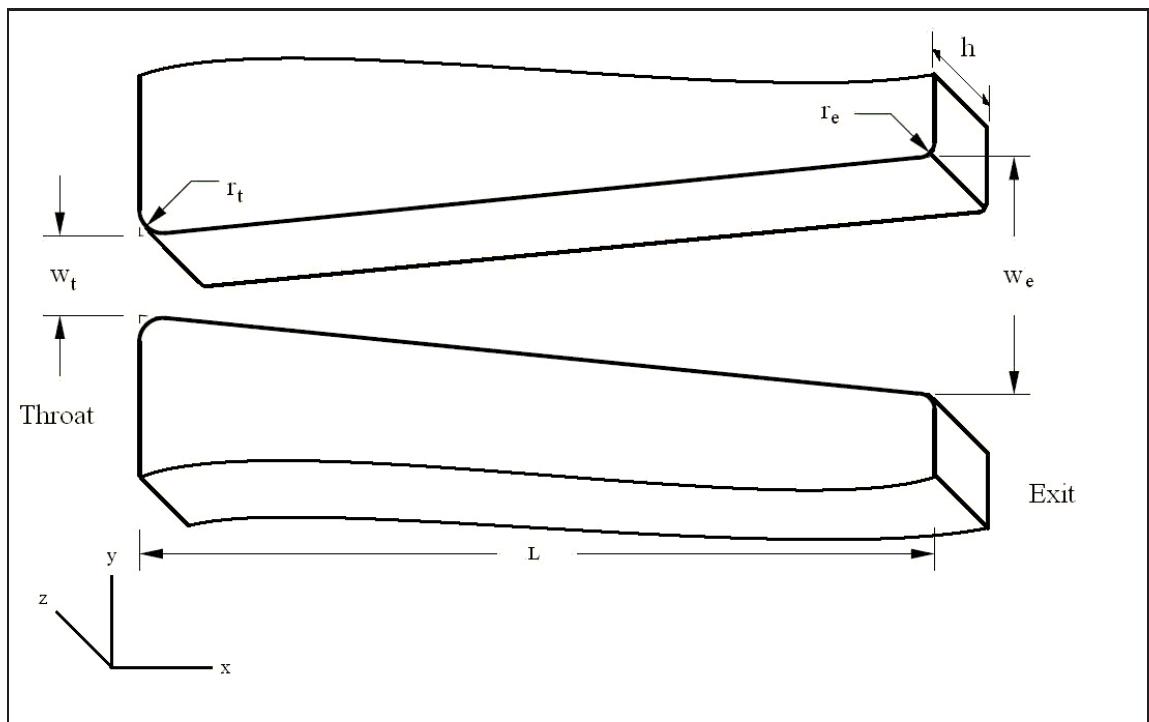


Figure 4.3: A flat walled diffuser / nozzle element.

Chapter 5

Theoretical model

Microchannels are channels with one or more dimensions in the sub-millimeter to single micrometer range. At these small scales and dimensions, our intuition of fluid mechanics can be deceiving. The basic principals of flow physics like conservation of mass and Navier-Stokes, are still valid in the microfluidics domain. Thus to evaluate the difference between microfluidics and macrofluidics, this chapter investigates the different phenomena that dominate the laminar flow regime for Reynolds numbers ranging from $1 \ll Re < 1000$.

5.1 Scaling down

To comprehend the effect of scaling down, consider the case depicted in Figure 5.1, where the size of a cube is reduced ten times. The side dimensions of the cube is reduced from a length

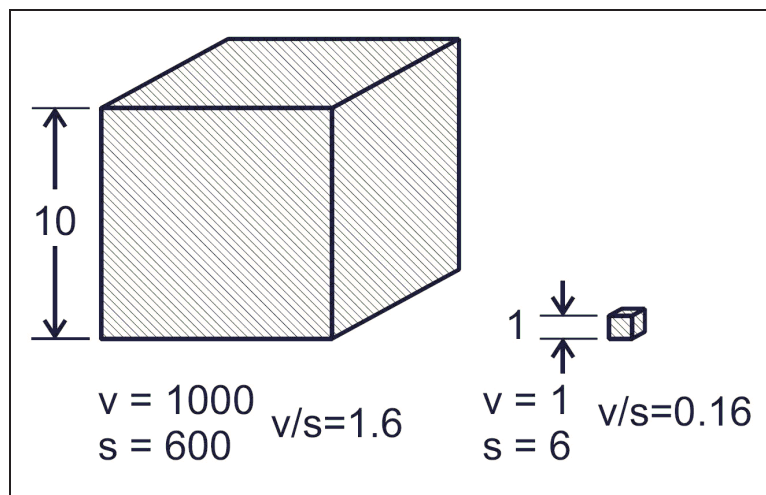


Figure 5.1: Cube down sizing to illustrate scaling effect [3].

10 to a length 1. The initial area of the cube equates to $s = 10 \times 10 \times 6 = 600$. The initial volume of the cube is $v = 10 \times 10 \times 10 = 1000$ and the volume to surface ratio is $v/s = 1.6$ as depicted in Figure 5.1. After scaling down the surface area is $s = 6 \times 1 \times 1 = 6$ whereas the volume is $v = 1 \times 1 \times 1 = 1$ and the volume to surface ratio is now $v/s = 0.16$. The decreased volume to

surface ratio means that when scaling down, the forces and effects dependent on surface-area (friction, electrostatic, surface tension and pressure) will become more dominant over forces associated with volume (inertia and gravitational).

The effects of scaling down on fluidics can be further illustrated by the Reynolds number

$$Re = \frac{V_s L \rho}{\mu} = \frac{\text{Inertial forces}}{\text{Viscous forces}} , \quad (5.1.1)$$

where

- V_s - mean fluid velocity,
- L - characteristic length,
- μ - dynamic fluid viscosity, and
- ρ - fluid density.

In typical microfluidics applications the Reynolds number will range between $1 \ll Re < 100$. This illustrates the dominance of viscous forces (surface dependent) over inertia forces (volume dependent) as the typical Reynolds number for laminar flow is $Re \leq 2000$ in a round tube [9; 30; 31]. A non-dimensionalized Navier-Stokes equation further demonstrates the effect of the Reynolds number on fluidic governing equations as illustrated in the Appendices.

5.2 Governing equations of microfluidics

This section investigates the influence of scaling down (see Section 5.1), on the fluid dynamic governing equations.

When considering fluid governing equations, the fluid is assumed to be a continuum of indivisible molecules which is constantly in motion. Although the fluid particles are constantly in motion only the global effect of the molecules are of interest. These effects include pressure, velocity, viscosity and density. These are all time and position dependent properties of a fluid.

The governing equations of fluidics have been derived from physical laws such as the conservation of mass, momentum and energy.

5.2.1 Continuity equation

The conservation of mass in fluidics equates to the Mass of fluid entering per unit time - Mass of fluid leaving per unit time = Increase of mass of fluid per unit time. The continuity equation is given in differential form as [9; 32]

$$\frac{\partial \rho}{\partial t} + \nabla \cdot (\rho \mathbf{V}) = 0 . \quad (5.2.1)$$

The expanded differential form of the continuity equation in (5.2.1) is given as [9; 30; 31]

$$\frac{\partial \rho}{\partial t} + \frac{\partial(\rho u)}{\partial x} + \frac{\partial(\rho v)}{\partial y} + \frac{\partial(\rho w)}{\partial z} = 0 . \quad (5.2.2)$$

where u, v, w represents local velocities in the x, y, z directions respectively. For an incompressible fluid the density is constant and

$$\frac{\partial \rho}{\partial t} \approx 0, \quad (5.2.3)$$

and Equation (5.2.2) simplifies to

$$\nabla \cdot \mathbf{V} = 0, \quad (5.2.4)$$

where the del operator is defined as

$$\nabla = \frac{\partial}{\partial x} \mathbf{i} + \frac{\partial}{\partial y} \mathbf{j} + \frac{\partial}{\partial z} \mathbf{k}. \quad (5.2.5)$$

5.2.2 Navier-Stokes equation

From the conservation of momentum and Newton's second law, the Navier-Stokes equation is derived. The Navier-Stokes equation for incompressible, constant-viscosity flow, in vector form is given by [1; 9; 30; 31]

$$\rho \left(\frac{\partial \mathbf{V}}{\partial t} + \mathbf{V} \cdot \nabla \mathbf{V} \right) = -\nabla p + \mu \nabla^2 \mathbf{V} + \mathbf{g}, \quad (5.2.6)$$

where

- \mathbf{V} - fluid velocity,
- t - time,
- ∇p - gradient of pressure,
- \mathbf{g} - gravity forces,
- μ - fluid viscosity for a Newtonian fluid, and
- ρ - fluid density.

Rewriting the Navier-Stokes equation in Cartesian coordinates, the following equations are obtained [9; 30; 31]

$$\begin{aligned} \rho \left(\frac{\partial u}{\partial t} + u \frac{\partial u}{\partial x} + v \frac{\partial u}{\partial y} + w \frac{\partial u}{\partial z} \right) &= -\frac{\partial p}{\partial x} + \mu \left(\frac{\partial^2 u}{\partial x^2} + \frac{\partial^2 u}{\partial y^2} + \frac{\partial^2 u}{\partial z^2} \right) + \rho g_x, \\ \rho \left(\frac{\partial v}{\partial t} + u \frac{\partial v}{\partial x} + v \frac{\partial v}{\partial y} + w \frac{\partial v}{\partial z} \right) &= -\frac{\partial p}{\partial y} + \mu \left(\frac{\partial^2 v}{\partial x^2} + \frac{\partial^2 v}{\partial y^2} + \frac{\partial^2 v}{\partial z^2} \right) + \rho g_y, \\ \rho \left(\frac{\partial w}{\partial t} + u \frac{\partial w}{\partial x} + v \frac{\partial w}{\partial y} + w \frac{\partial w}{\partial z} \right) &= -\frac{\partial p}{\partial z} + \mu \left(\frac{\partial^2 w}{\partial x^2} + \frac{\partial^2 w}{\partial y^2} + \frac{\partial^2 w}{\partial z^2} \right) + \rho g_z. \end{aligned} \quad (5.2.7)$$

When the Reynolds number is small i.e. $Re \ll 1$, Equation (5.2.6) is reduced to the Stokes equation for creeping flow [1]

$$\nabla p = \mu \nabla^2 \mathbf{V} + \mathbf{g}. \quad (5.2.8)$$

A physical interpretation of Equation (5.2.8), is that the flow is kinematically reversible. This means that if the flow is forced by a pressure gradient that varies harmonically with time, the mass flow rate will also vary harmonically with time, i.e. there will be no nett movement of the fluid. It is this property of creeping flow that complicates micropump design.

5.3 Microchannels

Consider the flow between two parallel plates as depicted in Figure 5.2. As fluid enters the chan-

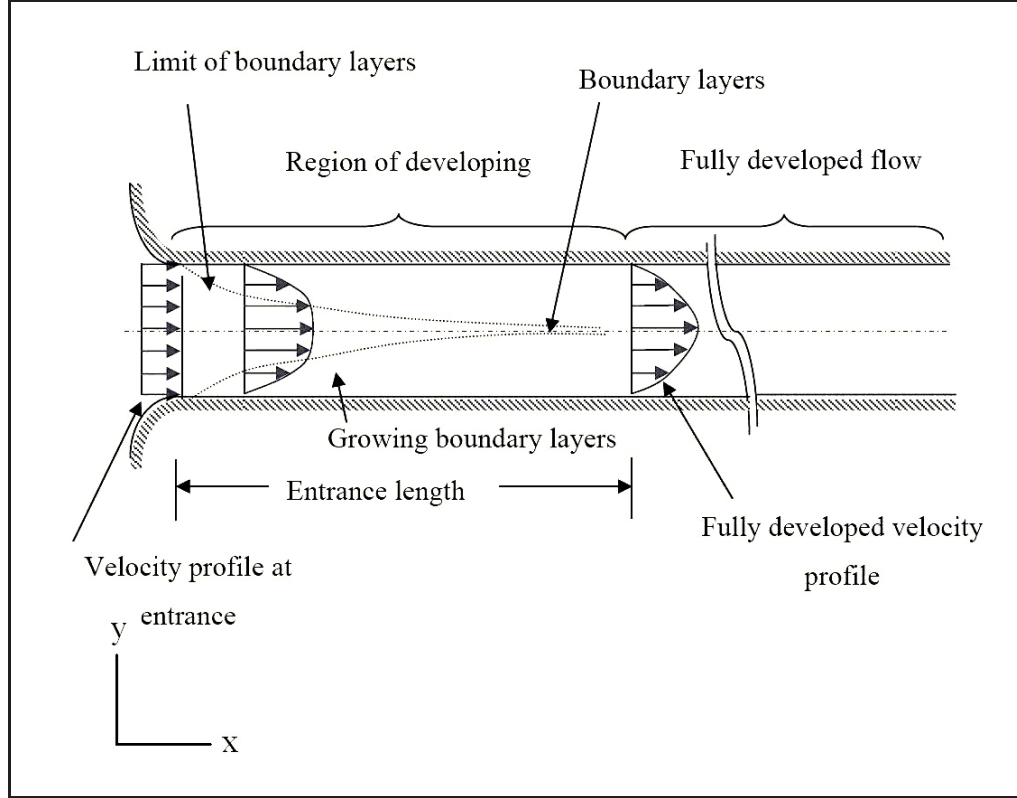


Figure 5.2: Velocity profile development from entrance region [6].

nel the flow experience convective acceleration, in which the flow in the center of the channel accelerates and the fluid at the walls decelerate according to the momentum Equation (5.2.6).

Boundary layers form as depicted in Figure 5.2. These boundary layers thicken downstream due to viscous effects. Boundary layers will thicken to a point where they meet. At this point the flow is fully developed and the velocity profile is unidirectional and independent of position. The distance from the entrance to the point where the boundary layers meet is known as the entrance length.

When the flow is fully developed, laminar and steady, the velocity profile is parabolic with a maximum value equal to one and a half times the mean velocity value, as depicted in Figure 5.3(a).

In the absence of y and z - direction velocities the Navier-Stokes Equations (5.2.7) can be simplified to

$$\rho \left(\frac{\partial u}{\partial t} + u \frac{\partial u}{\partial x} \right) = -\frac{\partial p}{\partial x} + \mu \left(\frac{\partial^2 u}{\partial x^2} + \frac{\partial^2 u}{\partial y^2} + \frac{\partial^2 u}{\partial z^2} \right) + \rho g_x , \quad (5.3.1)$$

Since there are no free surfaces and density is a constant the gravity term is cancelled by hydrostatic pressure. Assuming the flow is steady and laminar Equation (5.3.1) is therefore reduced

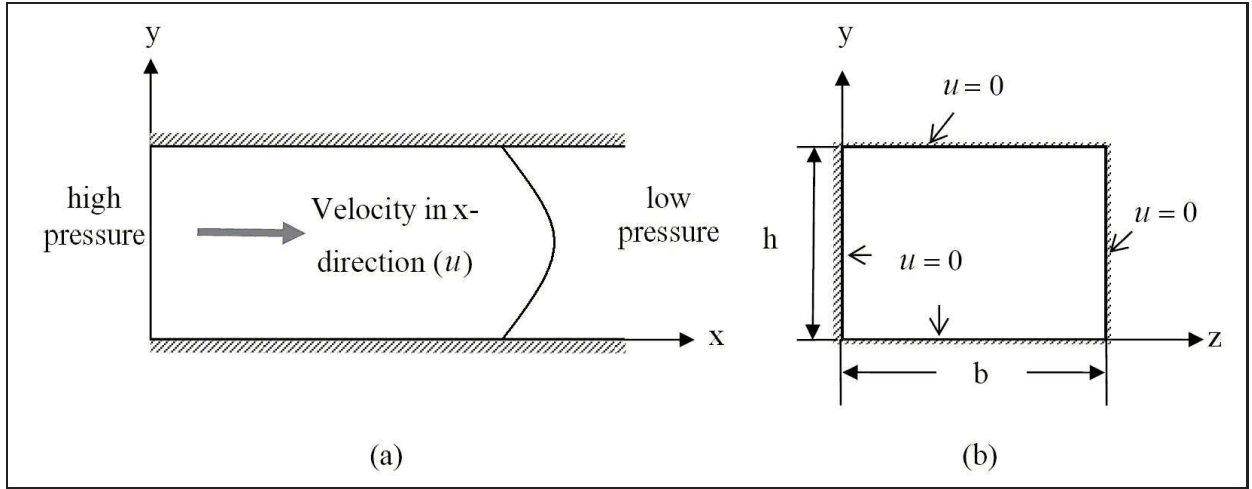


Figure 5.3: (a) Longitudinal view of microchannel with fully developed velocity profile, and (b) cross-sectional view of microchannel.

to become the Poisson's equation [21]

$$\frac{\partial^2 u}{\partial y^2} + \frac{\partial^2 u}{\partial z^2} = \frac{1}{\mu} \frac{\partial p}{\partial x} . \quad (5.3.2)$$

For shear rates less than 10^{12}s^{-1} Equation (5.3.2) can be solved analytically by introducing the no-slip boundary condition where $u = 0$, as depicted in Figure 5.3(b) [21].

Although Equation (5.3.2) can be solved analytically to obtain the velocity profile in a non-circular channel, there is little need for an exact solution as the focus of this chapter is not constant cross section area flows but velocity profiles in a converging or diverging channel.

5.4 Diffusers and nozzles

Diffuser and nozzle flow characteristics is the foundation of the valveless micropump, as explained in Section 2.2.4.3. They rectify the flow direction and govern both stability and efficiency in a valveless micropump.

The diffuser is a microchannel with a gradually expanding cross-section whilst the nozzle has a gradually contracting cross-section as depicted in Figure 5.5. The function of the diffuser is to transform kinetic energy (velocity) into potential energy (pressure) in inviscid flows.

The difference in flow resistances can be explained by studying the flow through a diffuser. The local wall shear stress is defined by

$$\tau_w \equiv \tau(y=0) = \mu \left. \frac{\partial u}{\partial y} \right|_{y=0} . \quad (5.4.1)$$

where

- μ is the dynamic viscosity of the fluid,
- u is the velocity of the fluid along the boundary, and

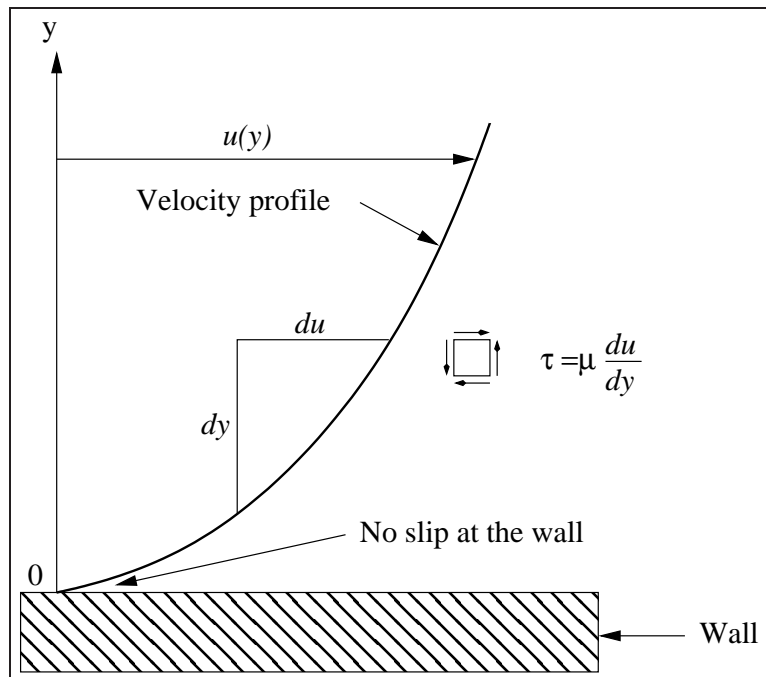


Figure 5.4: Newtonian shear stress distribution near the wall.

- y is the height of the boundary.

Shear stress in fluids are given as [9; 21; 30; 31]

$$\tau(y) = \mu \frac{\partial u}{\partial y}, \quad (5.4.2)$$

Examining a typical velocity profile as depicted in Figure 5.4 and considering Equations (5.4.2) and (5.4.1), it is observed that a large velocity gradient will produce a large shear force on the fluid, increasing the flow resistance on the flow.

During diffuser flow the main flow separates from the sidewalls and backflow occurs as depicted in Figure 5.5. The backflow is limited to the sidewalls of the diffuser and reduces the shear stress at the side wall as graphically illustrated in Figure 5.5. The fluid also decelerates and the pressure increases upstream.

When the flow is reversed the diffuser acts as a nozzle and no separation occur at the side-walls. The shear stress of the fluid increase as the velocity of the fluid increases along the nozzle.

Two types of diffusers/nozzles can be distinguished, flat-walled and conical as depicted in Figure 5.6. The advantages of space and size of the flat-walled diffuser over the conical diffuser is described in Section 4.4. This section therefore only evaluates the flat-walled or planar diffuser.

Diffuser flow can also be described by a stability map for as depicted in Figure 5.7. The stability map describes operation modes for different diffuser geometries for high Reynolds number flows i.e. turbulent flows [8]. Although the stability map describes diffuser performance for turbulent flows, the map offers valuable insight into the operation of a diffuser. The no-stall region occurs when flow is steady and viscous with no separation at the diffuser walls, diffuser performance is relatively good in this region. Transitory-stall is reached when flow is unsteady

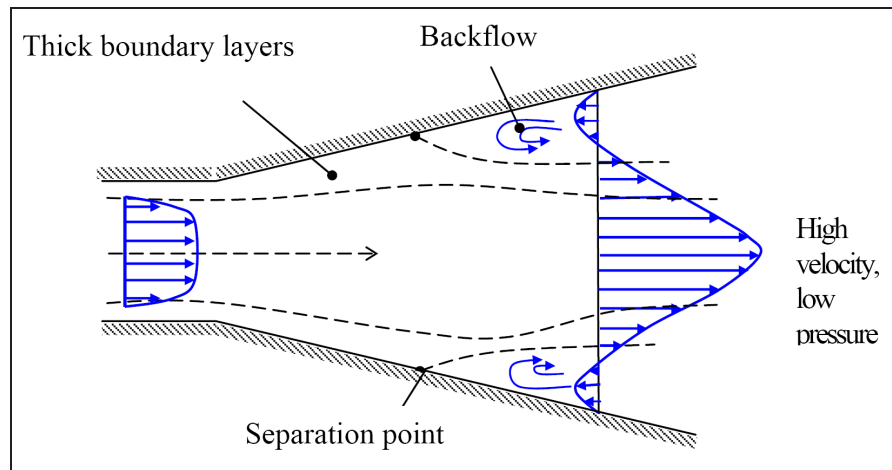


Figure 5.5: Schematic presentation diffuser flow [6].

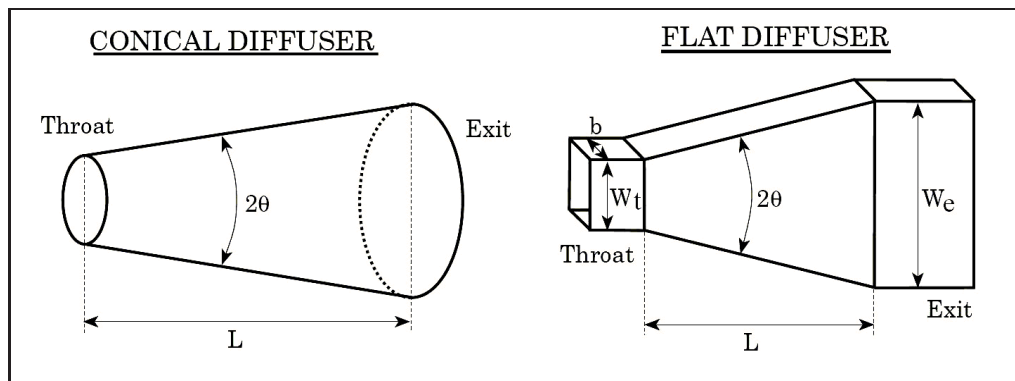


Figure 5.6: Conical and flat-walled diffusers [7].

and pressure loss is a minimum. Bistable steady-stall flow occurs when the flow flip-flops between diffuser walls and performance is poor in this region. Flow is said to be in the jet flow region when it separates completely from the diffuser walls and passes through at a near constant cross-sectional area [9].

5.4.1 Jeffery-Hamel flow in a wedge-shaped region

Diffuser and nozzle flow is presented here in polar coordinates for a wedge shaped region. This section presents one specific numerical solution to Jeffery-Hamel flow as given by White [32].

When the flow is assumed to be purely radial the momentum equation is reduced to a third-order, non-linear ordinary differential equation. The problem, although a boundary value problem, is solved here numerically using Matlab's Runge-Kutta initial value problem solver i.e. "ode45".

As depicted in Figure 5.8, the flow is considered in polar coordinates r, θ , generated by a line source at the origin as presented by White [32]. The flow in the diffuser is considered to be purely radial, $u_\theta = 0$ and bounded by the sidewalls at $\theta = \pm\alpha$.

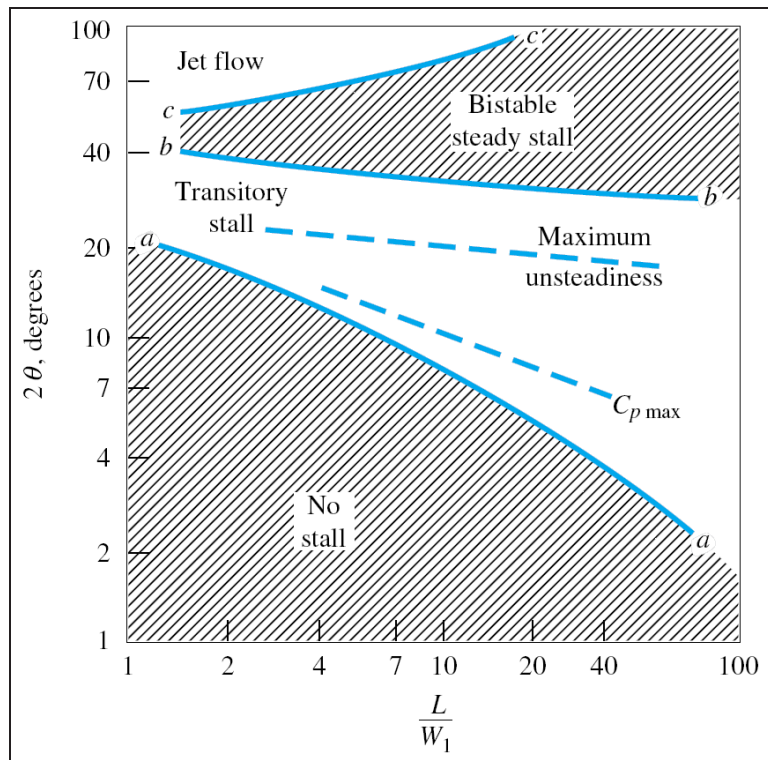


Figure 5.7: Stability map of a typical diffuser [8; 9].

The continuity equation in polar coordinates as given by [32]

$$\frac{1}{r} \frac{\partial}{\partial r} (r u_r) = 0 \quad (5.4.3)$$

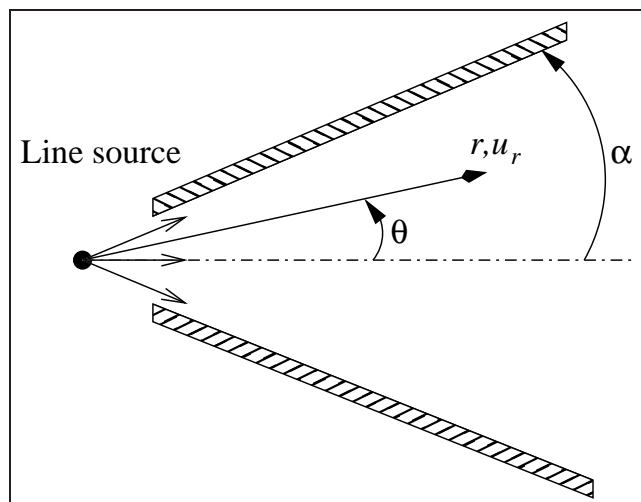


Figure 5.8: Geometry and parameters of Jeffery-Hamel flow.

If u_r have a local maximum at $\theta = 0$, then a nondimensionalization for the problem is

$$\eta = \frac{\theta}{\alpha} , \quad (5.4.4)$$

and

$$f(\eta) = \frac{u_r}{u_{max}} . \quad (5.4.5)$$

The momentum equation in polar coordinates for $u_\theta = 0$ is given by [32]

$$\begin{aligned} u_r \frac{\partial u_r}{\partial r} &= -\frac{1}{\rho} \frac{\partial p}{\partial r} + \nu \left(\frac{\partial^2 u_r}{\partial r^2} + \frac{1}{r} \frac{\partial u_r}{\partial r} - \frac{u_r}{r^2} + \frac{1}{r^2} \frac{\partial^2 u_r}{\partial \theta^2} \right) , \\ 0 &= -\frac{1}{\rho r} \frac{\partial p}{\partial \theta} + \frac{2\nu}{r^2} \frac{\partial u_r}{\partial \theta} . \end{aligned} \quad (5.4.6)$$

Pressure is eliminated by cross differentiation and introducing the variables from Equation (5.4.4), (5.4.5). The result is a third-order non-linear ordinary differential equation for the velocity profile f

$$f''' + 2Re\alpha f f' + 4\alpha^2 f' = 0 , \quad (5.4.7)$$

where $Re = u_r r \alpha / \nu$ is the characteristic Reynolds number for the flow presented. Flow is assumed to be symmetric and a no slip boundary condition is applied at the walls. As mentioned u_{max} is at $\theta = 0$. The initial and boundary values can thus be summarized by

$$\begin{aligned} f(+1) &= f(-1) = 0 , \\ f(0) &= 1 , \\ f'(0) &= 0 . \end{aligned} \quad (5.4.8)$$

Equation (5.4.7), combined with initial and boundary values from (5.4.8), is solved numerically using Matlab's Runge-Kutta solver i.e. "ode45" as illustrated by [33]. Equation (5.4.7) is solved for a range of $Re\alpha$ values. The chosen values represent the various $Re\alpha$ values encountered in the micropump. The solutions are plotted for $Re\alpha = -100, -10, -1, 0, 1, 5, 10, 15, 20, 30, 40$ and are graphically illustrated in Figures 5.9, 5.10. When $Re\alpha \leq 0$ the flow is in the nozzle direction and when $Re\alpha > 0$ the flow is in the diffuser direction.

For this specific case, with $\alpha = 3.5^\circ$, solutions to the velocity profile is found at a range of $Re\alpha$ values. Large velocity profile gradients are found near the wall when $Re\alpha < 0$ (nozzle flow), as depicted in Figure 5.10. These gradients correspond to large shear stresses at the walls.

The velocity profile gradients decrease when $Re\alpha$ increase to a point where separation occurs, in this case $Re\alpha \approx 9$. At this point the wall shear stress is diminished or $df/d\eta = 0$ as depicted in Figure 5.9. A further increase in the value of $Re\alpha$ cause the velocity profiles to be S-shaped and backflow at the wall is present.

5.4.2 Micropump efficiency

Designers and engineers often have to rely on a numerical approach and or experimental studies for design and optimization. The diffuser and nozzle dictates the efficiency of the micropump, and is the focus of this section.

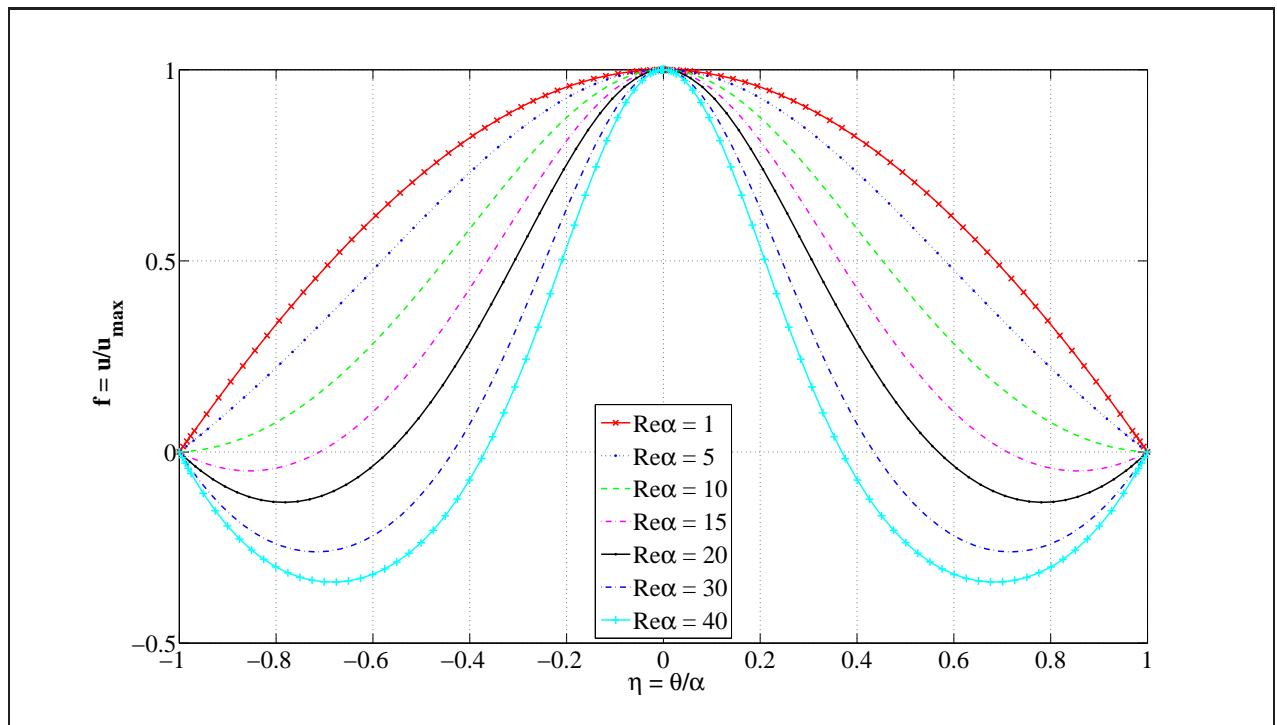


Figure 5.9: A numerical solution to Equation (5.4.7) for $Re\alpha > 0$ and $\alpha = 3.5^\circ$.

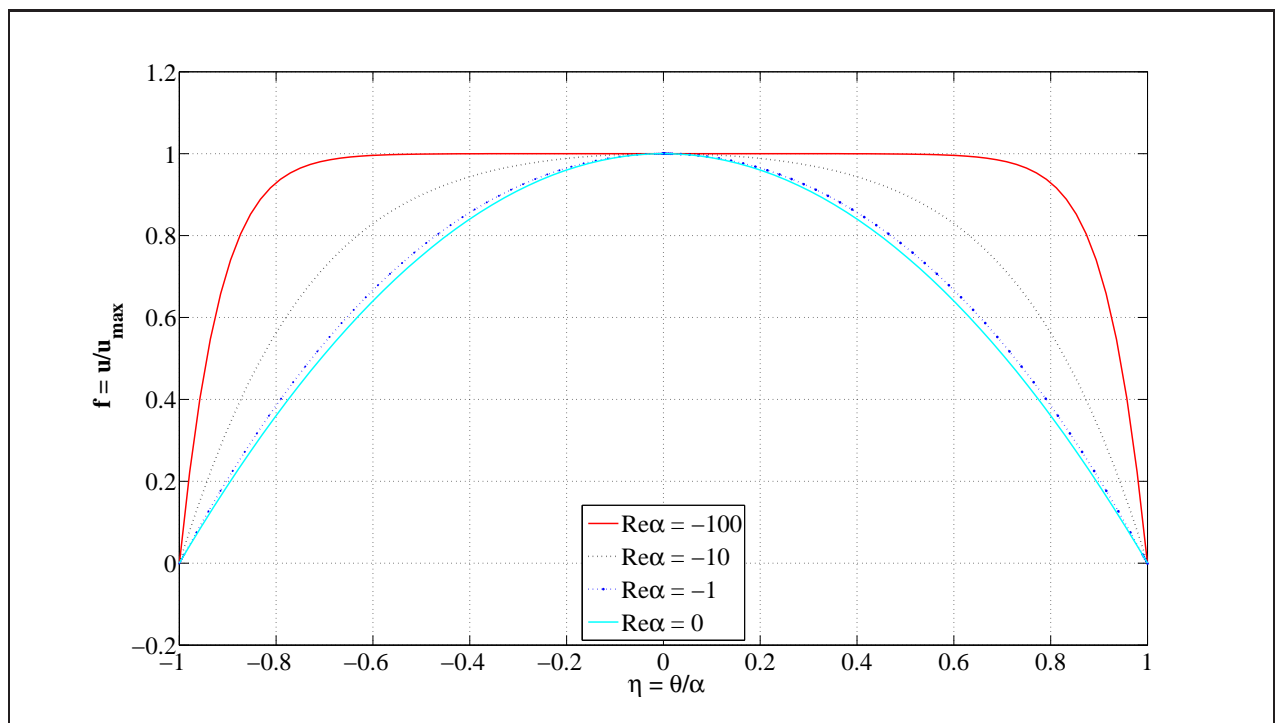


Figure 5.10: A numerical solution to Equation (5.4.7) for $Re\alpha \leq 0$ and $\alpha = 3.5^\circ$.

A measure of the efficiency for the diffuser is a dimensionless coefficient, called the diffuser pressure loss coefficient K_d [9], and is defined as [1; 26; 34; 35; 36]

$$K_d = \frac{\Delta p_d}{\frac{1}{2}\rho\alpha_e V_c^2} , \quad (5.4.9)$$

where ρ is the fluid density, V_c is the characteristic velocity of the flow, Δp_d is the pressure difference over the diffuser, and α_e is the kinetic energy correction factor and usually equal to one for turbulent flows but equal to two for laminar flow in a channel.

Similarly, K_n for a nozzle is defined as [10]

$$K_n = \frac{\Delta p_n}{\frac{1}{2}\rho\alpha_e V_c^2} , \quad (5.4.10)$$

where, Δp_n = pressure difference over the length of the nozzle. These definitions imply interaction between pressure and velocity. Equations (5.4.9) and (5.4.10) are valid for inviscid flows, but invalid for creeping flow as set out by Equation (5.2.8). In the case of creep flow there are added losses i.e. frictional losses and these losses may dictate the losses in the diffuser. Definitions in Equation (5.4.9) and (5.4.10) fail to adjust for viscous forces and can therefore not be used when $Re \ll 1$.

Pressure loss coefficients as defined in Equations (5.4.9) and (5.4.10) consist of three areas of pressure loss:

$\Delta p_{d,en}$ - pressure losses due to sudden contraction at the entrance of the diffuser,

Δp_d - pressure losses due to viscous flow in the expanding cross-section, and

$\Delta p_{d,ex}$ - pressure losses due to sudden expansion at the exit of the diffuser.

The total pressure loss can then be written as

$$\Delta p_{d,total} = \Delta p_{d,en} + \Delta p_d + \Delta p_{d,ex} , \quad (5.4.11)$$

and using Equations (5.4.9) and (5.4.11), the total pressure loss coefficient for a diffuser can be written as

$$\begin{aligned} K_{d,total} &= K_{d,en} + K_d + K_{d,ex} \\ &= \frac{\Delta p_{d,en}}{\frac{1}{2}\rho\alpha_e V_c^2} + \frac{\Delta p_d}{\frac{1}{2}\rho\alpha_e V_c^2} + \frac{\Delta p_{d,ex}}{\frac{1}{2}\rho\alpha_e V_c^2} \\ &= \frac{\Delta p_{d,total}}{\frac{1}{2}\rho\alpha_e V_c^2} . \end{aligned} \quad (5.4.12)$$

Hence, for a given diffuser geometry, the pressure loss coefficient can be estimated from the pressure drop and the mean velocity at the neck of the diffuser. However, these equations are largely simplified and usually intended for use in conventional high Reynolds number flow diffusers. Therefore determining the pressure drop inside the diffuser or $\Delta p_{d,total}$ requires a numerical or experimental approach.

The diffuser efficiency η_{nd} for a nozzle-diffuser element is defined as the ratio of the total pressure loss coefficient for flow in the nozzle direction to that for the flow in the diffuser direction [10], i.e.

$$\eta_{nd} = \frac{K_{n,total}}{K_{d,total}} . \quad (5.4.13)$$

Thus, η_{nd} should be greater than one to provide a net flow rate in the diffuser direction. If η_{nd} is equal to one there is no net flow rate due to equal pressure drop in both directions. When η_{nd} is smaller than one the net flow is in the nozzle direction.

5.4.3 Experimental analysis

Despite the fundamental simplicity of laminar flow in straight ducts, experimental studies of microscale flow have often failed to reveal the expected relationship between the friction factor and Reynolds number [21]. Subsequently designers and engineers have to rely on seemingly contradicting data for diffuser designs.

Maximum pressure recovery (C_p) as depicted in Figure 5.7 is illustrated graphically in Figure 5.11 as a experimental study and provides information on the performance of the diffuser element. Although intended for very high Reynolds number flows, Figure 5.11 can be utilized to aid the design process and provide an estimate of parameter influences. However, it should be emphasised that the data presented in Figure 5.11 is at best a crude estimate and [34; 36; 10] provided data that suggested major differences when the Reynolds number approached $Re \leq 100$. Little data exists for planar diffuser performance at $Re \leq 10$, Figure 5.12 depicts performance data of a planar diffuser for a range of Reynolds numbers.

These performance maps provide engineers with an first iteration of when choosing initial design parameters. Combined with data of Figure 5.12 and expressions derived in the previous sections, serves as basis of understanding the design and operation of a diffuser / nozzle micropump.

5.4.4 Dimensional analysis using Buckingham π -theorem

The goal of the dimensional analysis is to determine the most significant dimensionless functional relationships between the various design parameters and flow rate. Consider the parameters of the diffuser as given by Figure 4.3, the functional relationship for the flow rate can be expressed as

$$\bar{Q} = F(\Delta p, f, \rho, \mu, L, h, W_t, W_e, r_t, r_e) , \quad (5.4.14)$$

where

\bar{Q} = mean averaged flow rate,

Δp = the applied differential pressure,

f = excitation frequency,

μ = fluid viscosity,

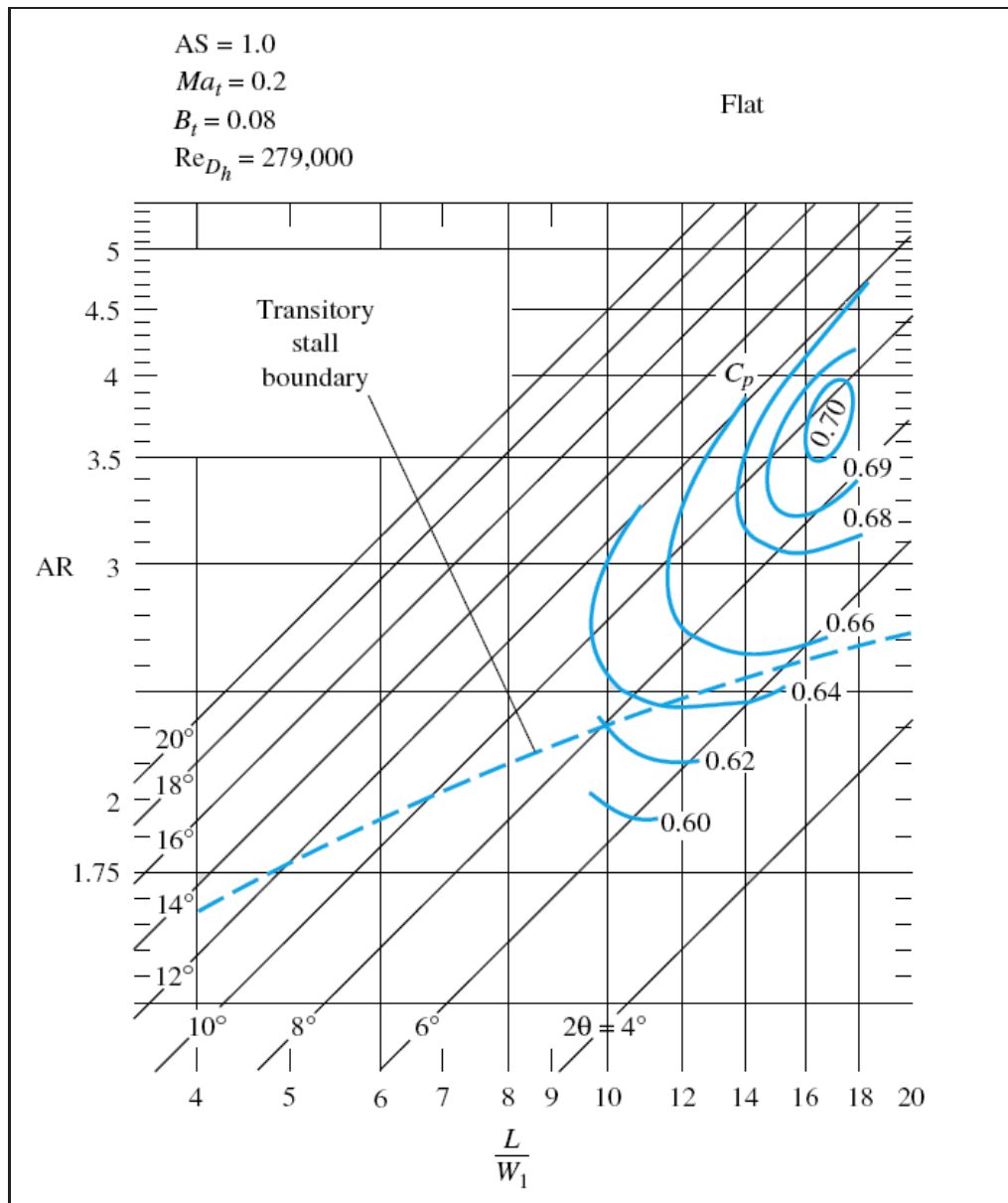


Figure 5.11: Typical diffuser performance map for flat walled diffuser under highly turbulent operating conditions [8].

L = total length of diffuser,

h = depth of diffuser,

W_t = width of the throat of the diffuser,

W_e = width of the diffuser exit,

r_t = inlet radii for the throat of the diffuser, and

r_e = outlet radii for the exit of the diffuser.

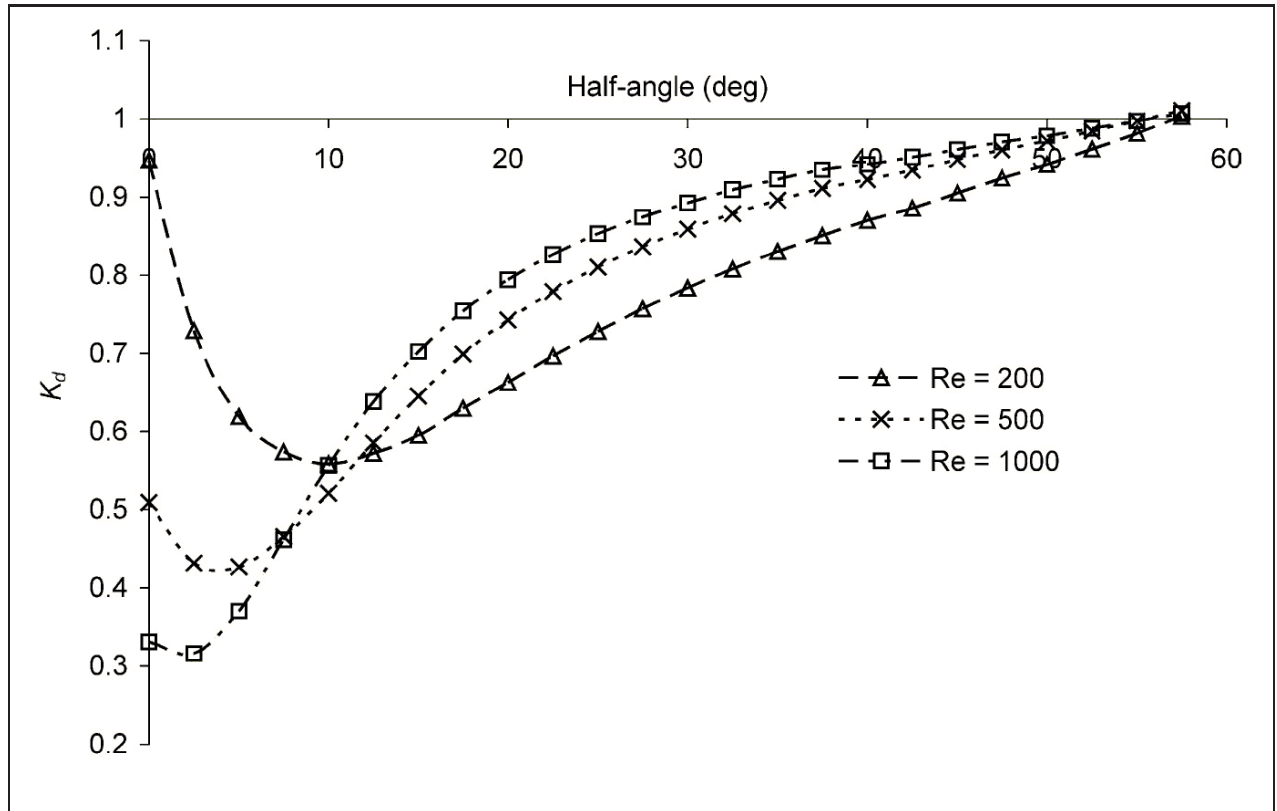


Figure 5.12: Planar diffuser performance plot for a fully developed entrance boundary layer at various Reynolds numbers [10].

The expression in (5.4.14) can be simplified using dimensional analysis. The method presented here was proposed in 1914 by Buckingham [37], and is now known as the Buckingham Pi-theorem. The theorem states that when a problem is written as a functional relationship, $Q_i = f(Q_1, Q_2, \dots, Q_n)$ in terms of n dimensional variables. These terms are physically relevant in the problem and are inter-related by an unknown dimensionally homogeneous set of equations. Then, r is the number of fundamental dimensions required to describe the n variables. The remaining $p = n - r$ variables can be expressed as p dimensionless and independent “Pi groups”. Thus any functional relationship of this form can be reduced to $\prod_i = \phi(\Pi_1, \Pi_2, \dots, \Pi_{n-r})$.

For the problem as set out in (5.4.14) there is $11 - 3 = 8$ independent dimensionless groups. The simplified equation is not unique, and one possibility for this functional relationship are

$$\frac{\rho \bar{Q}}{\mu L} = F\left(\frac{\rho L^2 \Delta p}{\mu^2}, \frac{\rho L^2 f}{\mu}, \arctan\left(\frac{W_e - W_t}{L}\right), \frac{W_e}{W_t}, \frac{h}{L}, \frac{r_t}{W_t}, \frac{r_e}{W_e}\right), \quad (5.4.15)$$

where $\alpha = \arctan\left(\frac{W_e - W_t}{L}\right)$ and $AR = \frac{W_e}{W_t}$.

Assuming that the applied pressure Δp is a property of the piezoelectric disk and not the geometry of the micropump these parameters are not considered for this investigation. As the piezoelectric disk is not the focus of the research presented, the remaining parameters are W_t , W_e , f , L , h , r_t and r_e .

Using Figure 5.12 and data from [8], it is clear that the optimal performance for diffusers angles ranges from $5^\circ \leq 2\theta \leq 10^\circ$. From this an angle of $2\theta = 7.5^\circ$ and a dimension of $W_t = 80 \mu\text{m}$ are selected for the design (which conforms with manufacturing capabilities). From these specified values and Figure 5.11, the maximum C_p is found at $\frac{L}{W_t} = 13.75$, which means $AR = 2.7$.

As the depth h of the diffuser is a constant (planar diffuser) and is bound by the manufacturing capabilities. The remaining variable parameters of Equation (5.4.15) are the inlet radii r_t and outlet radii r_e of the diffuser and the frequency of excitation f . The inlet and outlet radii of the diffuser are thus chosen as the primary concern for further investigation with the excitation frequency f the secondary concern.

Chapter 6

Numerical simulations

As pointed out in Section 5, there is no analytical solution to describe diffuser performance, this is integral for the design and optimization of the diffuser / nozzle of the micropump.

As illustrated in Section 5.4.4 the parameters under investigation is the inlet and outlet radii of the diffuser and the frequency of excitation. Other key geometric parameters are detailed in Section 5.4.4. These parameters include the inlet and outlet widths, W_t, W_e and applied pressure ΔP , data for these parameters however are available as presented by [26; 10]. It is therefore not included in this research. The approach for this chapter is to investigate the effects of the inlet and outlet radii as well as the frequency of excitation.

The CFD solver used for all simulations is Fluent 6.3.26. A pressure based solver is chosen and the SIMPLE pressure-velocity coupling scheme is selected for the analysis. The second order upwind numerical scheme is used for the momentum equation calculations. Small flow volumes is expected, the absolute convergent criteria is therefore set to 1×10^{-12} and the laminar viscous model is selected. The energy equation is switched off for the simulations. Fluid properties of water at 20°C is used for the fluid.

6.1 Method

The simulation approach is to construct a two-dimensional model of the micro-diffuser element and simulate steady state flow in both the nozzle and diffuser direction. The two-dimensional model is solved to test mesh dependancy and provide provide data on the flow directing capabilities of the diffuser/nozzle element configuration. The mesh is refined after each successful simulation. Mesh bi-section is used to refine the mesh and the optimum mesh settings are extrapolated to the three-dimensional model.

Due to mesh sizes in excess of 3.2×10^6 cells the models are simulated using a parallel processing HPC Linux cluster with 21 computing nodes. The head node specification is:

- Amount: 1,
- Model: X4150,
- Processors: 1 x E5410 (2.33GHz) Harpertown 45 nm Quad-core,
- Memory: 4GB FBDIMM, and

- I/O: 2 x 146GB 10000 rpm 2.5" SAS.

The computing nodes specification is:

- Amount: 21,
- Model: X4150,
- Processors: 2 x E5440 (2.83GHz) Harpertown 45 nm Quad-core,
- Memory: 16GB FBDIMM, and
- I/O: 2 x 146GB 10000 rpm 2.5" SAS.

The total cluster specifications is a CPU count of 168 cores @ 2.83GHz, the total RAM is 336GB, I/O is 12.1TB and the theoretical performance is 2 Terra flops. The operating system used is OpenSUSE 10.3.

6.2 Model

Working under the assumption that the flow is extensively laminar ($1 \ll Re \leq 1000$), a laminar viscous model is used for both two-dimensional steady state and three-dimensional transient analyses.

The estimated force of the piezoelectric disk is converted to a pressure and applied to both the two-dimensional and the three-dimensional model.

6.2.1 Model setup: Two-dimensional

The analyzed two-dimensional model as depicted in Figure 6.1, consist of a section of the designed three-dimensional micropump. The main dimensions as derived from diffuser data in Section 5.4.3 and manufacturing limitations is $L = 1100 \mu\text{m}$, $W_t = 80 \mu\text{m}$ and $W_e = 236 \mu\text{m}$. The depth of the two-dimensional model is unity.

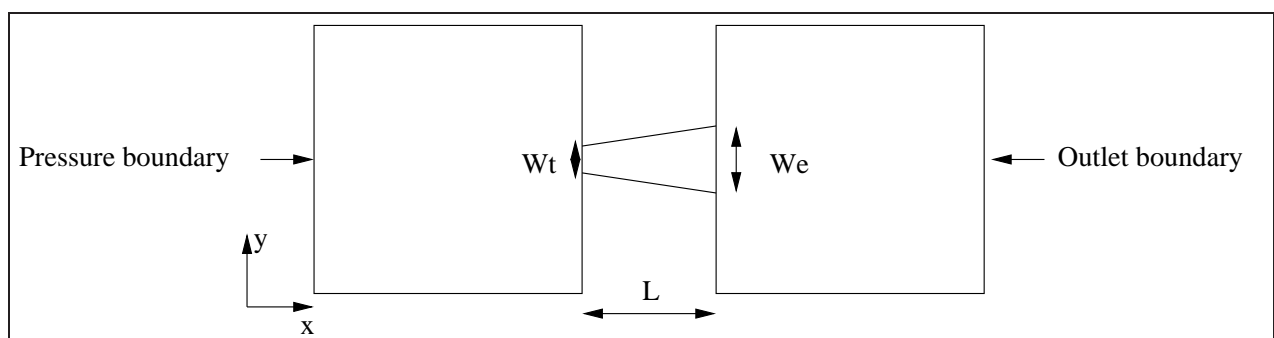


Figure 6.1: Two-dimensional layout of the diffuser element model.

The Fluent 6.3.26 solver settings for the two-dimensional steady state model is:

- **Solver** - Pressure based,

- **Viscous model** - Laminar,
- **Pressure velocity coupling** - SIMPLE,
- **Fluid** - Water @ 20°C,
- **Boundary conditions at the inlet** - Constant pressure @ 100 kPa,
- **Boundary conditions at the outlet** - Zero pressure boundary,
- **Boundary conditions at the walls** - No slip boundary condition,
- **Formulation** - Implicit, and
- **Gradient option** - Green-Gauss cell based.

The flow rate on the outlet boundary is calculated for each mesh size iteration and plotted.

6.2.2 Model setup: Three-dimensional

The three-dimensional model is that of the total micropump as depicted in Figure 6.2. The model has a thickness of 80 μm and the diameter of the pump chamber is 6 mm. The model

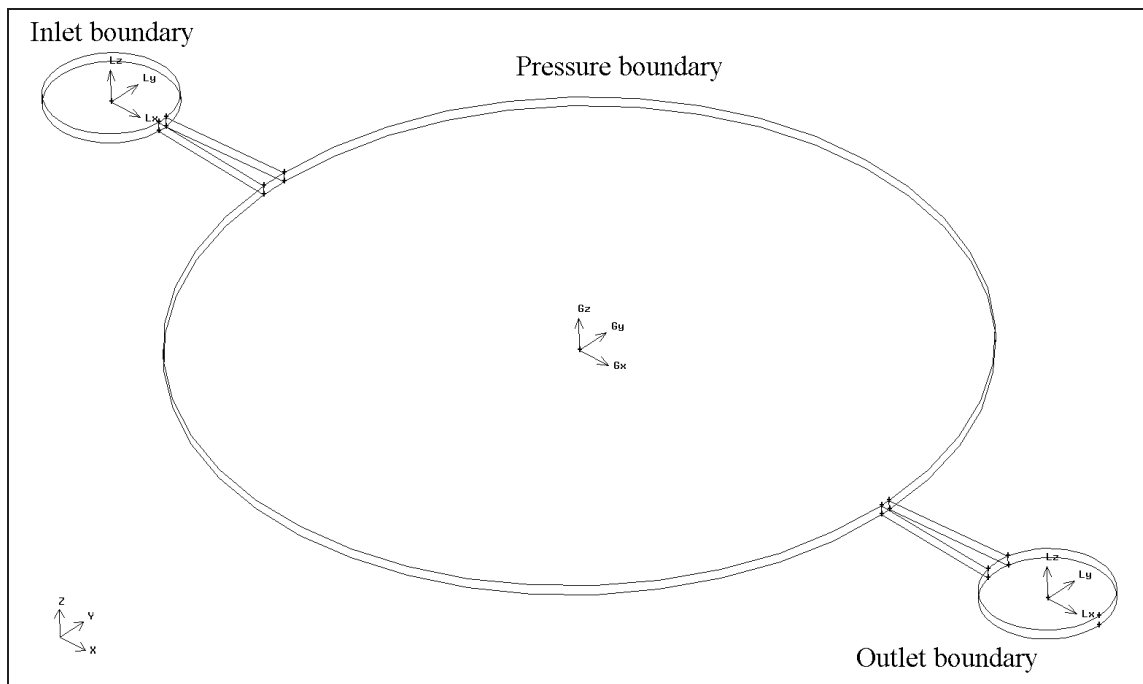


Figure 6.2: Three dimensional layout of the micropump model.

has three distinctive boundary conditions, the the pressure boundary is located at the top of the pump chamber. The other two is the inlet and outlet chambers connected by means of the nozzle/diffuser to the pump chamber as depicted by Figure 6.2.

The Fluent 6.3.26 solver settings for the three-dimensional steady state model

- **Solver** - Pressure based,
- **Viscous model** - Laminar,
- **Pressure velocity coupling** - SIMPLE,
- **Fluid** - Water @ 20°C,
- **Boundary condition for pressure** - Sinusoidal pressure function with amplitude of 100 kPa,
- **Boundary conditions at the outlet** - Zero pressure boundary,
- **Boundary conditions at the inlet** - Zero pressure boundary
- **Boundary conditions at the walls** - No slip boundary condition,
- **Formulation** - Implicit,
- **Unsteady formulation** - 2nd-Order implicit, and
- **Gradient option** - Green-Gauss cell based.

The flow rate through the inlet and outlet boundary are calculated as part of the solution. The time step Δt is reduced for the different frequency simulations in

- $f = 10$ Hz - $\Delta t = 1$ ms,
- $f = 100$ Hz - $\Delta t = 0.1$ ms, and
- $f = 1000$ Hz - $\Delta t = 0.01$ ms.

6.3 Two-dimensional analysis

The two-dimensional model is solved for five different grid sizes as part of a mesh dependence analysis. Each increment of the mesh size is four times the previous mesh size due to mesh bisection. The initial mesh size is chosen to be 12500 two-dimensional elements as depicted in Figure 6.3. The initial mesh is bi-sected four times to produce a final mesh element count of 3.2×10^6 .

The inlet and outlet flow rates are plotted in Figure 6.4 and shows both flow rates approaching a converged value. The figure also illustrates the flow directing capabilities of the diffuser element. The flow rates for the corresponding mesh sizes is given in Table 6.1.

From Table 6.1 and Figure 6.4 it's observed that the flow rates of both directions converge toward a specific value as the mesh is refined. Data from this diffuser element analysis is used to construct the mesh for the three-dimensional diffuser model.

Assuming that the last point on the graph in Figure 6.4 is the theoretical best answer, then the optimum element vs accuracy combination is when implementing 50000 elements. At this point the error is 3,5% compared to 7,5% at 12500 elements. This mesh scheme is extrapolated to the diffuser elements in the three-dimensional model. Since the mesh in the two-dimensional model is localized to the diffuser region, further mesh refinement in this region is not considered in the three-dimensional.

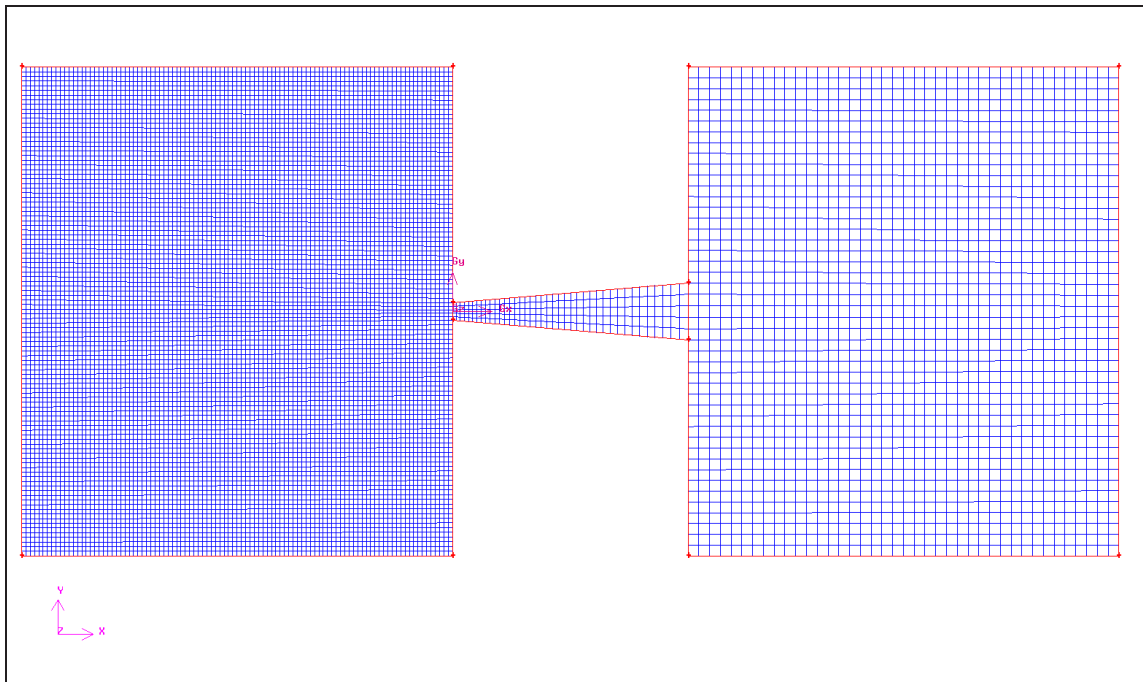


Figure 6.3: A two-dimensional mesh of the diffuser section comprising of 12500 mesh elements.

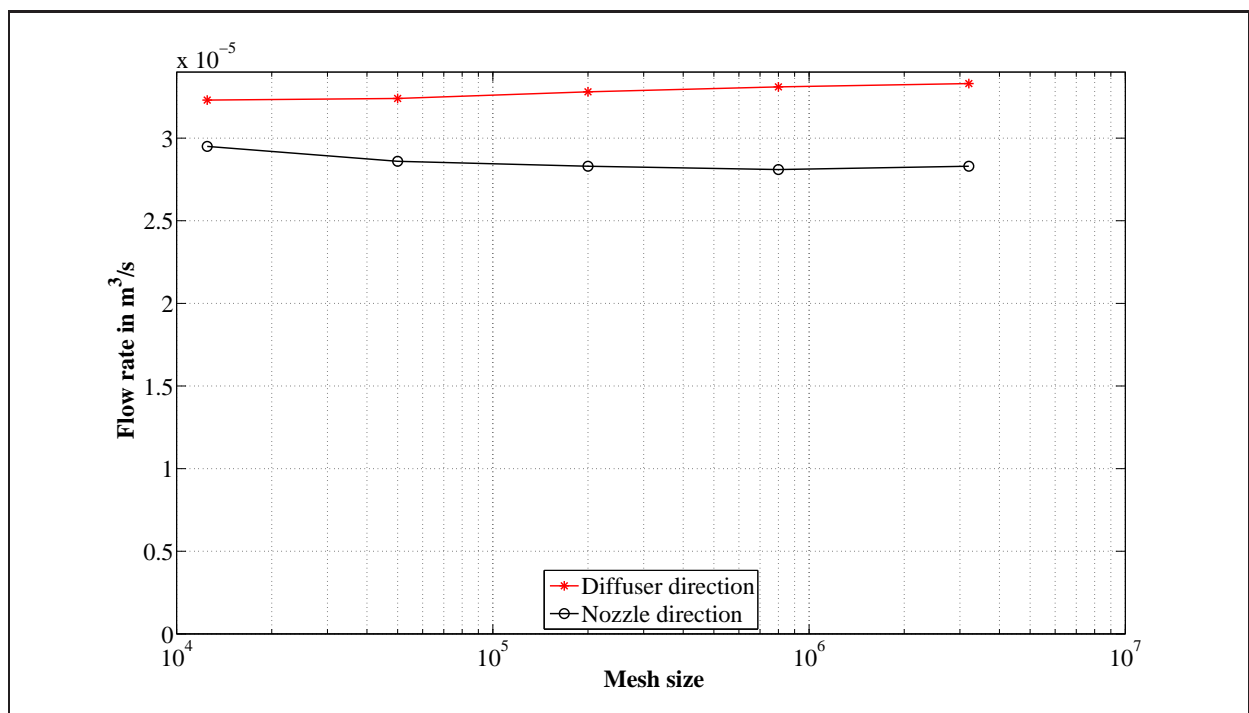


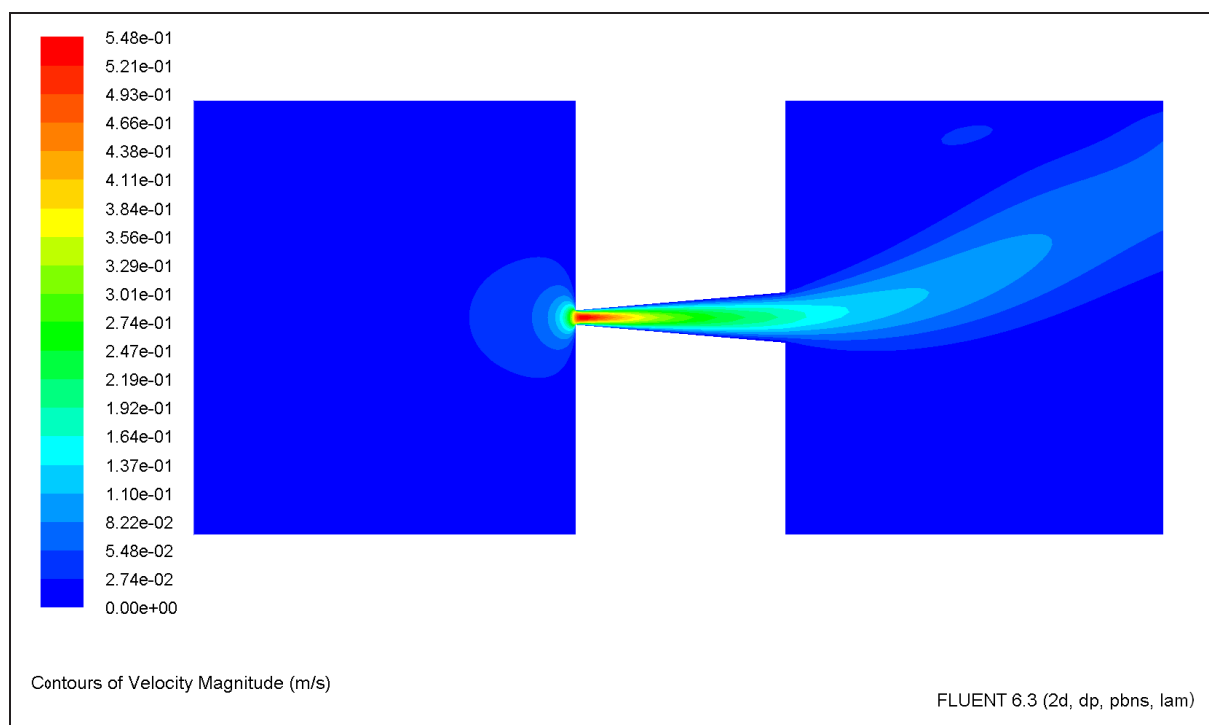
Figure 6.4: Results for number of mesh elements vs flow rate for a two dimensional steady state analysis.

Table 6.1: The exact values of mesh size vs flow rate, for diffuser and nozzle directions

Mesh elements	Diffuser (m ³ /s)	Nozzle (m ³ /s)
12500	3.23E-05	2.95E-05
50000	3.24E-05	2.86E-05
200000	3.28E-05	2.83E-05
800000	3.31E-05	2.81E-05
3200000	3.33E-05	2.83E-05

6.3.1 Results of two-dimensional analysis

This section provides results of the two-dimensional analysis in the form of velocity contour plots. Figures 6.5, 6.6 depicts the velocity contour plots of the diffuser and nozzle directions for the 8×10^5 element model.

**Figure 6.5:** Steady state velocity magnitude contours for two dimensional diffuser flow.

From Figure 6.5 the following can be observed

- the upward slope of the diffuser flow is typical of low Reynolds number flows ($Re \approx 30$) as graphically illustrated in Figure 5.7, as the bi-stable steady stall region, and
- high velocity gradients around the inlet of the diffuser.

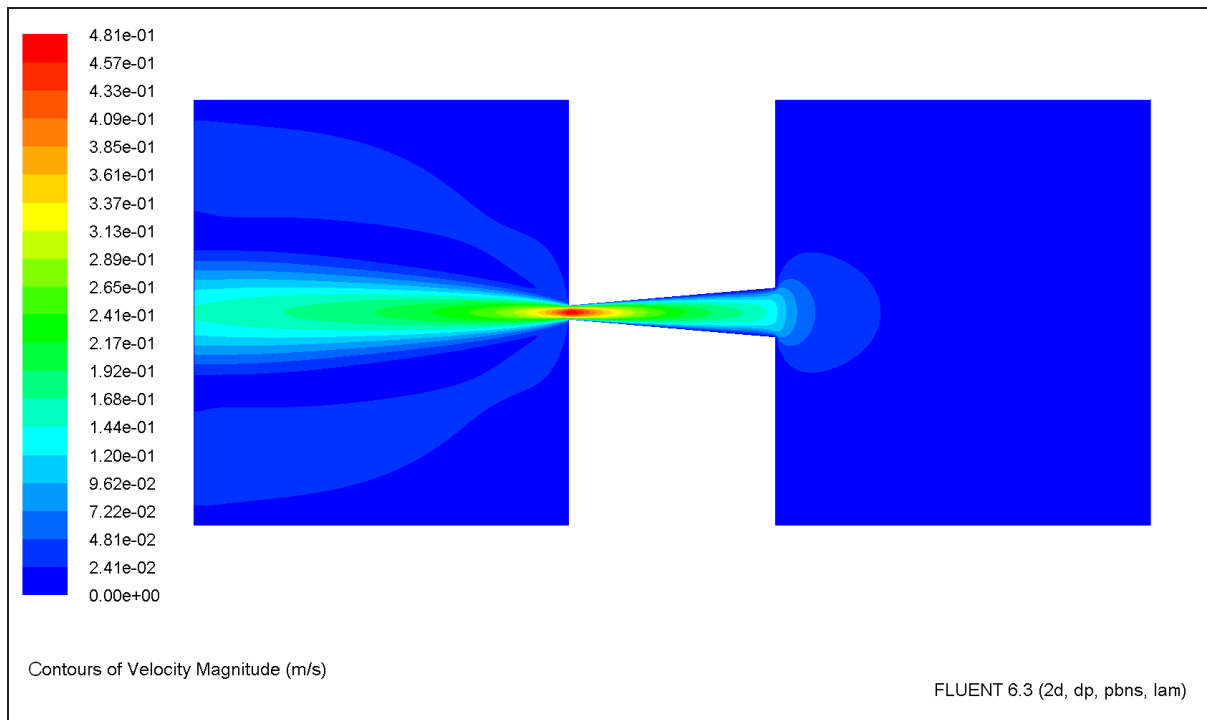


Figure 6.6: Steady state velocity magnitude contours for two dimensional nozzle flow.

From these simulations the importance of the diffuser inlet radii is highlighted by high velocity gradients around the diffuser and nozzle inlets. The simulations provides valuable data on diffuser characteristics for low Reynolds number flows.

6.4 Three-dimensional analysis

The three-dimensional model is constructed from the information gathered from the two-dimensional analysis and has 25 elements in the z -direction as depicted by Figure 6.7. The total mesh size of the three-dimensional model is 410 000 cells and simulated on eight cores or one node of the HPC. Typical run time is approximately 36 hours per cycle. Three cycles were used to calculate the flow rate. The three-dimensional model is simulated with three different inlet and outlet radii configurations as depicted in Figure 6.8 and at three different excitation frequencies of 10 Hz, 100 Hz, 1000 Hz. This frequency range is selected to provide frequency sensitivity feedback of a typical micropump configuration.

A sinusoidal pressure with amplitude of 100 kPa is applied to the pump chamber and the flowrates on the boundaries are calculated. Pressure contours, velocity gradients and velocity profiles are plotted in Appendices A.3, A.4 and A.5 respectively for one cycle.

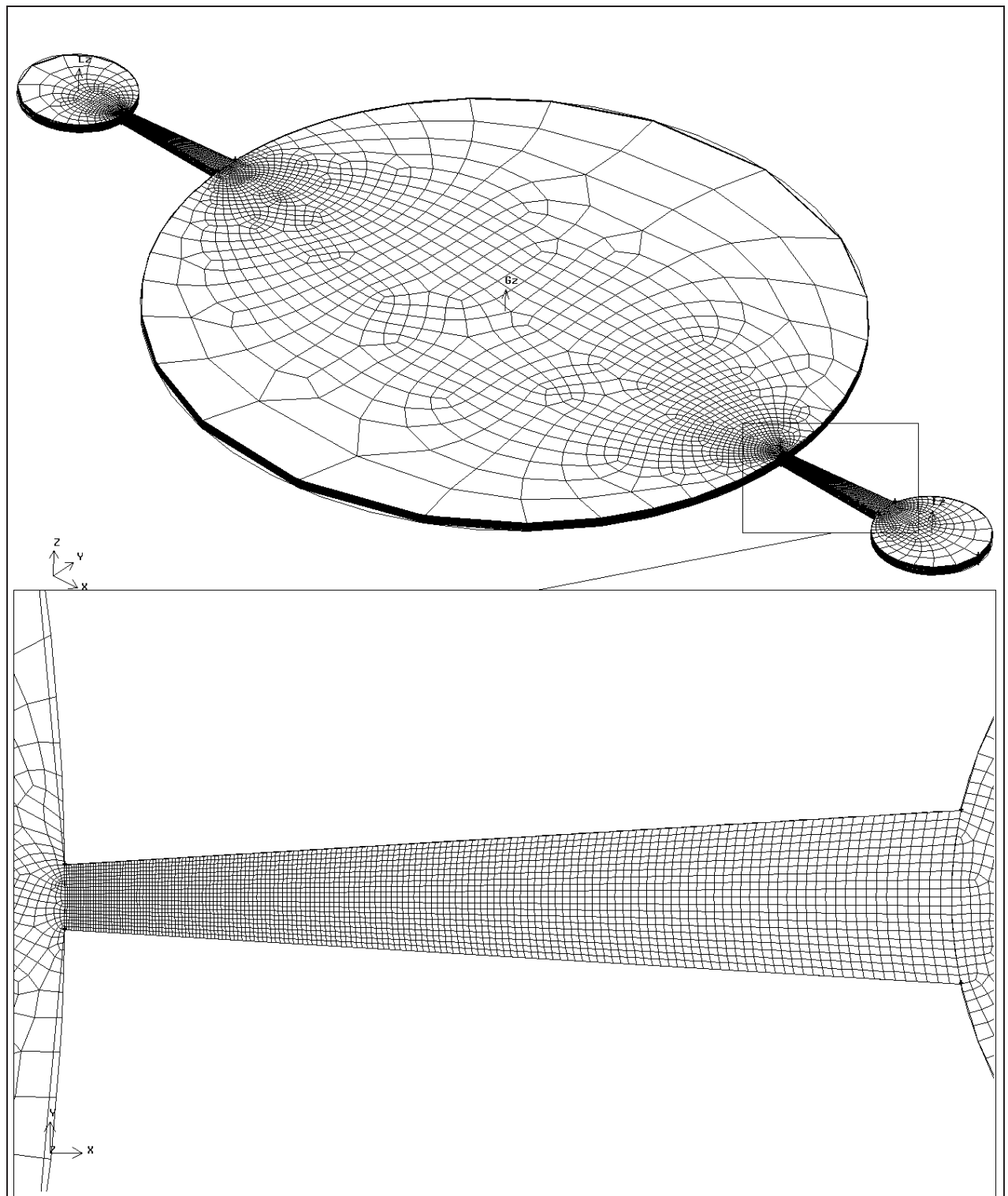


Figure 6.7: A meshed three-dimensional model showing the elements in the diffuser.

6.4.1 Sharp edged diffuser/nozzle configuration

In this model the diffuser and nozzle inlets has angles approaching 90° as depicted in Figure 6.8(a).

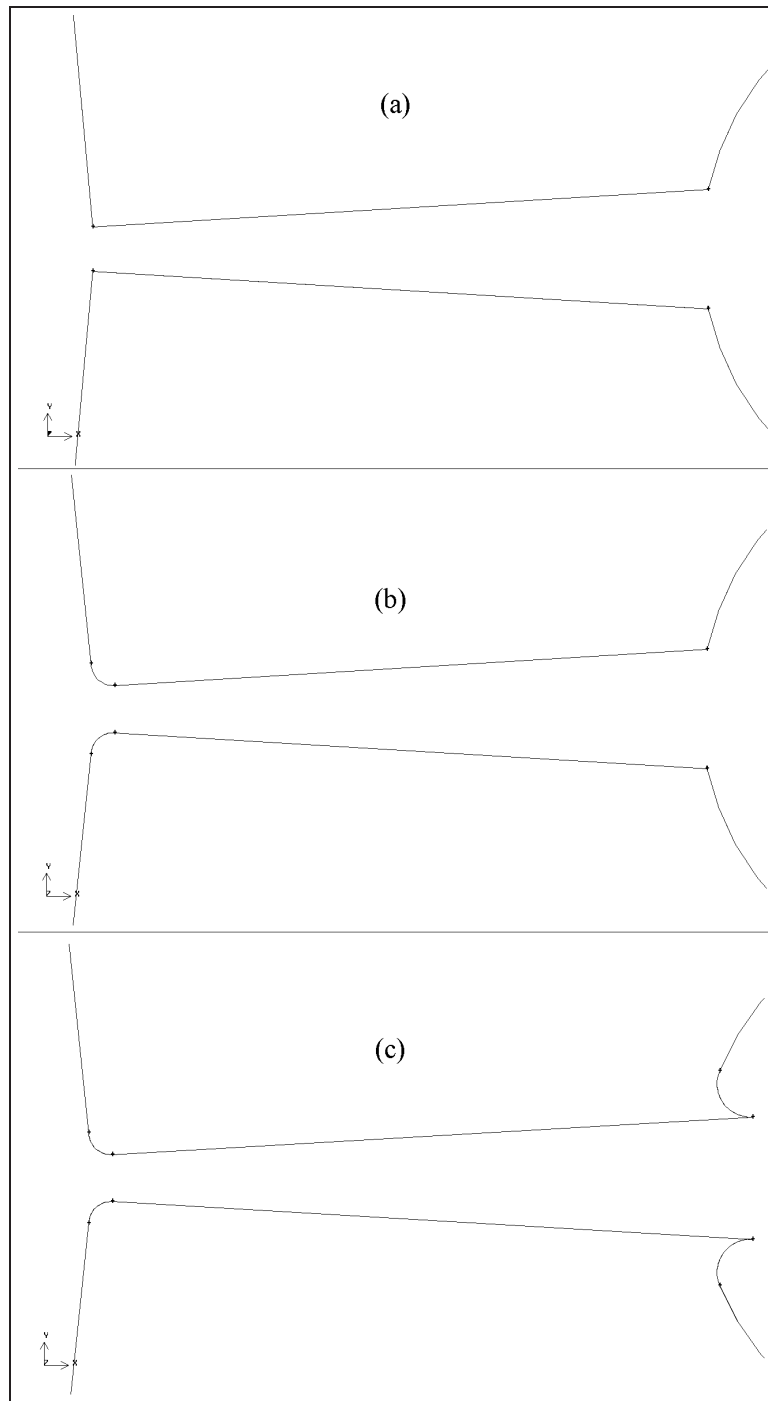


Figure 6.8: (a) An illustration of a diffuser model with sharp diffuser and nozzle inlet radii. (b) An illustration of a diffuser model with a rounded diffuser inlet edge and a sharp nozzle inlet edge. (c) An illustration of a diffuser model with a rounded diffuser inlet edge and a sharpened nozzle inlet edge.

The resulting flows rates plotted for the 10 Hz, 100 Hz and 1000 Hz are plotted in Figures 6.9, 6.10 and 6.11 respectively. Flow rates are numerically integrated for the sharp edged

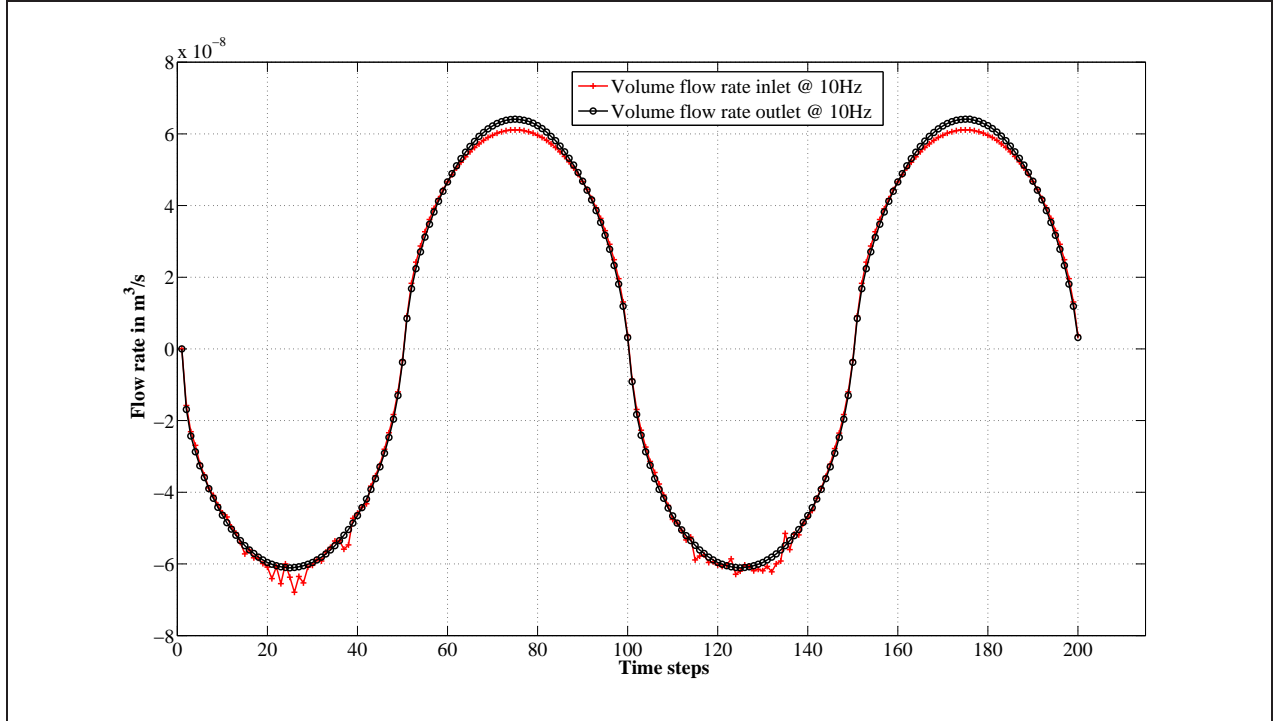


Figure 6.9: Inlet and outlet flow rates for the sharp edged diffuser nozzle configuration exited at 10 Hz for 0.2 seconds and with $\Delta t = 1$ ms.

diffuser/nozzle configuration and given as

- 10 Hz = 2038 $\mu\text{L}/\text{min}$ - nozzle direction,
- 100 Hz = 2206 $\mu\text{L}/\text{min}$ - nozzle direction, and
- 1000 Hz = 3679 $\mu\text{L}/\text{min}$ - nozzle direction.

From Figures 6.9, 6.10 and 6.11 it is observed that there is no definite flow direction and only when integrating the results, a flow rate is observed. A transient effect is also observed on the inlet flow curve, this effect is because of unstable flow caused by the nozzle flow. The effect can be resolved by decreasing the time step. The result of the decreased time step is observed in Figure 6.11.

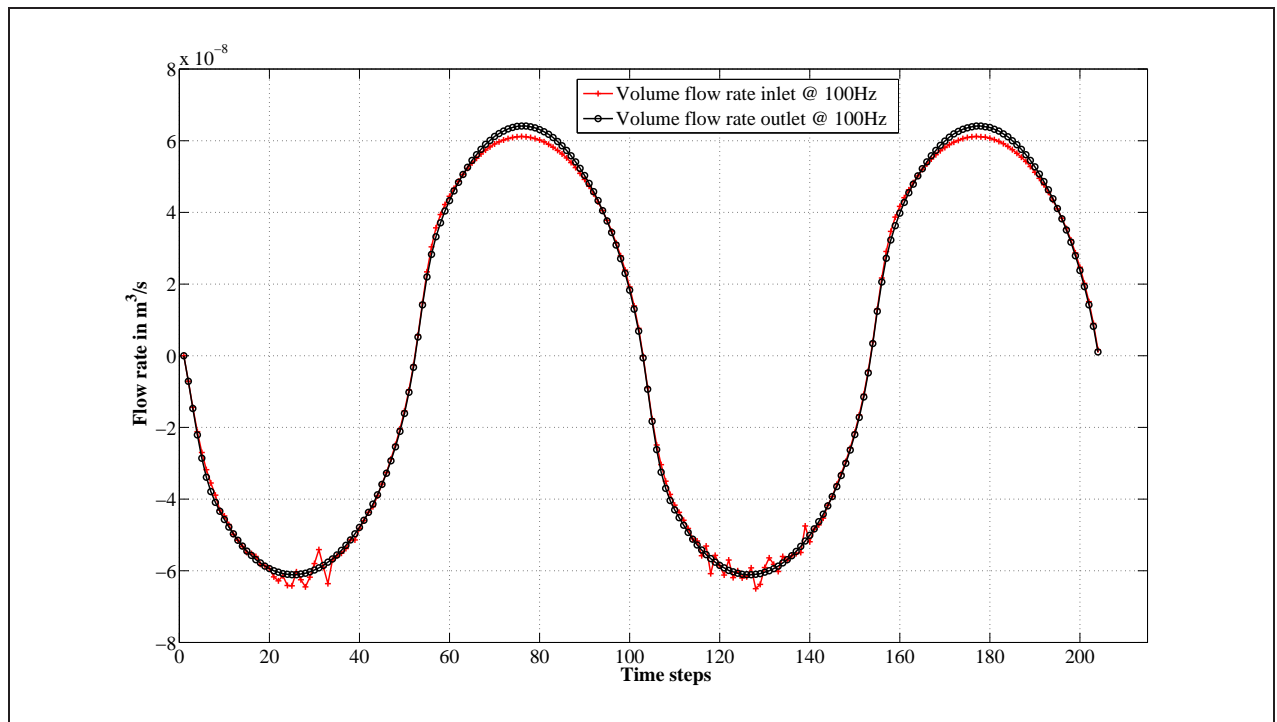


Figure 6.10: Inlet and outlet flow rates for the sharp edged diffuser nozzle configuration exited at 100 Hz for 0.02 seconds and with $\Delta t = 0.1$ ms.

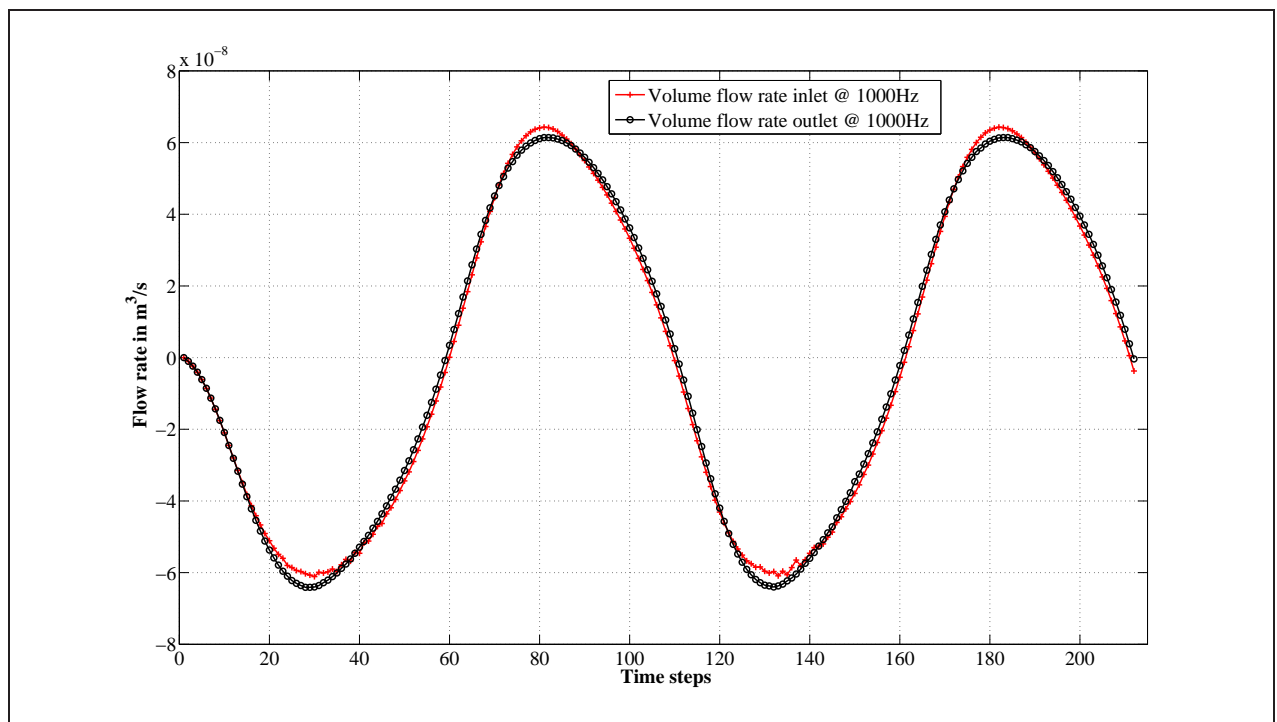


Figure 6.11: Inlet and outlet flow rates for the sharp edged diffuser nozzle configuration exited at 1000 Hz for 0.002 seconds and with $\Delta t = 0.01$ ms.

6.4.2 Round edged diffuser/nozzle configuration

This model has a rounded inlet edge, $r_t = 40 \mu\text{m}$, for diffuser flow and a sharp inlet edge, angles approaching 90° , for the nozzle flow as depicted in Figure 6.8(b).

The resulting flows rates plotted for the 10 Hz, 100 Hz and 1000 Hz plotted in Figures 6.12, 6.13 and 6.14 respectively. Flow rates are numerically integrated for the rounded edged diffuser/nozzle

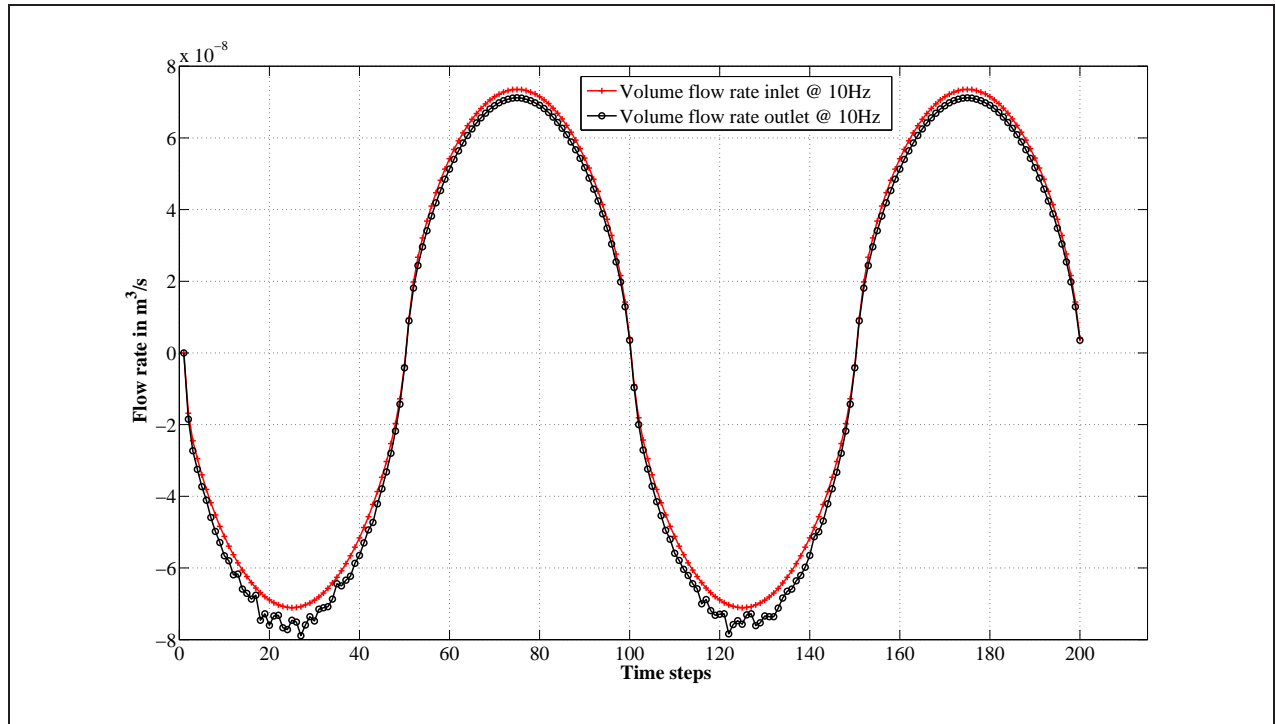


Figure 6.12: Inlet and outlet flow rates for the rounded diffuser inlet and sharp nozzle inlet configuration exited at 10 Hz for 0.2 seconds and with $\Delta t = 1 \text{ ms}$.

configuration and given as:

- 10 Hz = 8384 $\mu\text{L}/\text{min}$ - diffuser direction,
- 100 Hz = 8080 $\mu\text{L}/\text{min}$ - diffuser direction, and
- 1000 Hz = 8635 $\mu\text{L}/\text{min}$ - diffuser direction.

From Figures 6.12, 6.13 and 6.14 it is observed that there is a definite flow direction in the diffuser direction. As in the sharp edged model, a transient effect is also observed on the inlet flow curve, but much less prominent as in the sharp edged model's case, due to the diffuser rounding stabilizing the flow. This effect can also be resolved by decreasing the time step. The result of the decreased time step is observed in Figure 6.14.

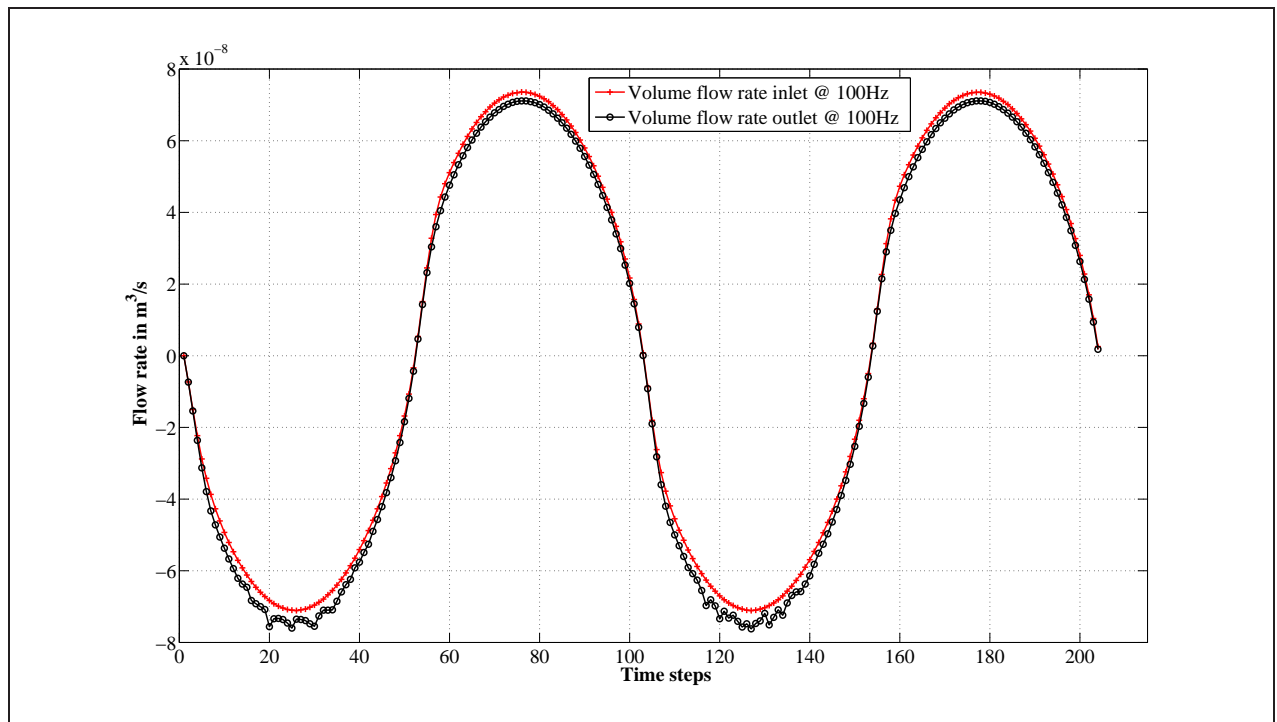


Figure 6.13: Inlet and outlet flow rates for the rounded diffuser inlet and sharp nozzle inlet configuration exited at 100 Hz for 0.02 seconds and with $\Delta t = 0.1$ ms.

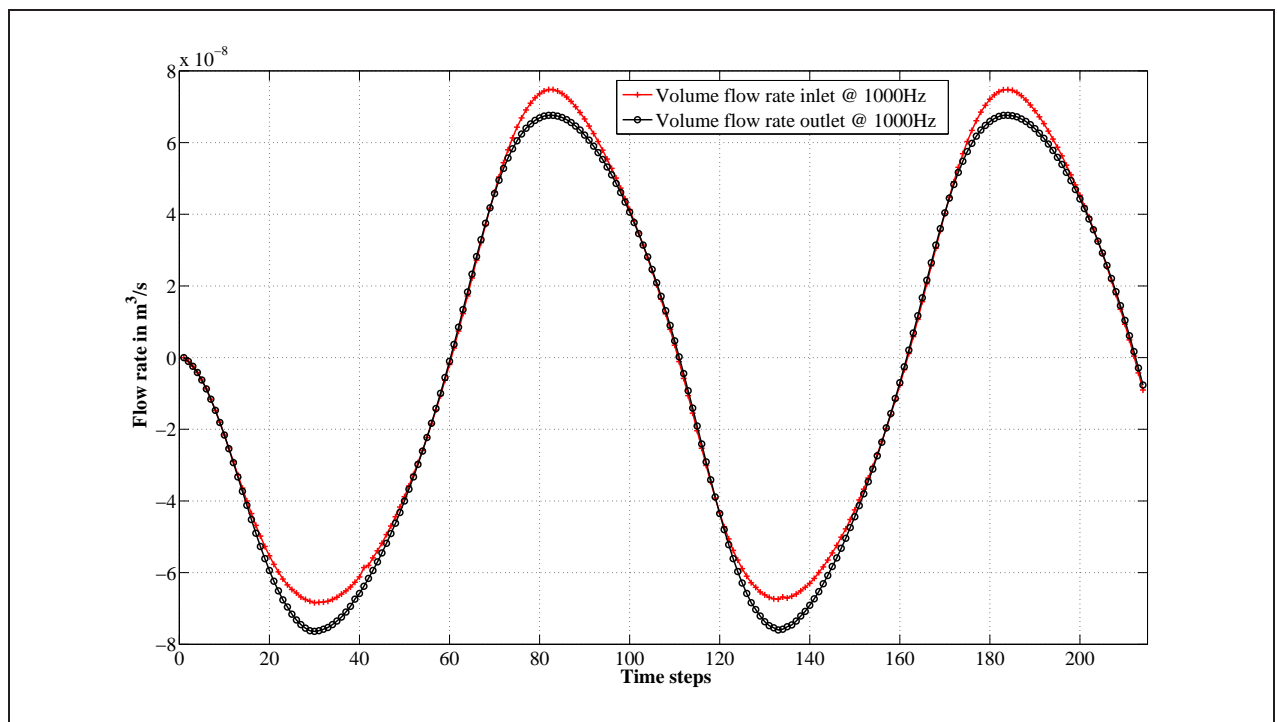


Figure 6.14: Inlet and outlet flow rates for the rounded diffuser inlet and sharp nozzle inlet configuration exited at 1kHz for 0.002 seconds and with $\Delta t = 0.01$ ms.

6.4.3 Round edged diffuser and sharpened edge nozzle configuration

This model has a rounded inlet edge, $r_t = 40 \mu\text{m}$, for diffuser flow and a sharpened inlet edge, angles approaching 180° , for the nozzle flow as depicted in Figure 6.8(c).

The resulting flows rates plotted for the 10 Hz, 100 Hz and 1000 Hz are plotted in Figures 6.15, 6.16 and 6.17 respectively. Flow rates are numerically integrated for the model de-

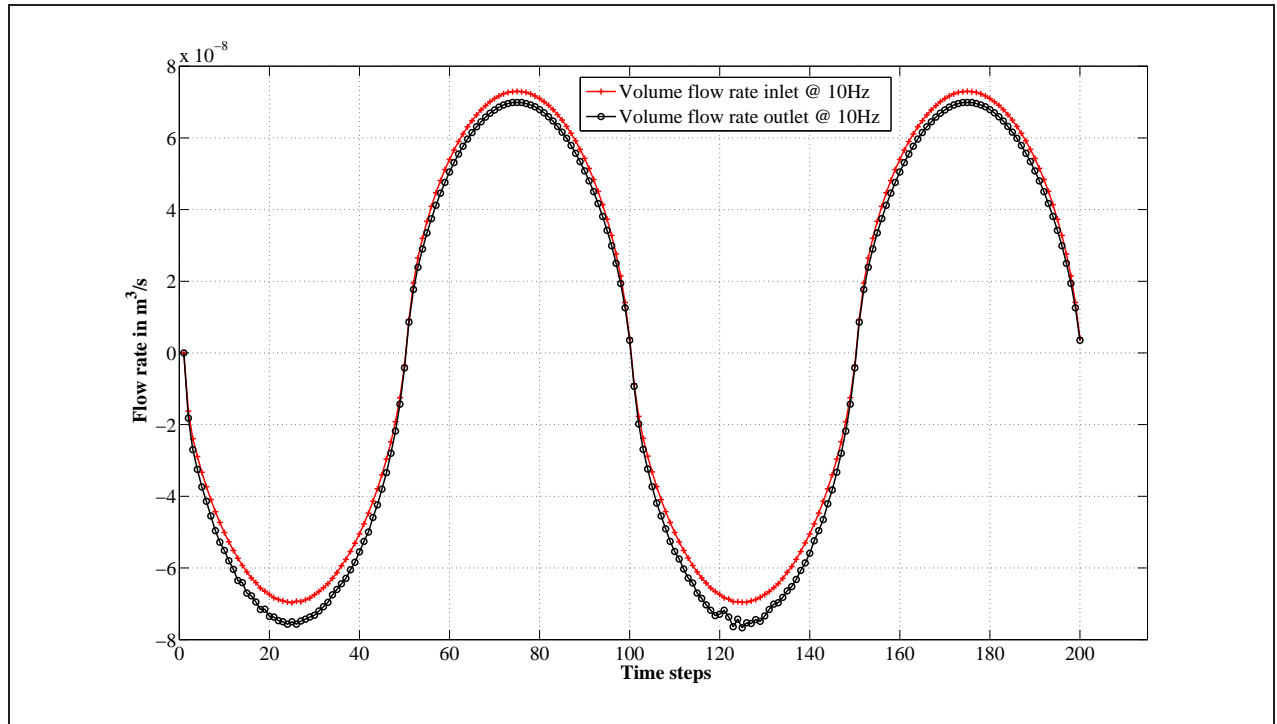


Figure 6.15: Inlet and outlet flow rates for the rounded diffuser inlet and sharpened nozzle inlet configuration exited at 10 Hz for 0.2 seconds and with $\Delta t = 1 \text{ ms}$.

picted in Figure 6.8(c) and given as

- 10 Hz = 10198 $\mu\text{L}/\text{min}$ - diffuser direction,
- 100 Hz = 10238 $\mu\text{L}/\text{min}$ - diffuser direction, and
- 1000 Hz = 11460 $\mu\text{L}/\text{min}$ - diffuser direction.

From Figures 6.15, 6.16 and 6.17 it is observed that there is a definite flow direction in the diffuser direction. As in the sharp edged model, a transient effect is also observed on the inlet flow curve, but much less prominent as in the sharp edged model's case, due to the diffuser rounding stabilizing the flow. The sharpened nozzle inlet edge appears to have added stability to the nozzle flow as the transient effects have decreased from the rounded diffuser inlet edge model. This effect can also be resolved by decreasing the time step. The result of the decreased time step is observed in Figure 6.17.

Pressure contour plots of this model follow in the Appendices.

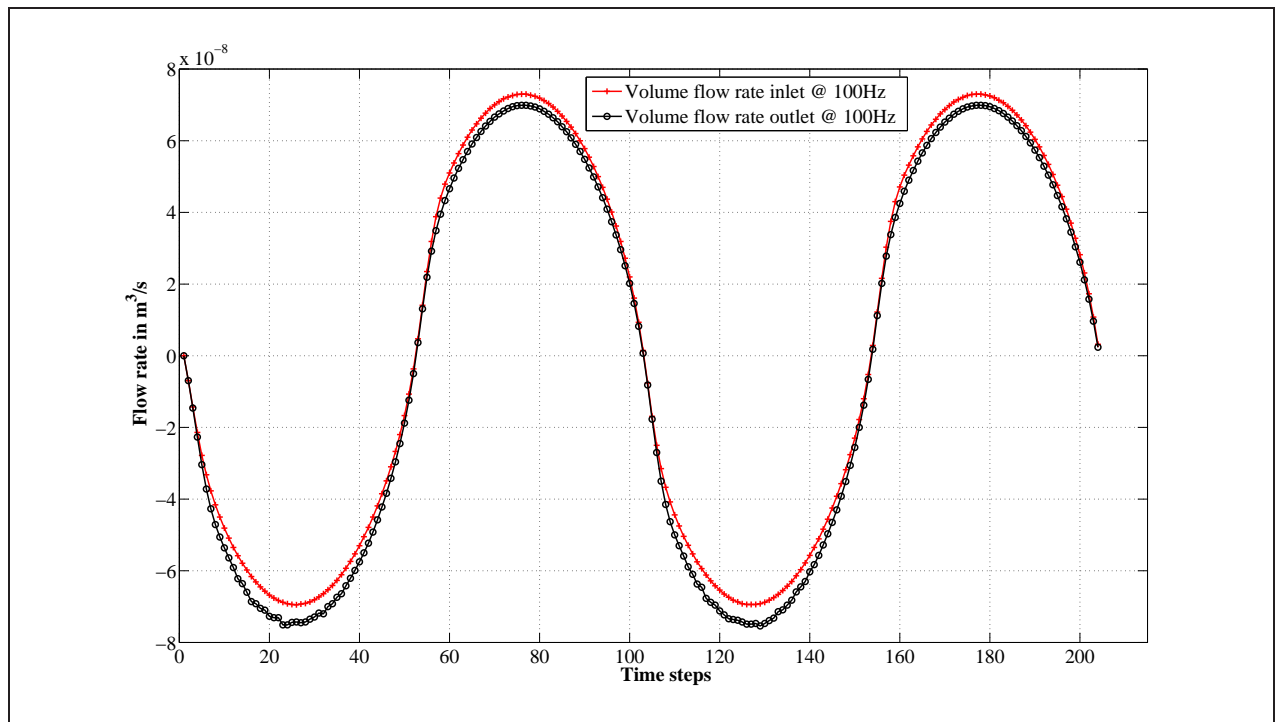


Figure 6.16: Inlet and outlet flow rates for the rounded diffuser inlet and sharpened nozzle inlet configuration exited at 100 Hz for 0.02 seconds and with $\Delta t = 0.1$ ms.

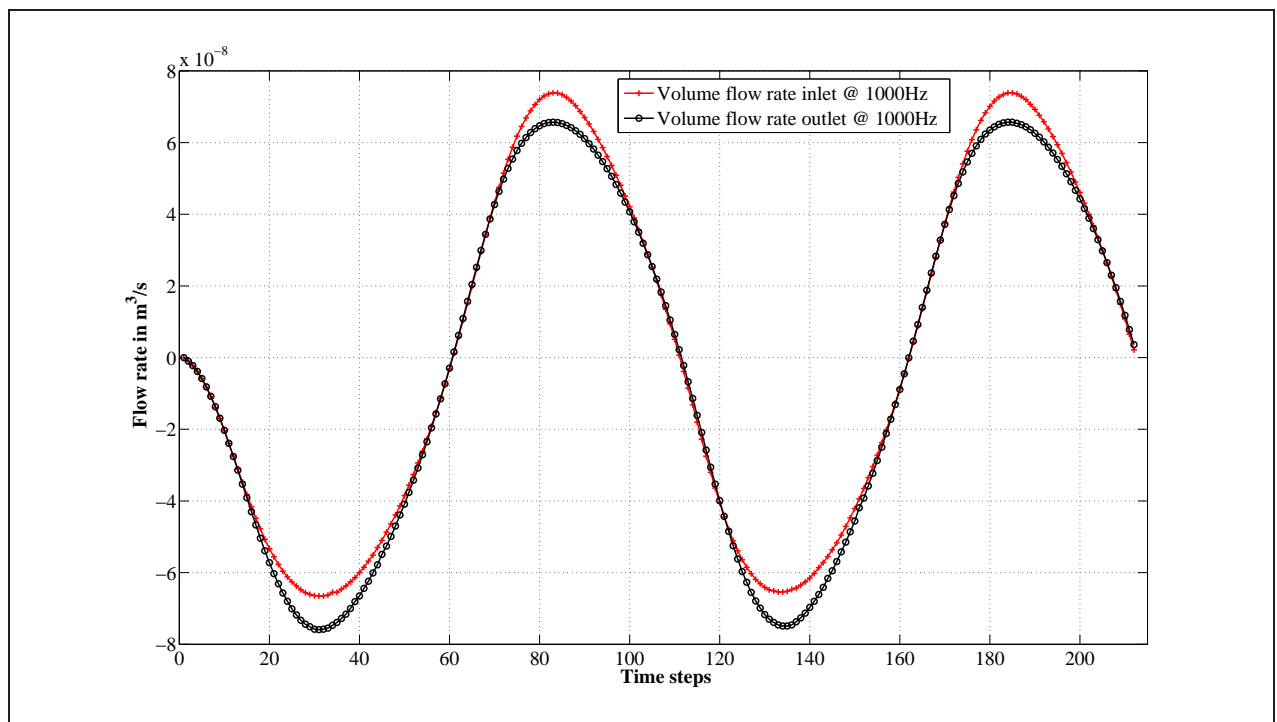


Figure 6.17: Inlet and outlet flow rates for the rounded diffuser inlet and sharpened nozzle inlet configuration exited at 1000 Hz for 0.002 seconds and with $\Delta t = 0.01$ ms.

Chapter 7

Results and discussion

Considering the data presented by Section 6, the nett flow rate \bar{Q} can be calculated as

$$\bar{Q} = \sum Q_{outlet} - \sum Q_{inlet} , \quad (7.0.1)$$

which means that if $\bar{Q} \leq 0$, the pump direction is in the diffuser direction. If however $\bar{Q} \geq 0$, the pump direction is in the nozzle direction.

The inlet and outlet data for all the configurations are integrated numerically and subtracted as in Equation (7.0.1). The flow losses in the diffuser are discussed according to Equation (5.4.11).

7.1 CFD solution

Analysing the three-dimensional transient results presented in Section 6, the combined absolute flow rates are depicted in Figure 7.1 and in Table 7.1. The maximum Reynolds number for all the three-dimensional simulations is found to be $Re \approx 950$. The Reynolds number varies between $0 < |Re| \leq 950$ for the simulations presented in Section 6.

This section also compares the data from the CFD simulations in Section 6 to the predicted velocity profiles from Jeffery-Hamel flow as illustrated by Section 5.4.1.

7.1.1 Transient simulation of sharp edged diffuser and nozzle inlet

From this simulation the effect of the sharp edged diffuser inlet is clear. The flow direction is reversed from what was expected. It is observed from Figures 6.9, 6.10 and 6.11, that the outlet curve is on average higher than the inlet curve. Considering Equation (7.0.1), this implies that the flow direction is in the nozzle direction.

The flow rate is reversed from what was expected. This result is verified by Olsson *et al* [26] with experimental studies under similar operating conditions and illustrates the high entrance losses associated with very low Reynolds number flows ($Re_{max} \approx 800$). Large relative velocity gradients around the diffuser inlet as depicted in Figure 7.2, contribute largely to the entrance losses. Even with large separation from the sidewalls, the inlet losses $K_{d,en}$ dominate the flow resistance at all simulated frequencies.

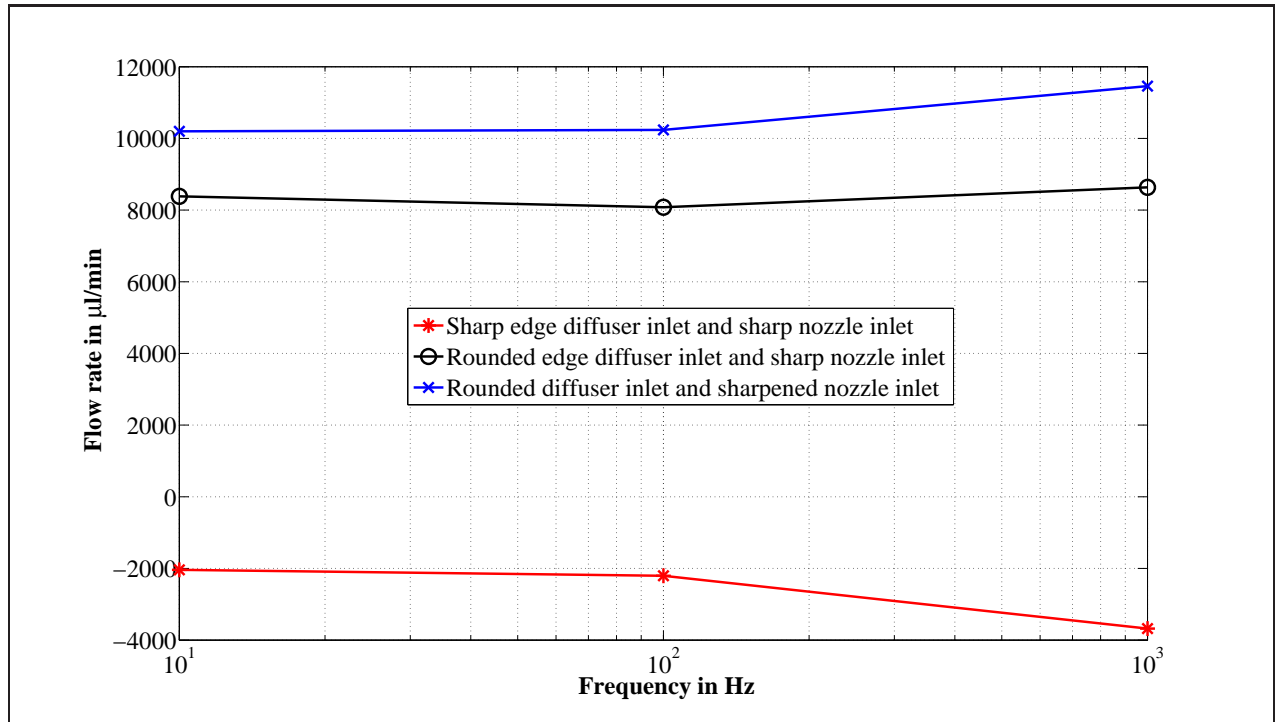


Figure 7.1: Flow rates for the three different diffuser / nozzle edge configurations vs frequency.

Table 7.1: Results of the three geometries as depicted in Figure 6.8 at three excitation frequencies.

Frequency (Hz)	(a) Sharp diffuser inlet	(b) Rounded diffuser inlet	(c) Rounded diffuser inlet and sharpened nozzle inlet
10	-2038 (µl/min)	8384 (µl/min)	10198 (µl/min)
100	-2206 (µl/min)	8080 (µl/min)	10238 (µl/min)
1000	-3679 (µl/min)	8635 (µl/min)	11460 (µl/min)

Data from five points throughout the length of the diffuser are recorded on three different depths as depicted by Figures 7.3 and 7.4. Velocity profiles are extracted from the data at these five locations and compared to the predicted Jeffery-Hamel velocity distribution as depicted in Figures 7.5, 7.6, 7.7, 7.8 and 7.9.

The velocity distribution from the CFD data also shows that the velocity profiles of the flow tends toward that of nozzle flow as illustrated by comparing Figure 5.10 to Figures 7.5, 7.6, 7.7 and 7.8. For this model (see Figure 6.8(a)) with a sharp diffuser inlet edge, only Figure 7.9 shows a reduced velocity gradient near the diffuser wall.

From Figures 7.5, 7.6, 7.7, 7.8 and 7.9 it is clear that the flow is never fully developed and large velocity gradients at the diffuser wall contribute to large shear forces as explained by Section 5.4. These large shear forces contribute to the already high flow resistance in the diffuser direction. It is also observed that there is negligible back flow in the diffuser and there is very little comparison to the Jeffery-Hamel velocity distribution.

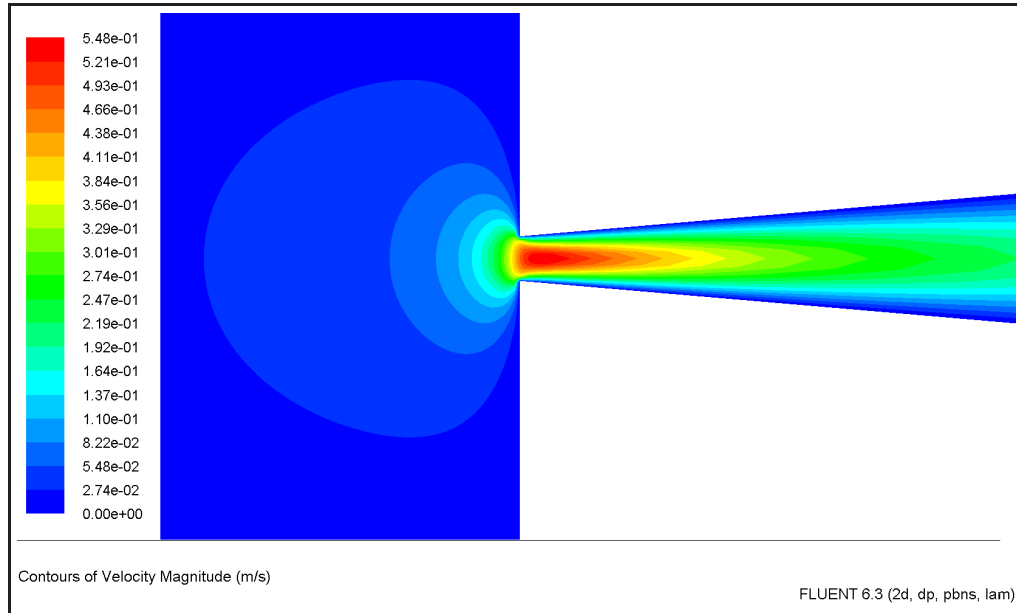


Figure 7.2: A two dimensional view of the velocity gradients around the diffuser inlet.

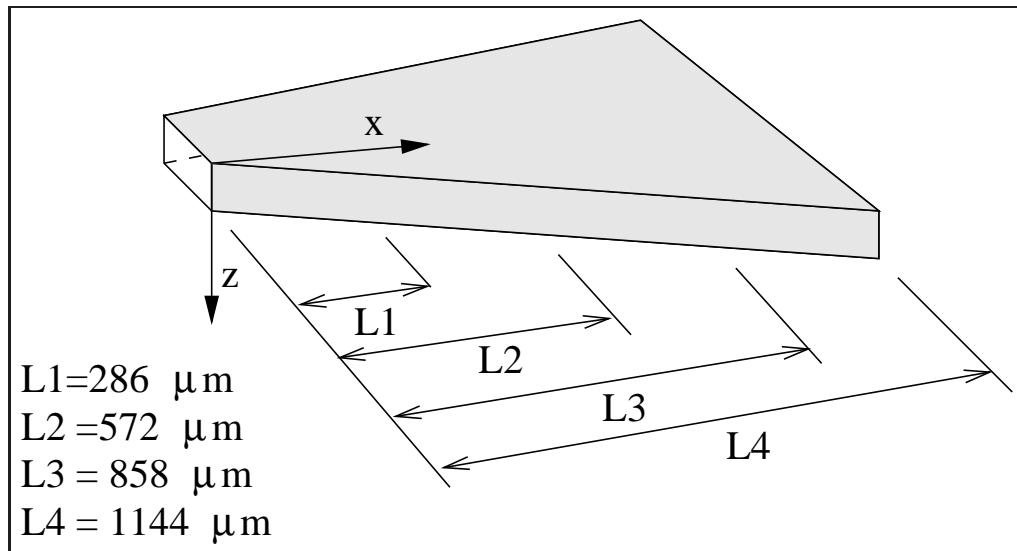


Figure 7.3: An illustration of the diffuser lengths where data were recorded.

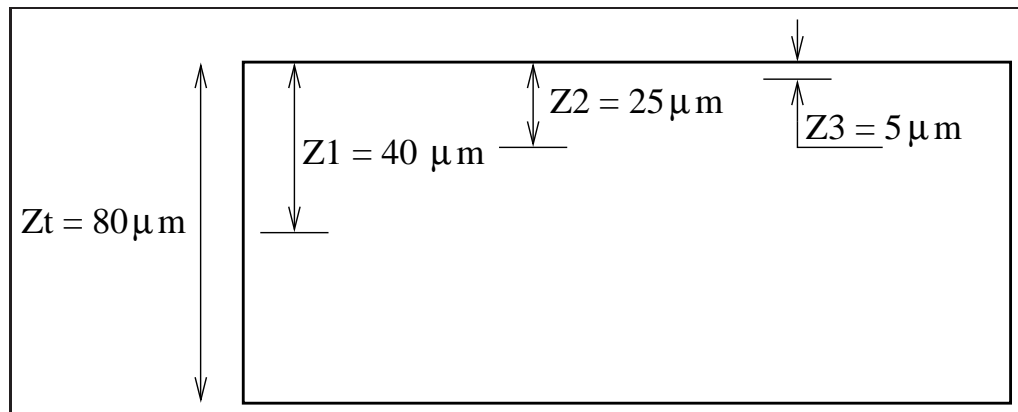


Figure 7.4: A cross section of the diffuser showing the depths where data were recorded.

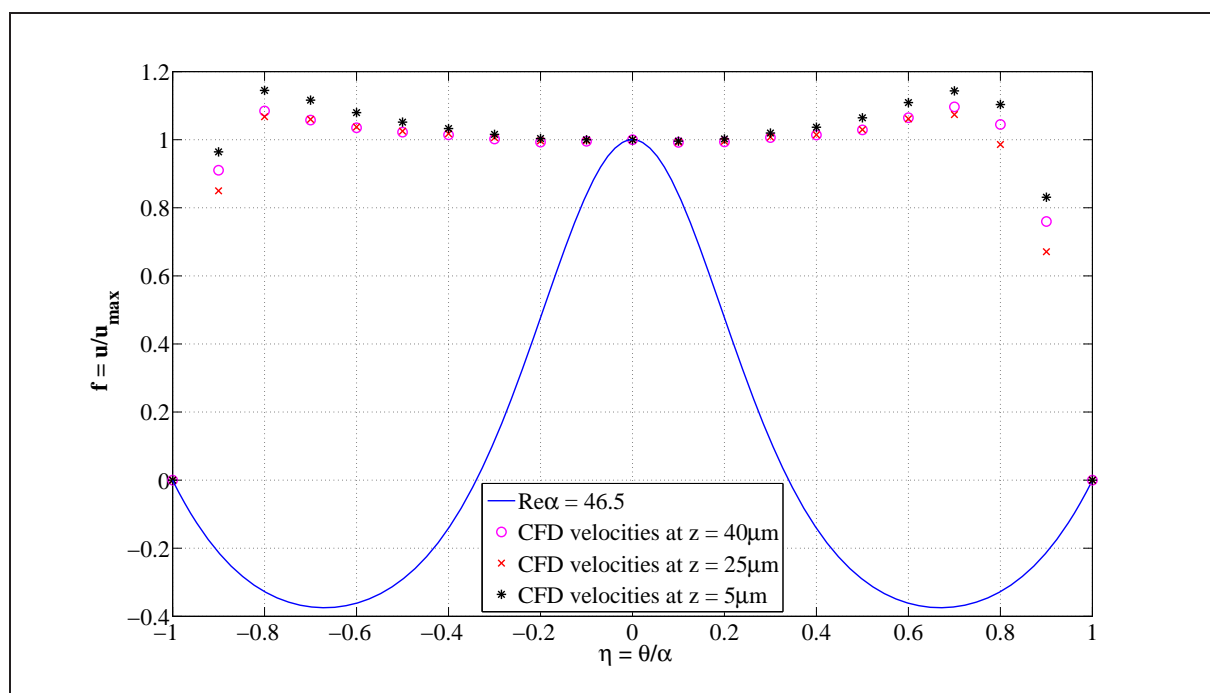


Figure 7.5: A comparison between the predicted Jeffery-Hamel velocity profiles and the calculated CFD velocity vectors for $x = 0 \mu\text{m}$, $t = 1.20 \text{ ms}$, @ 1 kHz and at three depths in the diffuser for the sharp edged model (see Figure 6.8(a)).

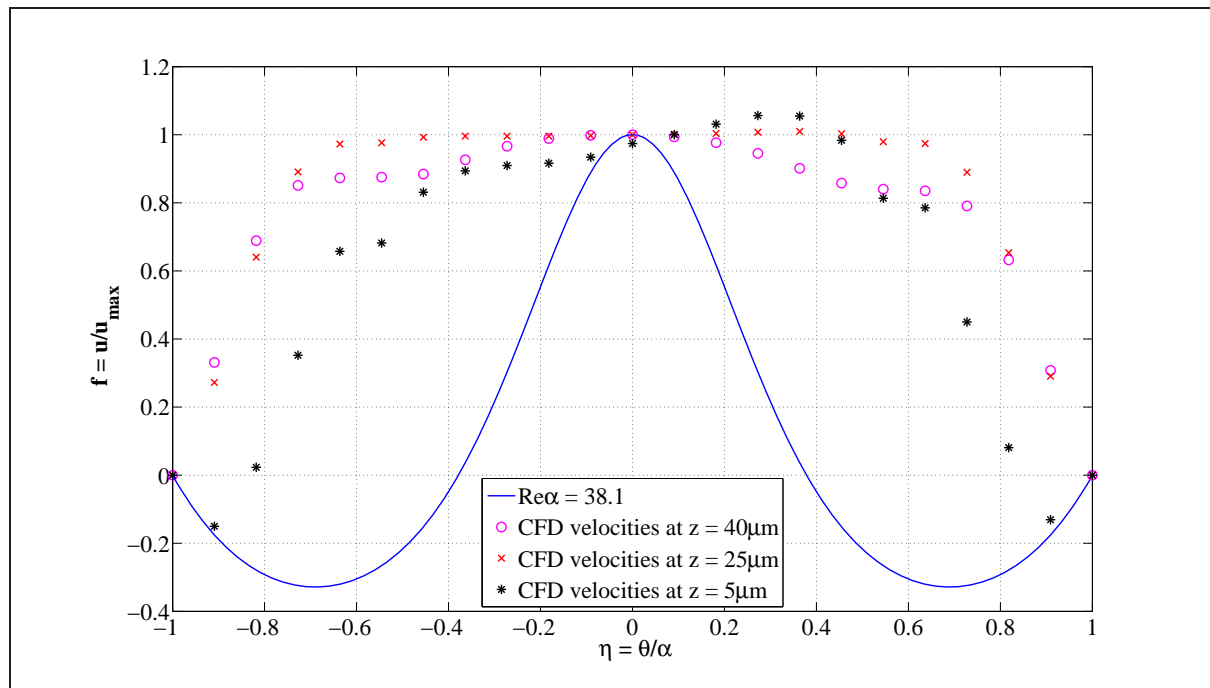


Figure 7.6: A comparison between the predicted Jeffery-Hamel velocity profiles and the calculated CFD velocity vectors for $x = 286 \mu\text{m}$, $t = 1.20 \text{ ms}$, @ 1 kHz and at three depths in the diffuser for the sharp edged model (see Figure 6.8(a)).

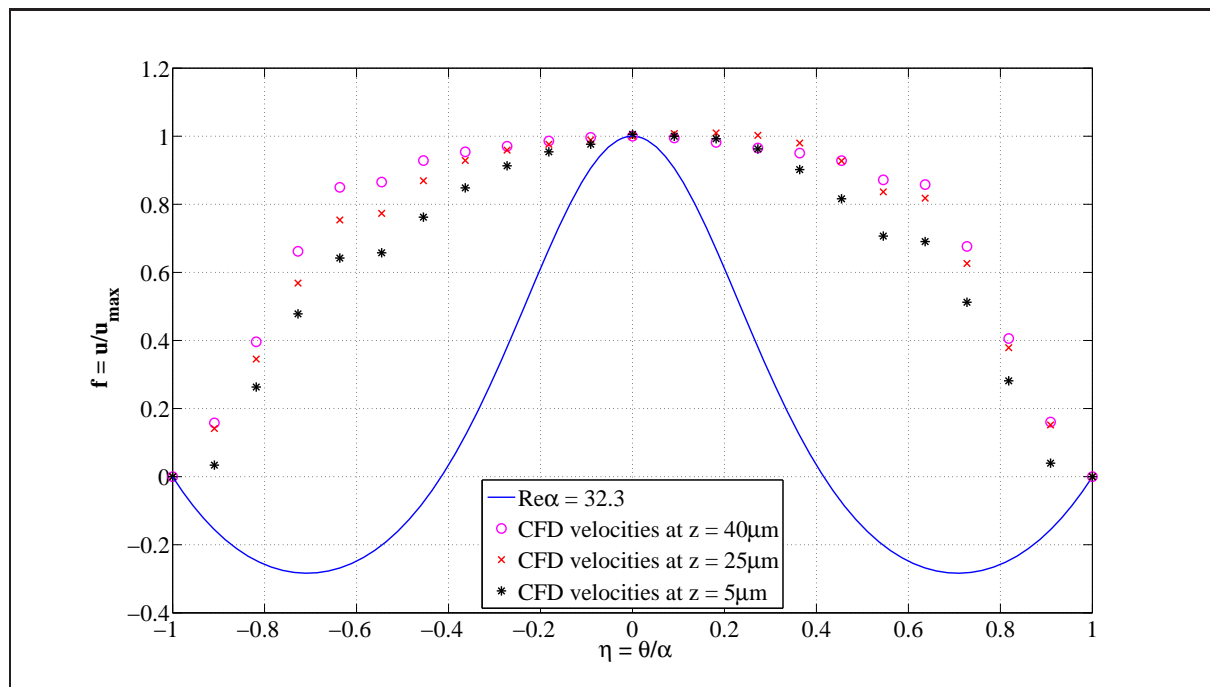


Figure 7.7: A comparison between the predicted Jeffery-Hamel velocity profiles and the calculated CFD velocity vectors for $x = 572 \mu\text{m}$, $t = 1.20 \text{ ms}$, @ 1 kHz and at three depths in the diffuser for the sharp edged model (see Figure 6.8(a)).

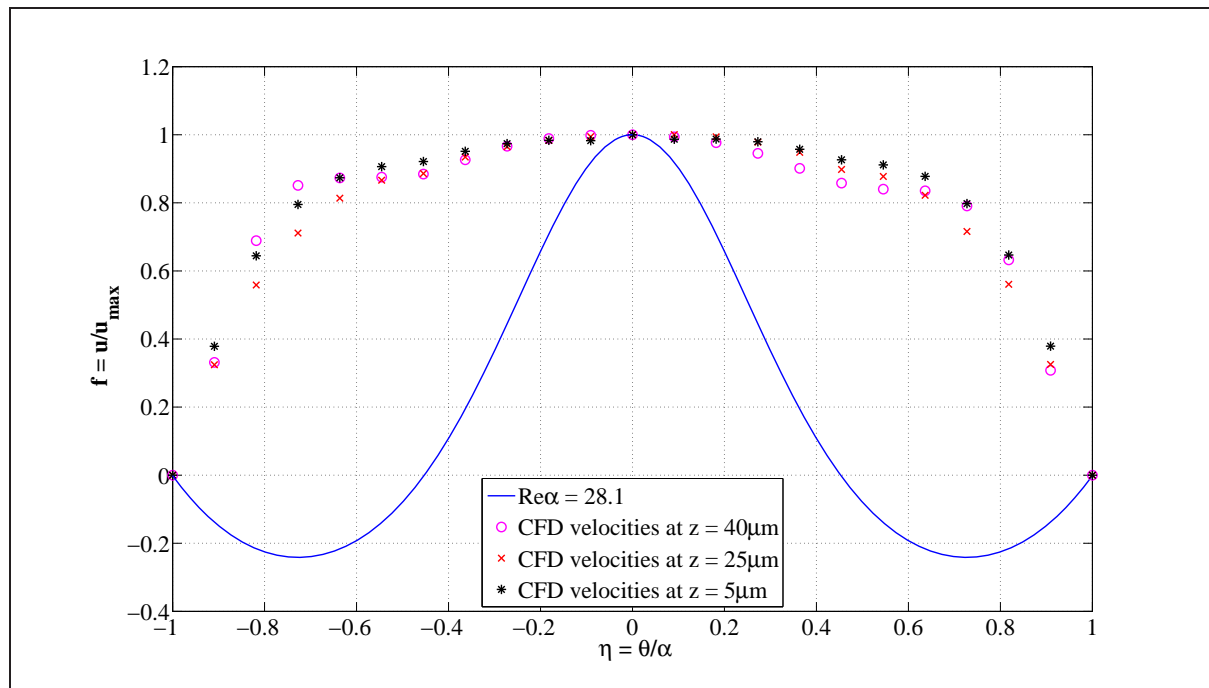


Figure 7.8: A comparison between the predicted Jeffery-Hamel velocity profiles and the calculated CFD velocity vectors for $x = 858 \mu\text{m}$, $t = 1.20 \text{ ms}$, @ 1 kHz and at three depths in the diffuser for the sharp edged model (see Figure 6.8(a)).

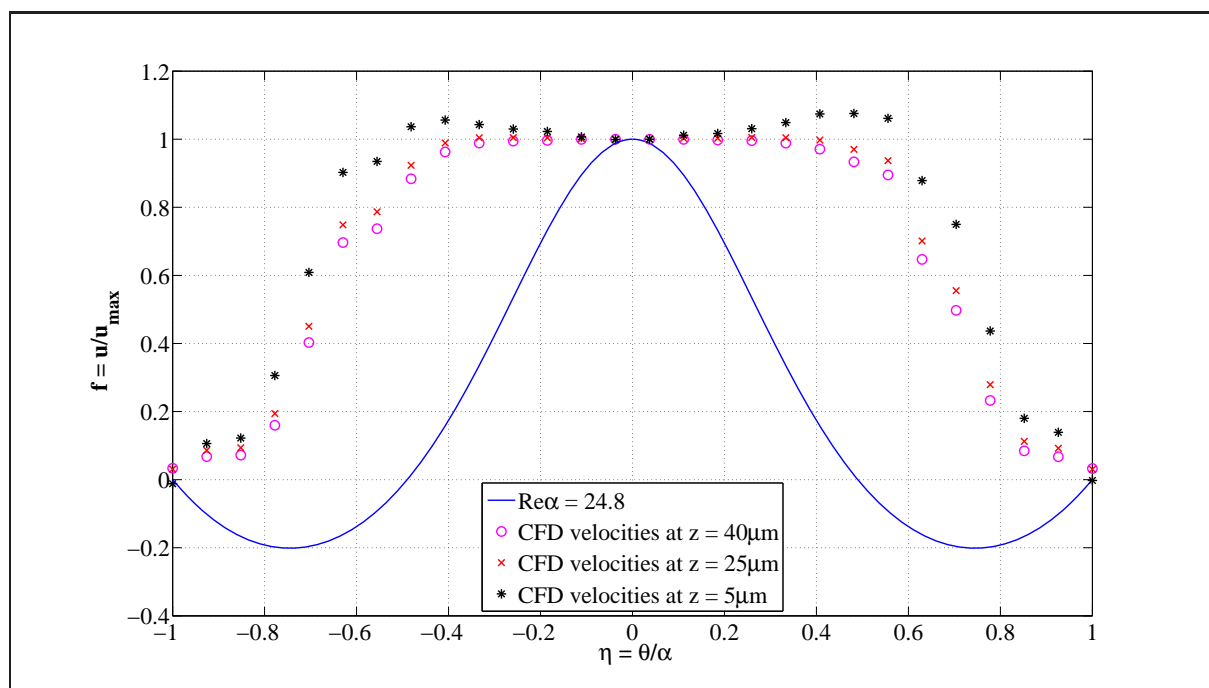


Figure 7.9: A comparison between the predicted Jeffery-Hamel velocity profiles and the calculated CFD velocity vectors for $x = 1144 \mu\text{m}$, $t = 1.20 \text{ ms}$, @ 1 kHz and at three depths in the diffuser for the sharp edged model (see Figure 6.8(a)).

7.1.2 Transient simulation of rounded diffuser inlet edge model

From the results depicted in Figures 6.12, 6.13 and 6.14 it is observed that the diffuser functions as intended. Studying the results show that the inlet curve is on average higher than the outlet curve. When considering Equation (7.0.1) this implicates that the flow direction is in the diffuser direction.

The rounded inlet for the diffuser illustrates the effect of the entrance losses at low Reynolds numbers. Compared to the sharp diffuser inlet model the flow rate is improved by more than 100% on the absolute flow rate. The flow in this model is in the diffuser direction opposed to the nozzle direction as is the case in the sharp edge model. The flow patterns from Figures 7.10, 7.11, 7.12, 7.13 and 7.14 also appear to be more steady compared to that of the sharp diffuser inlet model. The maximum Reynolds number is $Re_{max} \approx 960$.

Data from five points throughout the length of the diffuser are recorded on three different depths as depicted by Figures 7.3 and 7.4. Velocity profiles are extracted from the data at these five locations and compared to the predicted Jeffery-Hamel velocity distribution as depicted by Figures 7.10, 7.11, 7.12, 7.13 and 7.14.

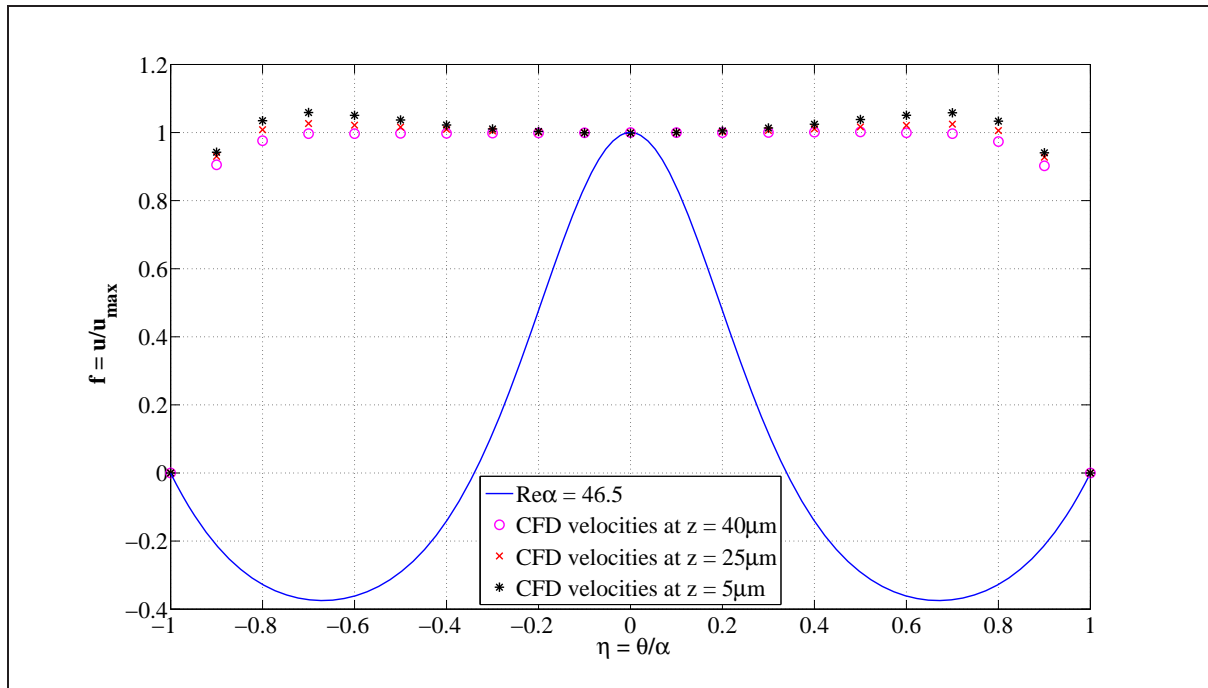


Figure 7.10: A comparison between the predicted Jeffery-Hamel velocity profiles and the calculated CFD velocity vectors for $x = 0 \mu\text{m}$, $t = 1.20 \text{ ms}$, @ 1 kHz and at three depths in the diffuser for the rounded diffuser inlet edge model (see Figure 6.8(b)).

From Figures 7.10, 7.11, 7.12, 7.13 and 7.14 it is observed that the flow is on average closer to what was predicted by the Jeffery-Hamel velocity distributions than that of the sharp inlet model. The Jeffery-Hamel model assumes that flow is fully developed at the entrance and it is this characteristic that attributes to the major differences in the CFD data and Jeffery-Hamel flow at $x = 0 \mu\text{m}$, $286 \mu\text{m}$, $572 \mu\text{m}$. As the flow develops along the length of the diffuser ($x = 858$

μm , $1144 \mu\text{m}$), the differences between the CFD data and Jeffery-Hamel flow is decreased and back flow is observed near the diffuser wall at all depths ($z = 5 \mu\text{m}$, $25 \mu\text{m}$, $40 \mu\text{m}$) as depicted by Figures 7.13 and 7.14.

Comparing CFD data from this model (see Figure 6.8(b)) to data from the sharp diffuser inlet edge model (see Figure 6.8(a)) it is observed that the velocity profiles from this model appear to be less irregular than those of the latter.

The velocity distribution from the CFD data also shows that the velocity gradients become normal to the wall of the diffuser at $x = 286 \mu\text{m}$ as depicted in Figure 7.11. When the velocity gradient is normal to the wall of the diffuser the shear stress at the wall $\tau(y) = \mu(\partial v/\partial x)$ is diminished, thus lowering the flow resistance of the flow in the diffuser direction.

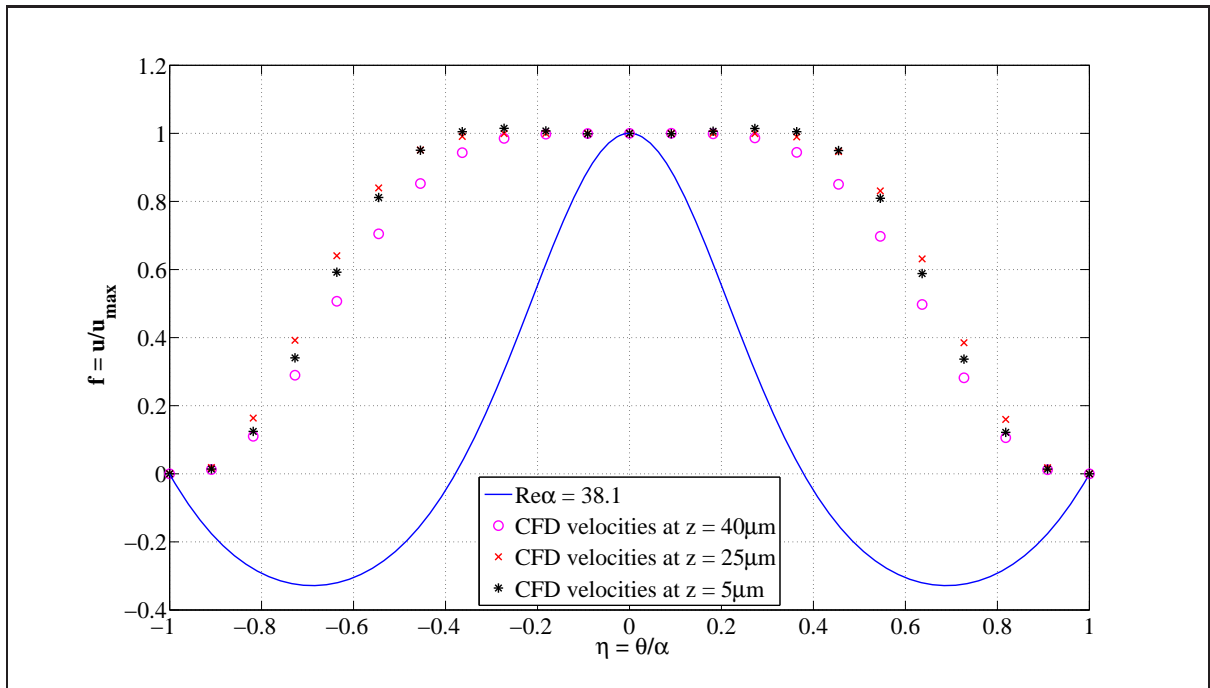


Figure 7.11: A comparison between the predicted Jeffery-Hamel velocity profiles and the calculated CFD velocity vectors for $x = 286 \mu\text{m}$, $t = 1.20 \text{ ms}$, @ 1 kHz and at three depths in the diffuser for the rounded diffuser inlet edge model (see Figure 6.8(b)).

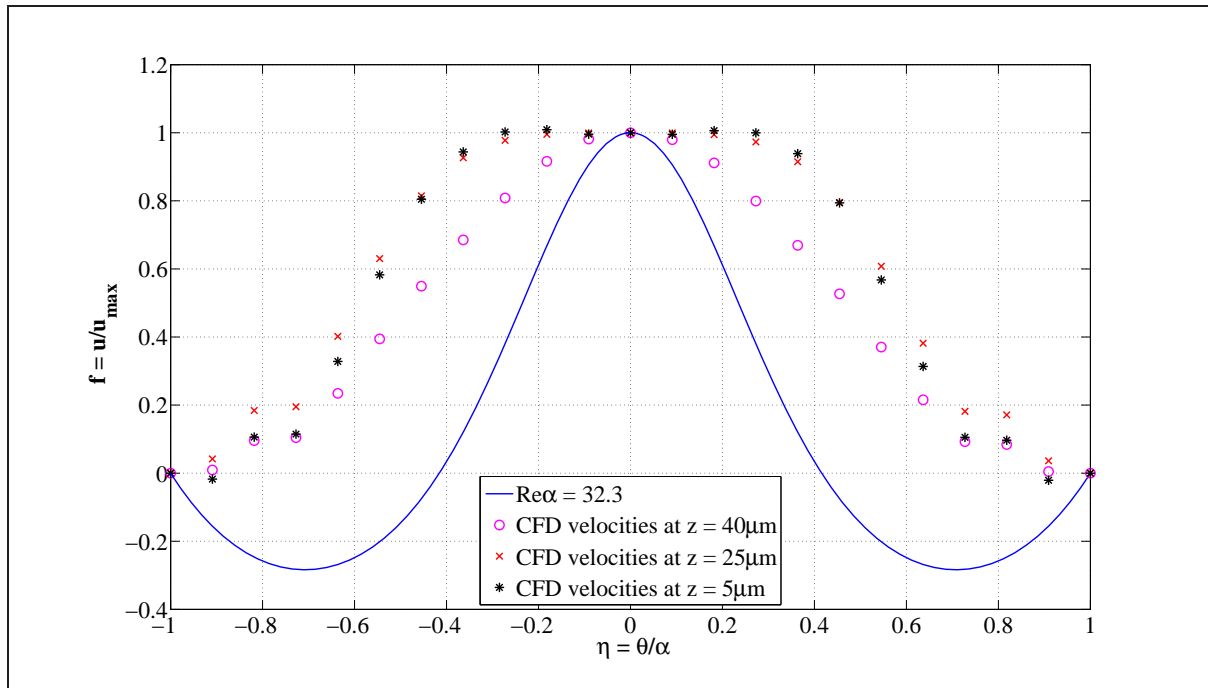


Figure 7.12: A comparison between the predicted Jeffery-Hamel velocity profiles and the calculated CFD velocity vectors for $x = 572 \mu\text{m}$, $t = 1.20 \text{ ms}$, @ 1 kHz and at three depths in the diffuser for the rounded diffuser inlet edge model (see Figure 6.8(b)).

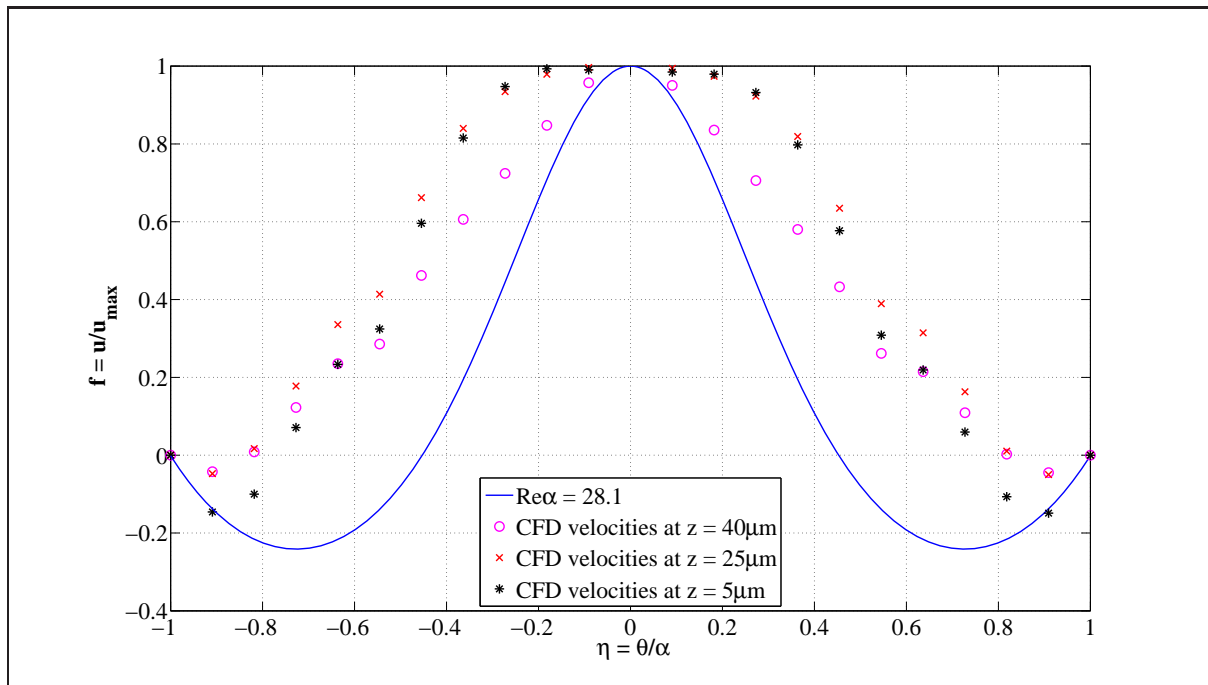


Figure 7.13: A comparison between the predicted Jeffery-Hamel velocity profiles and the calculated CFD velocity vectors for $x = 858 \mu\text{m}$, $t = 1.20 \text{ ms}$, @ 1 kHz and at three depths in the diffuser for the rounded diffuser inlet edge model (see Figure 6.8(b)).

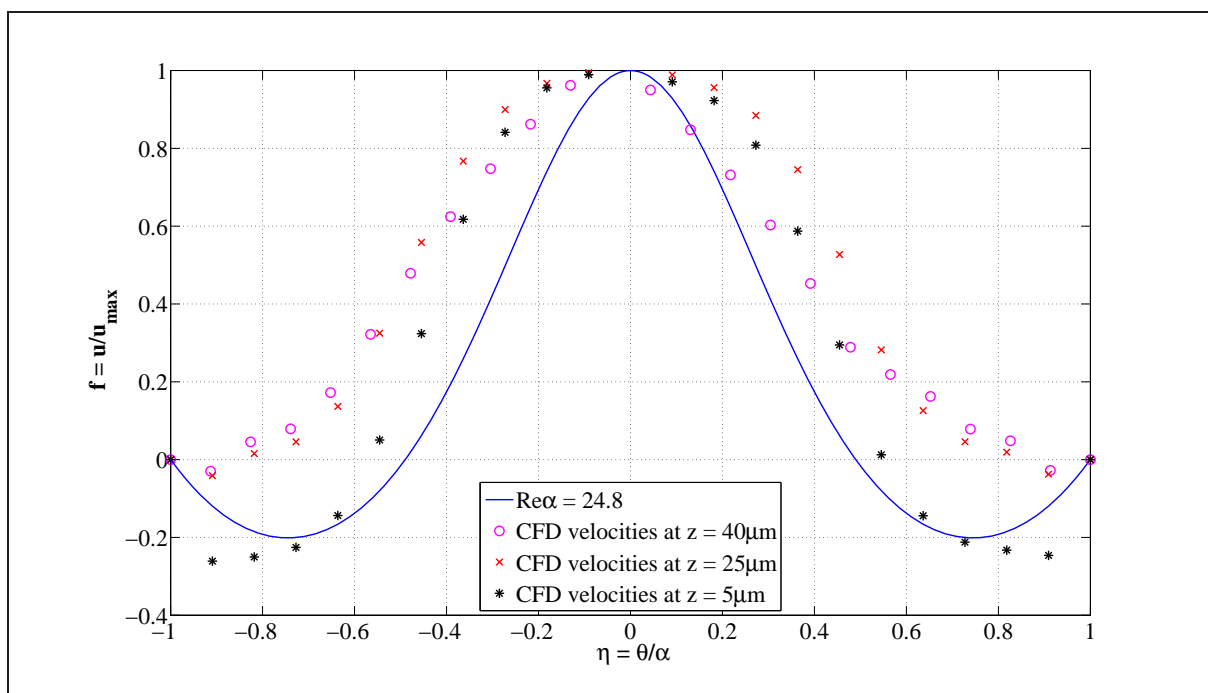


Figure 7.14: A comparison between the predicted Jeffery-Hamel velocity profiles and the calculated CFD velocity vectors for $x = 1144 \mu\text{m}$, $t = 1.20 \text{ ms}$, @ 1 kHz and at three depths in the diffuser for the rounded diffuser inlet edge model (see Figure 6.8(b)).

7.1.3 Transient simulation of rounded diffuser inlet edge and sharpened nozzle inlet edge

From the results depicted in Figures 6.15, 6.16 and 6.17 it is observed that the diffuser functions as intended. Studying the results show that the inlet curve is on average higher than the outlet curve. When considering Equation (7.0.1) this implicates that the flow direction is in the diffuser direction.

The sharpened outlet for the diffuser illustrates the effect of the entrance losses at low Reynolds numbers. Compared to the round diffuser inlet model the flow rate is improved by more than 30%. The inlet flow rate curve is also more steady compared to the other two models as depicted by Figures 6.15, 6.16 and 6.17. This simulation illustrate the effect of entrance losses in the nozzle direction. Considering Figures 7.15, 7.16, 7.17, 7.18 and 7.19 the flow patterns appear to be even more steady compared to that of the rounded diffuser inlet model and the sharp edge model (see Figures 6.8(b) and (a) respectively). The maximum Reynolds number is $Re_{max} \approx 990$.

As in the previous models, data from five points throughout the length of the diffuser are recorded on three different depths as depicted by Figures 7.3 and 7.4. Velocity profiles are extracted from the data at these five locations and compared to the predicted Jeffery-Hamel velocity distribution as depicted by Figures 7.15, 7.16, 7.17, 7.18 and 7.19.

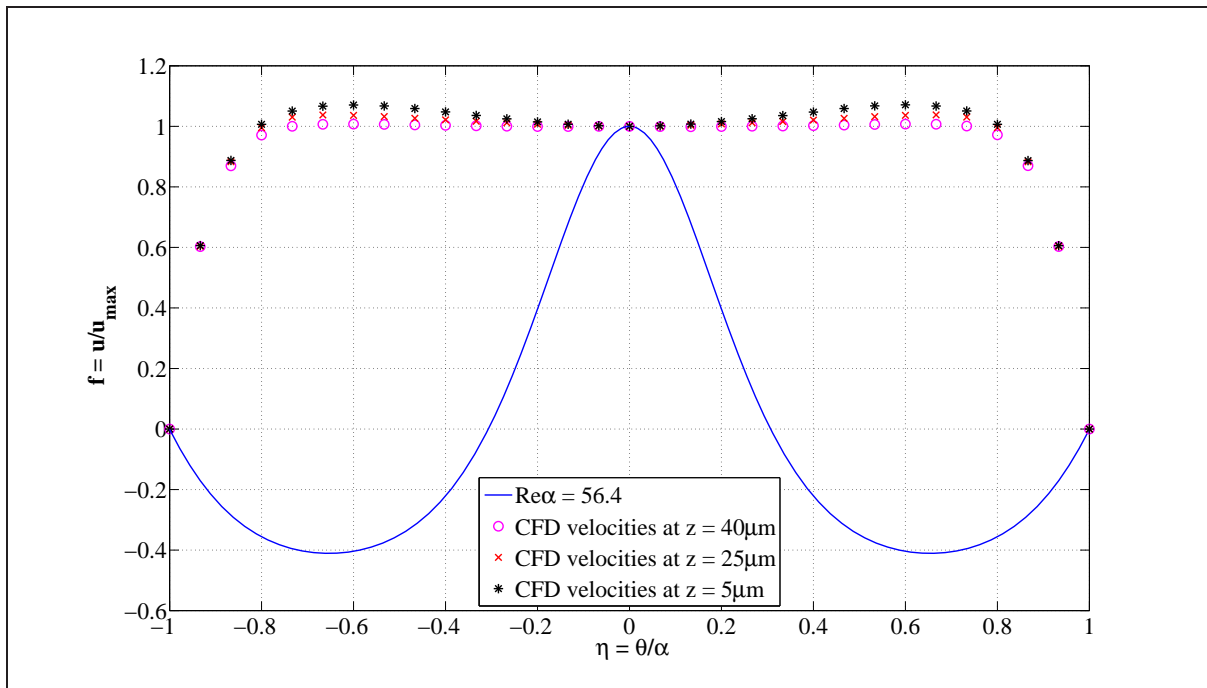


Figure 7.15: A comparison between the predicted Jeffery-Hamel velocity profiles and the calculated CFD velocity vectors for $x = 0 \mu\text{m}$, $t = 1.20 \text{ ms}$, @ 1 kHz and at three depths in the diffuser for the rounded diffuser inlet edge and sharpened nozzle inlet edge model (see Figure 6.8(c)).

From Figures 7.15, 7.16, 7.17, 7.18 and 7.19 it is observed that the flow is similar to the flow in the rounded diffuser inlet edge model (see Figure 6.8(b)). As in the previous model the Jeffery-Hamel model assumes that flow is fully developed at the entrance and it is this characteristic

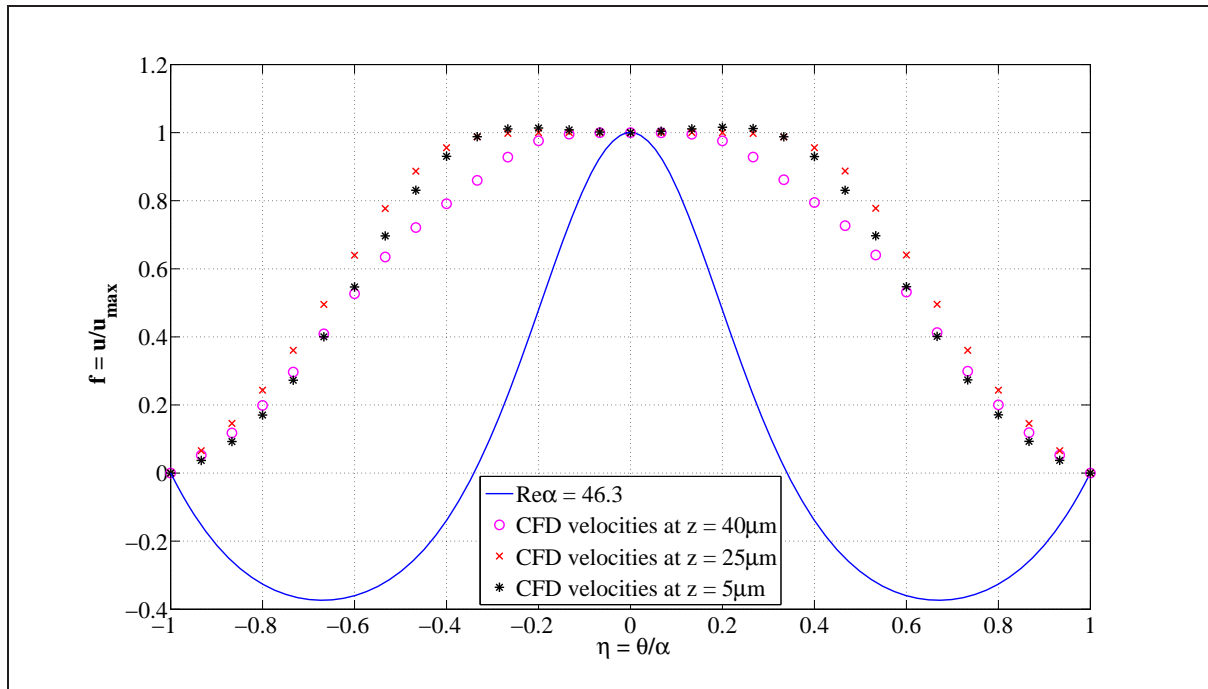


Figure 7.16: A comparison between the predicted Jeffery-Hamel velocity profiles and the calculated CFD velocity vectors for $x = 286 \mu\text{m}$, $t = 1.20 \text{ ms}$, @ 1 kHz and at three depths in the diffuser for the rounded diffuser inlet edge and sharpened nozzle inlet edge model (see Figure 6.8(c)).

that attributes to the major differences in the CFD data and Jeffery-Hamel flow at $x = 0 \mu\text{m}$, $286 \mu\text{m}$, $572 \mu\text{m}$. As the flow develops along the length of the diffuser ($x = 858 \mu\text{m}$, $1144 \mu\text{m}$), the differences between the CFD data and Jeffery-Hamel flow is decreased and back flow is observed near the diffuser wall as depicted by Figures 7.18, 7.19.

Examining the velocity profiles as depicted by Figures 7.16, 7.17 and 7.18 reveals a “kink” in the data at $z = 40 \mu\text{m}$ and $\eta \approx \pm 0.3$. Back flow at $z = 40 \mu\text{m}$, $25 \mu\text{m}$ is not as prominent as at $z = 5 \mu\text{m}$. The velocity distribution from the CFD data also shows that the velocity gradients become normal to the wall of the diffuser at $x = 572 \mu\text{m}$ as depicted in Figure 7.16. When the velocity gradient is normal to the wall of the diffuser the shear stress at the wall $\tau(y) = \mu(\partial v / \partial x)$ is diminished, thus lowering the flow resistance of the flow in the diffuser direction.

Since this model’s diffuser flow (see Figure 6.8(c)) is similar to that of the rounded diffuser inlet model (see Figure 6.8(b)) the difference in flow rate can be attributed to the nozzle direction flow.

From Figure 7.20 its observed that the velocity profile from the sharpened inlet edge model follows the Jeffery-Hamel prediction more closely than the model with the sharp inlet edge. Although the velocity gradient of the sharp edged nozzle inlet model is greater than that of the sharpened inlet edge model as depicted by Figures 7.21 and 7.22 the latter demonstrated superior flow directing capabilities. This can be explained by increased entrance losses caused by high velocity gradients around the entrance of the nozzles as depicted by Figures 7.23 and 7.24.

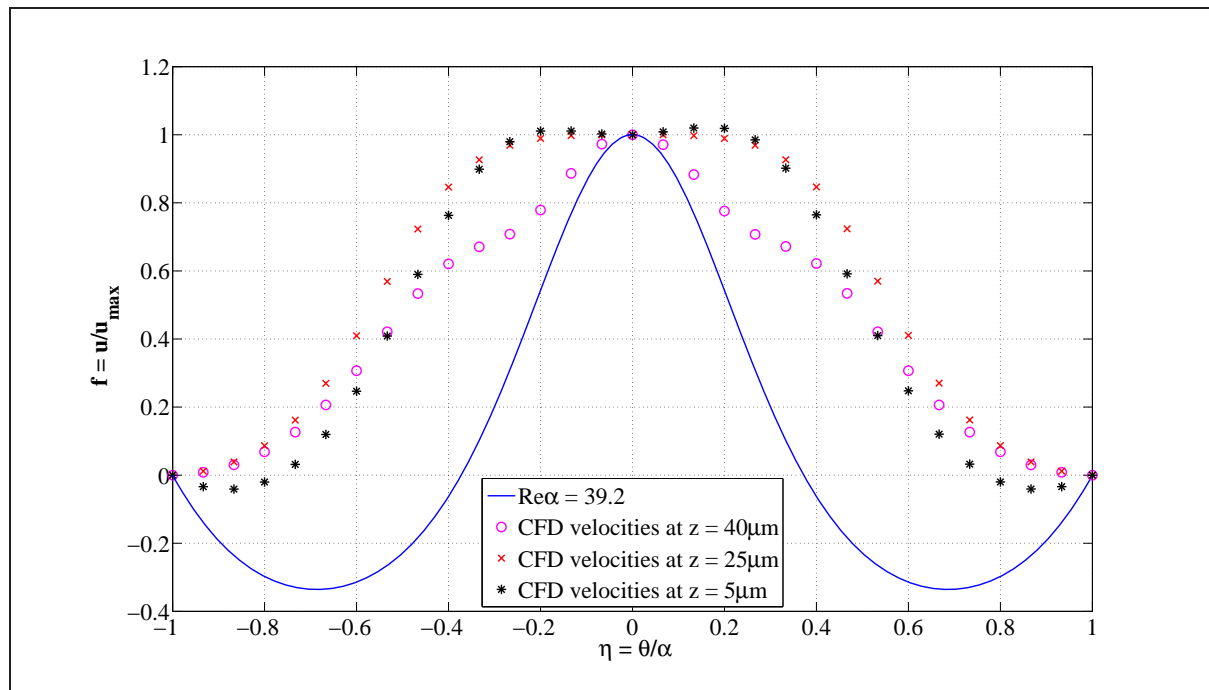


Figure 7.17: A comparison between the predicted Jeffery-Hamel velocity profiles and the calculated CFD velocity vectors for $x = 572 \mu\text{m}$, $t = 1.20 \text{ ms}$, @ 1 kHz and at three depths in the diffuser for the rounded diffuser inlet edge and sharpened nozzle inlet edge model (see Figure 6.8(c)).

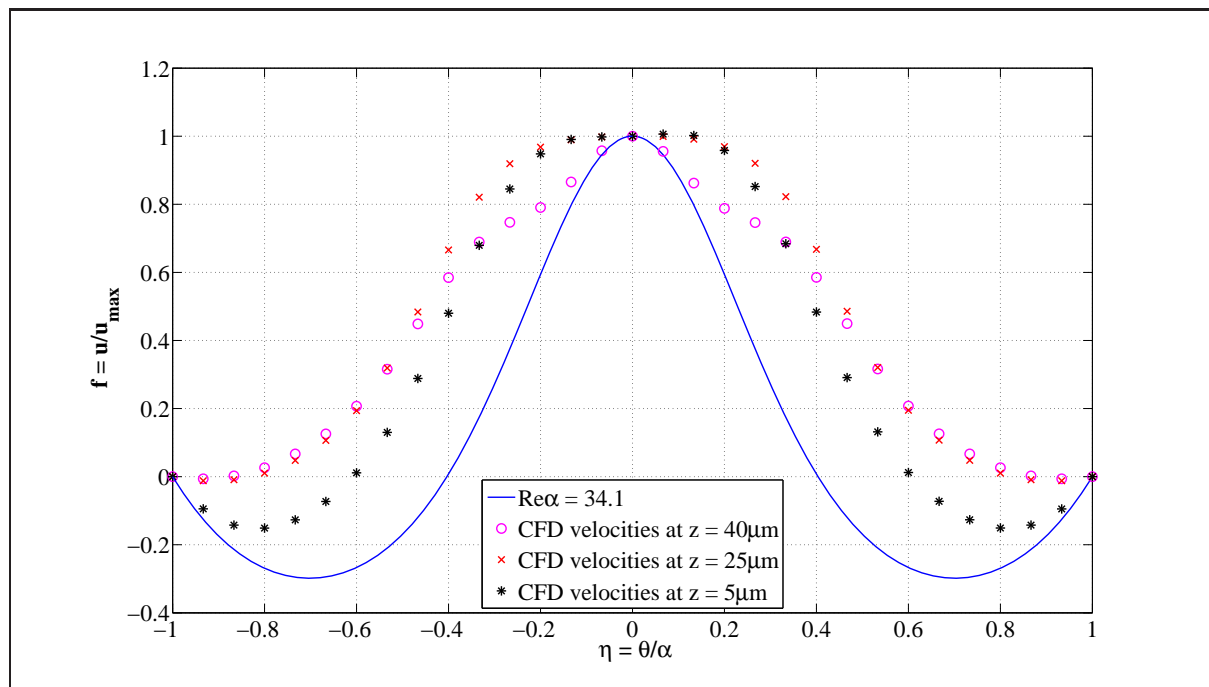


Figure 7.18: A comparison between the predicted Jeffery-Hamel velocity profiles and the calculated CFD velocity vectors for $x = 858 \mu\text{m}$, $t = 1.20 \text{ ms}$, @ 1 kHz and at three depths in the diffuser for the rounded diffuser inlet edge and sharpened nozzle inlet edge model (see Figure 6.8(c)).

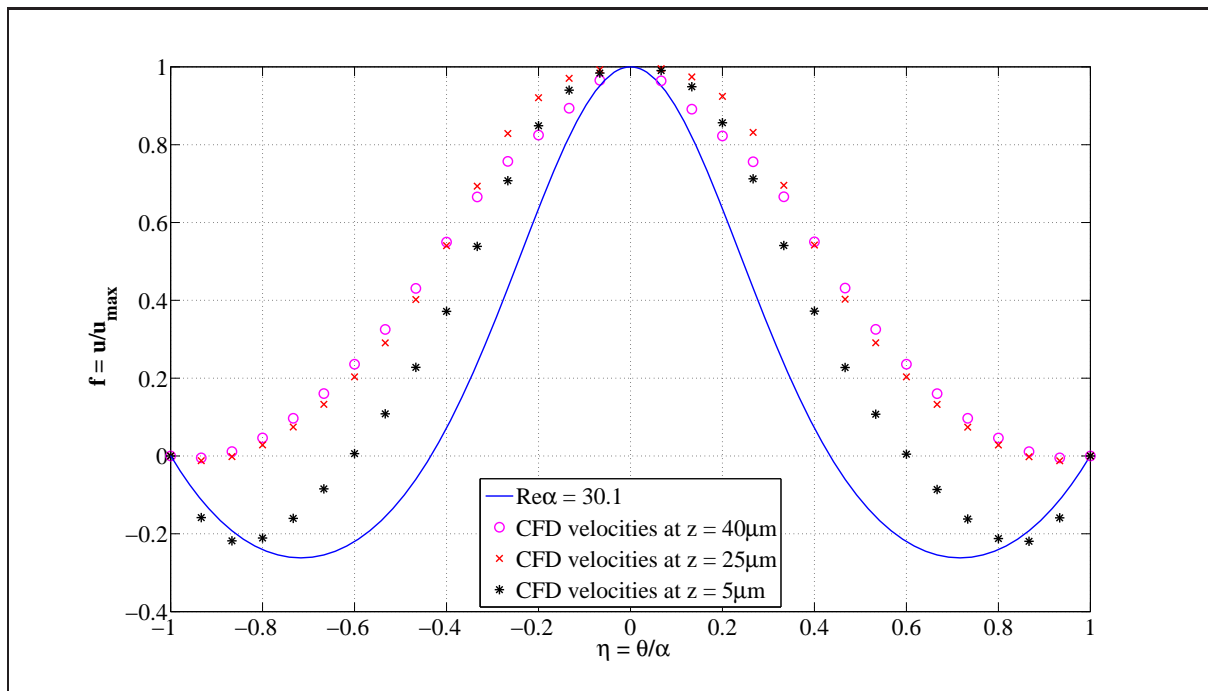


Figure 7.19: A comparison between the predicted Jeffery-Hamel velocity profiles and the calculated CFD velocity vectors for $x = 1144 \mu\text{m}$, $t = 1.20 \text{ ms}$, @ 1 kHz and at three depths in the diffuser for the rounded diffuser inlet edge and sharpened nozzle inlet edge model (see Figure 6.8(c)).

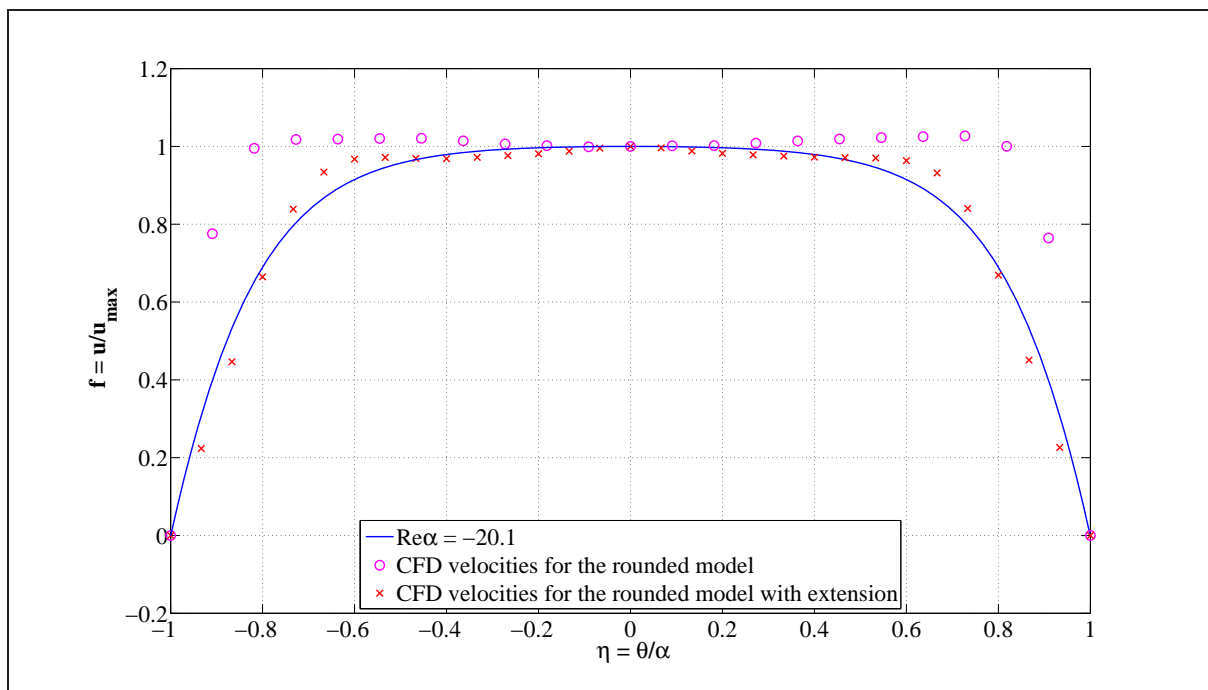


Figure 7.20: A comparison between the predicted Jeffery-Hamel velocity profiles and the calculated CFD velocity vectors for nozzle flow in the rounded diffuser inlet model and the rounded diffuser inlet model with extension at the nozzle entrance.

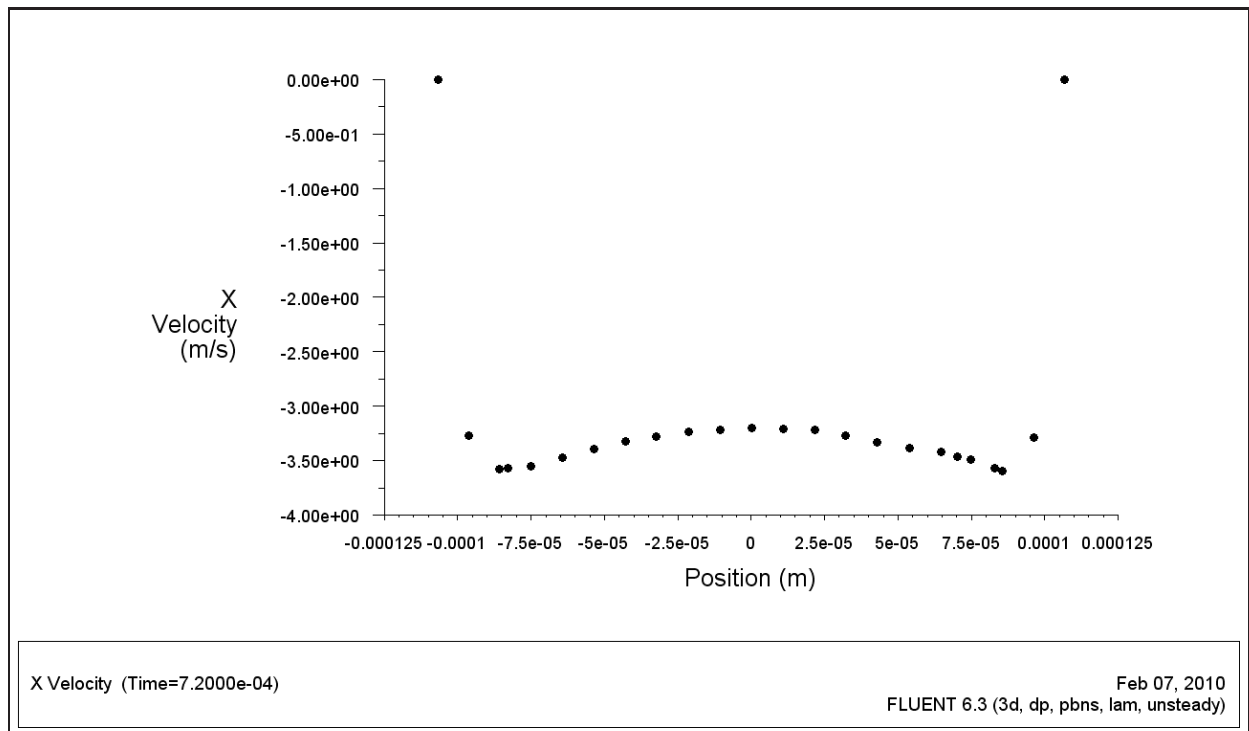


Figure 7.21: Velocity profile plot of nozzle flow in the sharp nozzle inlet edge model near the nozzle entrance.

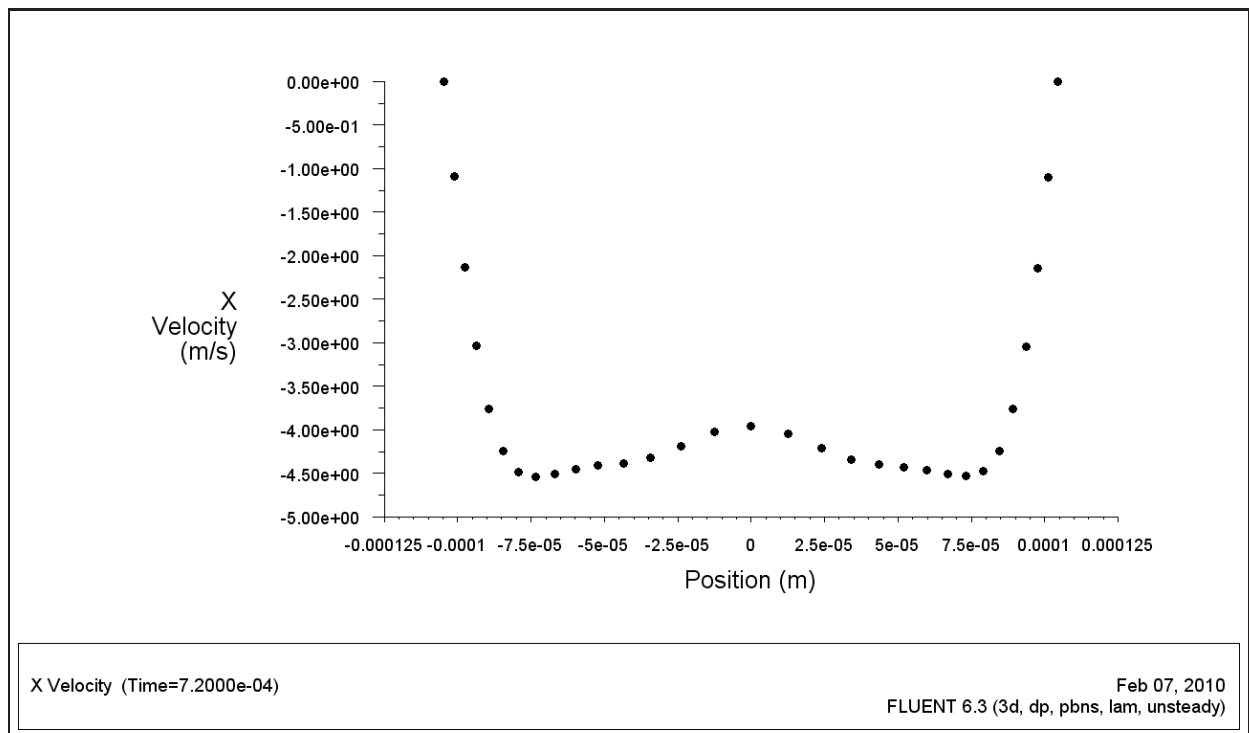


Figure 7.22: Velocity profile plot of nozzle flow in the sharpened nozzle inlet edge model near the nozzle entrance.

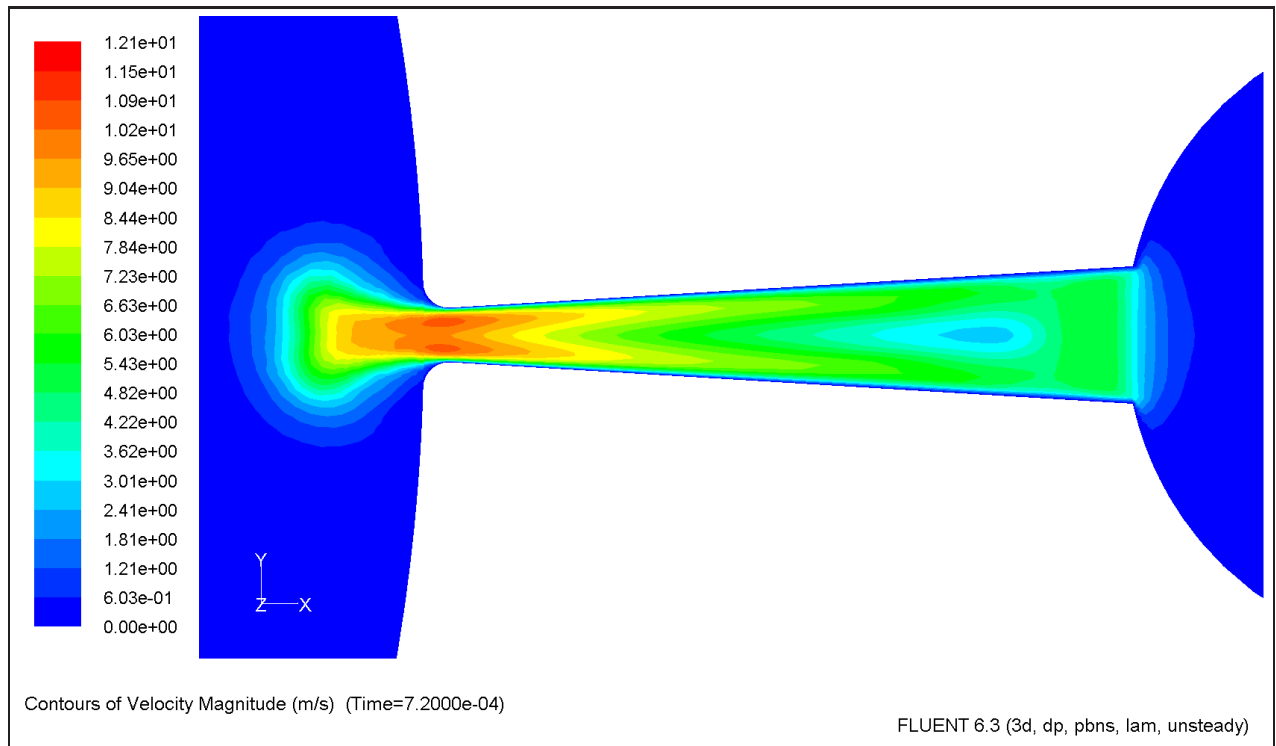


Figure 7.23: Velocity contour plot of the nozzle flow for the sharp nozzle inlet edge model.

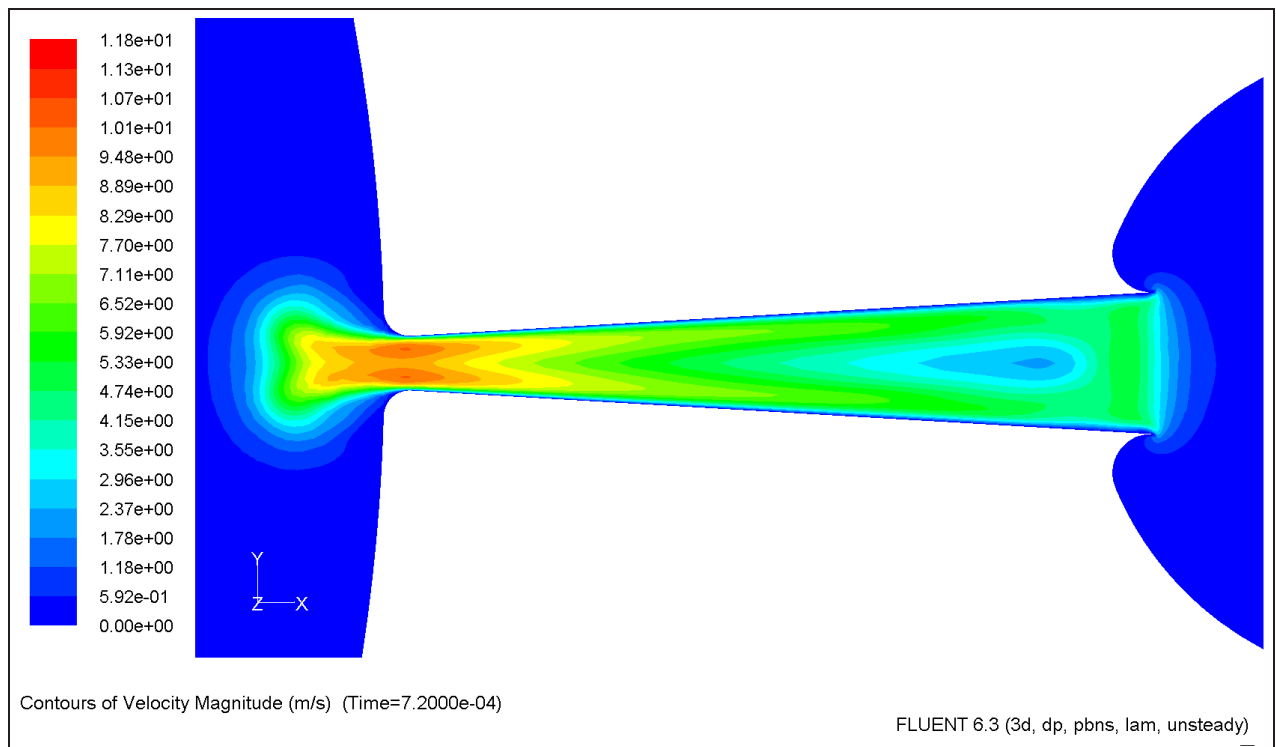


Figure 7.24: Velocity contour plot of the nozzle flow for the sharpened nozzle inlet edge model.

7.2 Frequency dependence analysis

Considering Figure 7.1 it appears as if the flowrate is independent of the frequency range between 10 Hz and 100 Hz. There is however an increase in flow rate for all models for the frequency range between 100 Hz and 1000 Hz. The flow rate is increased for this frequency range by an average of 28%. This effect can be attributed to the Roshko number derived by dimensional analysis in Section 5.4.4 and defined by Equation (7.2.1). Wang *et al.* [36] reported that these frequency effects become significant for Roshko numbers $Ro \geq 1.5$. Results however cannot compare as the characteristic length for the flow presented by Wang *et al.* [36] is undefined.

$$Ro = \frac{\rho L^2 f}{\mu} . \quad (7.2.1)$$

Using the length of the diffuser as the characteristic length L and properties of water at 20°C. The Roshko number ranges between $16 \leq Ro \leq 1686$ for the frequencies simulated. The flow is dependent on the frequency for $168 \leq Ro \leq 1686$.

Chapter 8

Conclusions and recommendations

The data presented shows that the flow is extensively laminar with a maximum Reynolds number of $Re \approx 950$. The data also shows dependency of the flow direction on variables such as inlet and outlet radii, at Reynolds numbers ranging from $1 \ll Re < 1000$. For this reason the numerical models have concentrated meshing schemes in the diffuser and nozzle region as depicted by Figure 6.7.

This dependency can be explained by large losses at the diffuser entrance due to extreme velocity gradients in this area. The losses at the entrance of the diffuser dominate diffuser losses and exit losses. This effect is illustrated in Figures 7.2, 7.23 and 7.24.

Implementing a rounded diffuser inlet throat, where the velocity gradients are large, the efficiency of the micropump is increased. Rounding the diffuser inlet also causes the boundary layer to develop more rapidly. When the flow in the diffuser is developed the velocity gradient is approximately normal to the wall of the diffuser as depicted by Figure 7.11, therefore reducing the shear force on the fluid. Compared to the sharp diffuser inlet model the absolute flow rate is improved by more than 100%. The flow in the sharp diffuser inlet model is reversed or negative, thus it's only possible to compare absolute flow rates.

The nett flow rate is further increased by adding sharper inlet edges to the nozzle flow direction, this increases flow resistance by amplifying the inlet losses. Although the velocity gradient is larger with the model without the sharpened inlet edge as depicted by Figures 7.21 and 7.22, the inlet losses dominate the flow resistance in the nozzle direction. Compared to the round diffuser inlet model the flow rate is improved by more than 30%. The effect of the alterations on the respective radii have increased the first model's absolute flow rate by more than 200%.

The frequency dependence of the micropump is plotted in Figure 7.1. The flow rate appears to be independent of the frequency when $10 \leq f \leq 100$. However a slight dependence is observed when $100 \leq f \leq 1000$. This dependence can be contributed to the Roshko number effect. Frequency dependence is important, as MEMS devices typically operate in and above the frequency range plotted by Figure 7.1. Wang *et al.* [36] reported that these frequency effects become significant for Roshko numbers $Ro \geq 1.5$. Results however cannot compare as the characteristic length for the flow presented by Wang *et al.* [36] is undefined.

8.1 Recommendations

This section discus recommendations regarding further simulations and manufacturing options.

8.1.1 Further analyses

Examining the expression in 5.4.15, it is clear that there are numerous possibilities for further analyses. One such a possibility is to investigate the effects of the diffuser angle α on the flow resistance of the diffuser at various Reynolds numbers. Another possibility will be to investigate the effects on the flow rate by varying the length of the diffuser with the inlet aspect ratio.

This investigation also makes little mention of the operating pressure of the micropump, for future work it can be suggested that a flow rate vs pressure plot be constructed.

8.1.2 Manufacturing recommendations

Manufacturing for this project was problematic. The micropump requires a membrane to seal the pump chamber and to exert a pressure on the fluid. Therefore a membrane needs to be bonded to the base that contains the pump chamber and channels. This step requires special laboratories, processes and materials to do properly and avoid blocking the microchannels. These processes have only recently became readlily available in South Africa. Unfortunately the time for the project elapsed. Thus manufacturing will be possible for further investigations in the future. Manufacturing done is presented in Appendics A.1.

List of References

- [1] Wang, W. and Soper, S.: *Bio-MEMS Technologies and Applications*. CRC Press, Taylor & Francis Group, 2007. (Cited on pages viii, 1, 11, 14, 15, 31, and 39.)
- [2] Zeng, S., Chen, C., Jr., J.M. and Santiago, J.: Fabrication and characterization of electroosmotic micropumps. *Sensors and Actuators B*, vol. 79, pp. 107–114, 2001. (Cited on pages viii, 13, and 15.)
- [3] Chollet, F. and Liu, H.: *A (not so) short Introduction to Micro Electromechanical Systems*, vol. 2.1. Creative Commons, July 2007. (Cited on pages viii, 16, 17, 19, 20, and 29.)
- [4] Gerlach, T., Schuenemann, M. and Wurmus, H.: A new micropump principle of the reciprocating type using pyramidal micro flow channels as passive valves. *Journal of Micromechanics and Micro-engineering*, vol. 5, pp. 199–201, 1995. (Cited on pages viii, xii, 11, and 18.)
- [5] MEMS, June 2008.
Available at: http://www.cs.ualberta.ca/~database/MEMS/sma_mems/mems.html
(Cited on pages viii and 22.)
- [6] Aumeerally, M.: *Analytic Model Derivation of Microfluidic Flow for MEMS Virtual-Reality CAD*. Master's thesis, School of Information and Communication Technology, Faculty of Engineering and Information Communication Technology, Griffith University, Queensland, Australia, 2004. (Cited on pages viii, ix, 32, and 35.)
- [7] Olsson, A.: *Valve-Less Diffuser Pumps for Liquids*. Master's thesis, Instrumentation Laboratory, Department of Signals, Sensors and Systems, Royal Institute of Technology, Stockholm, 1996. (Cited on pages ix and 35.)
- [8] Runstadler, P., Dolan, F. and Dean, R.: Diffuser data book. Tech. Rep., Create Inc. Science and Technology, 1975. (Cited on pages ix, 34, 36, 41, and 43.)
- [9] White, E.: *Fluid Mechanics*. McGraw-Hill international Editions, 1986. (Cited on pages ix, 27, 30, 31, 34, 35, 36, and 39.)
- [10] Singhal, V., Garimella, S. and Murthy, J.: Low reynolds number flow through nozzle-diffuser elements in valveless micropumps. *Sensors and Actuators*, vol. A 113, pp. 226 – 235, 2003. (Cited on pages ix, 39, 40, 42, and 44.)
- [11] Stemme, E. and Stemme, G.: A valve-less diffuser / nozzle based fluid pump. *Sensors and Actuators*, vol. A39, pp. 159–167, 1993. (Cited on pages xii, 5, and 11.)
- [12] Lammerink, T., Elwenspoek, M. and Fluitman, J.: Integrated micro-liquid dosing system. In: *IEEE 6th International Workshop on Micro Electro Mechanical Systems (MEMS'93), Fort Lauderdale, Florida, USA*. February 7-10, 1993. (Cited on pages xii and 11.)

- [13] Zengerle, R., Richter, A. and Sandmaier, H.: A micromembrane pump with electrostatic actuation. In: *IEEE 5th International Workshop on Micro Electro Mechanical Systems (MEMS'92), Travemunde, Germany*. February 4-7, 1992. (Cited on pages xii and 11.)
- [14] Shoji, S., Nakafawa, S. and Esashi, M.: Micropump and sample-injector for integrated chemical analyzing systems. *Sensors and Actuators*, vol. A21-A23, pp. 189–192, 1990. (Cited on pages xii and 11.)
- [15] van de Pol, F., van Lintel, H., Elwenspoek, M. and Fluitman, J.: A thermopneumatic micropump based on micro-engineering techniques. *Sensors and Actuators*, vol. A21-A23, pp. 198–202, 1990. (Cited on pages xii and 11.)
- [16] van Lintel, H., van den Pol, F. and Bouwstra, S.: A piezoelectric micropump based on micromachining in silicon. *Sensors and Actuators*, vol. 15, pp. 153–167, 1988. (Cited on pages xii and 11.)
- [17] Smits, J.: Piezoelectric micropump with three valves working peristaltically. *Sensors and Actuators*, vol. vA21-A23, pp. 203–206, 1990. (Cited on pages xii and 11.)
- [18] Mizoguchi, H., Ando, M., Mizuno, T., Takagi, T. and Nakajima, N.: Design and fabrication of light driven micropump. In: *IEEE 5th International Workshop on Micro Electro Mechanical Systems (MEMS'92), Travemunde, Germany*. February 4-7, 1992. (Cited on pages xii and 11.)
- [19] Ahn, C. and Allen, M.: Fluid micropumps based on rotary magnetic actuators. In: *IEEE 8th International Workshop on Micro Electro Mechanical Systems (MEMS'95), Amsterdam, the Netherlands, Jan. 29-Feb. 2*. 1995. (Cited on pages xii and 11.)
- [20] Feynman, R.: There is plenty of room at the bottom. In: *Caltech's Engineering and Science Magazine*. 1960. (Cited on page 1.)
- [21] el Hak, M.G.: *MEMS - Introduction and Fundamentals, The MEMS Handbook, Second Edition*. CRC Press, Taylor & Francis Group, 2006. (Cited on pages 1, 3, 33, 34, and 40.)
- [22] Tay, F. (ed.): *Microfluidics and BioMEMS Applications*. Kluwer Academic Publishers, 2002. (Cited on pages 1, 5, and 13.)
- [23] South Africa HIV and AIDS statistics, October 2008.
Available at: <http://www.avert.org/safricastats.htm> (Cited on page 2.)
- [24] el Hak, M.G.: *MEMS - Applications, The MEMS Handbook, Second Edition*. CRC Press, Taylor & Francis Group, 2006. (Cited on page 3.)
- [25] Microfluidics and microsystems executive review, October 2008.
Available at: http://www.memsinvestorjournal.com/2006/08/biomems_has_bee.html
(Cited on page 4.)
- [26] Olsson, A., Stemme, G. and Stemme, E.: Numerical and experimental studies of flat-walled diffuser elements for valve-less micropumps. *Sensors and Actuators*, vol. 84, pp. 165–175, 1998. (Cited on pages 13, 27, 39, 44, and 59.)
- [27] Enderle, J., Blanchard, S. and Bronzino, J.: *Introduction to Biomedical Engineering*. Elsevier Academic Press, 2005. (Cited on page 16.)
- [28] el Hak, M.G.: *MEMS - Design and Fabrication, The MEMS Handbook, Second Edition*. CRC Press, Taylor & Francis Group, 2006. (Cited on page 17.)

- [29] Senturia, S.: *Microsystem Design*. Springer Science+Business Media,LCC, 2001. (Cited on pages 19, 20, and 21.)
- [30] Schetz, J. and Fuhs, A. (eds.): *Fundamentals of Fluid Mechanics*. John Wiley & Sons, Inc, 1999. (Cited on pages 30, 31, and 34.)
- [31] Crowe, C., Elger, D. and Roberson, J.: *Engineering Fluid Mechanics*. John Wiley and Sons, Inc, 2001. (Cited on pages 30, 31, and 34.)
- [32] White, E.M.: *Viscous Fluid Flow*. McGraw-Hill, 2006. (Cited on pages 30, 35, 36, and 37.)
- [33] Lindfield, G. and Penny, J.: *Numerical Methods using Matlab®*. Prentice Hall, 2000. (Cited on page 37.)
- [34] Jiang, X., Zhou, Z., Huang, X., Li, Y., Y.Yang and Liu, C.: Micronozzle/diffuser flow and its application in micro valveless pumps. *Sensors and Actuators*, vol. A 70, pp. 81–87, 1998. (Cited on pages 39 and 40.)
- [35] Olsson, A., Stemme, G. and Stemme, E.: Diffuser-element design investigation for valve-less pumps. *Sensors and Actuators*, vol. A 57, pp. 137–143, 1996. (Cited on page 39.)
- [36] Wang, Y., Hsu, J., Kuo, P. and Lee, Y.: Loss characteristics and flow rectification property of diffuser valves for micropump applications. *International Journal of Heat and Mass Transfer*, vol. 52, pp. 328–336, 2009. (Cited on pages 39, 40, 75, and 76.)
- [37] Buckingham, E.: On physically similar systems: Illustrations of the use of dimensional equations. *Phys. Rev.*, vol. 4, pp. 345–376, 1914. (Cited on page 42.)

Appendix A

Appendices

A.1 Manufacturing of micropump

This chapter details the manufacturing of the valveless micropump as designed and simulated in previous sections. Local manufacturing capabilities are limited and bonding techniques of surfaces on a micro scale is material specific. The proposed solution for the manufacturing is depicted in Figure A.1.

The material used is Perspex. The material is micro milled as depicted in Figure A.1. The micro milling machine used is a CNC machine with a $25\mu\text{m}$ diameter flat milling tool. The finalized product is shown in Figures A.2 and A.3.

The bonding process depicted in Figure A.1 is however not finalized as the process is complex and manufacturing resources was limited.

A.2 Non-dimensionalised Navier-Stokes equation

Considering the Navier-Stokes equation as given by

$$\rho \left(\frac{\partial \mathbf{v}}{\partial t} + \mathbf{v} \cdot \nabla \mathbf{v} \right) = -\nabla p + \mu \nabla^2 \mathbf{v} + \mathbf{f}. \quad (\text{A.2.1})$$

Each term in the above equation has the units of a volume force or, equivalently, an acceleration times a density. Each term is thus dependent on the exact measurements of a flow. When rendering the equation nondimensional, a form which does not depend directly on the physical sizes is produced. One possible way to obtain a nondimensional equation is to multiply the equation by the following factor:

$$\frac{D}{\rho V^2}, \quad (\text{A.2.2})$$

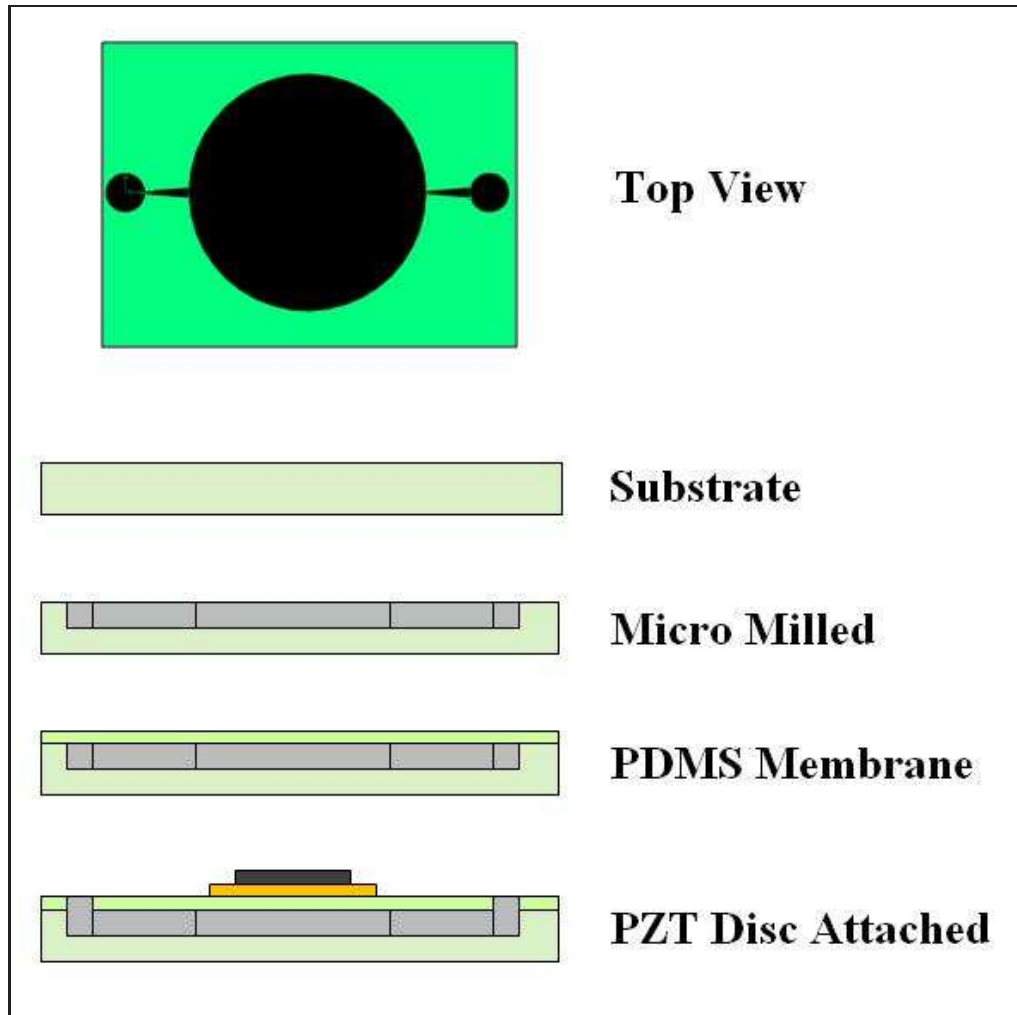


Figure A.1: Proposed manufacturing solution.

where the symbols are the same as those used in the definition of the Reynolds number. Then

$$\begin{aligned}
 \mathbf{v}' &= \frac{\mathbf{v}}{V} , \\
 p' &= p \frac{1}{\rho V^2} , \\
 \mathbf{f}' &= \mathbf{f} \frac{D}{\rho V^2} , \\
 \frac{\partial}{\partial t'} &= \frac{D}{V} \frac{\partial}{\partial t} , \\
 \nabla' &= D \nabla .
 \end{aligned} \tag{A.2.3}$$

Rewriting the Navier-Stokes equation without dimensions as

$$\frac{\partial \mathbf{v}'}{\partial t'} + \mathbf{v}' \cdot \nabla' \mathbf{v}' = -\nabla' p' + \frac{\mu}{\rho D V} \nabla'^2 \mathbf{v}' + \mathbf{f}' , \tag{A.2.4}$$

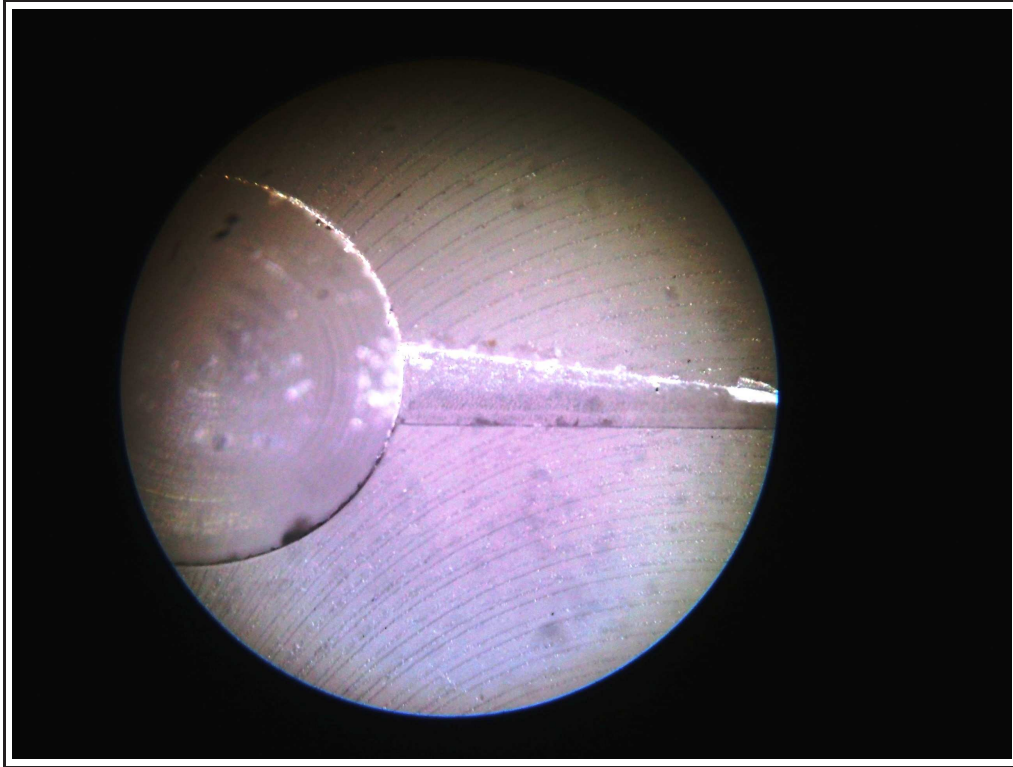


Figure A.2: The diffuser and outlet of the micropump under 20× magnification.

and

$$\frac{\mu}{\rho DV} = \frac{1}{\text{Re}} . \quad (\text{A.2.5})$$

Simplifying the non-dimensionalised equation as

$$\frac{\partial \mathbf{v}}{\partial t} + \mathbf{v} \cdot \nabla \mathbf{v} = -\nabla p + \frac{1}{\text{Re}} \nabla^2 \mathbf{v} + \mathbf{f} . \quad (\text{A.2.6})$$

This is why mathematically all flows with the same Reynolds number are comparable.

A.3 Pressure contour plots

Figures A.4 and A.5 depicts the pressure gradients in the middle plane of the micropump for the rounded diffuser inlet edge and sharpened nozzle inlet edge model. Negative pressure can be observed at the entrance of the diffuser, causing backflow in the diffuser. Flow development is depicted by Figures A.6 - A.12. Plots were made every 12 time steps. Each time stem is $\Delta t = 0.01$ ms.

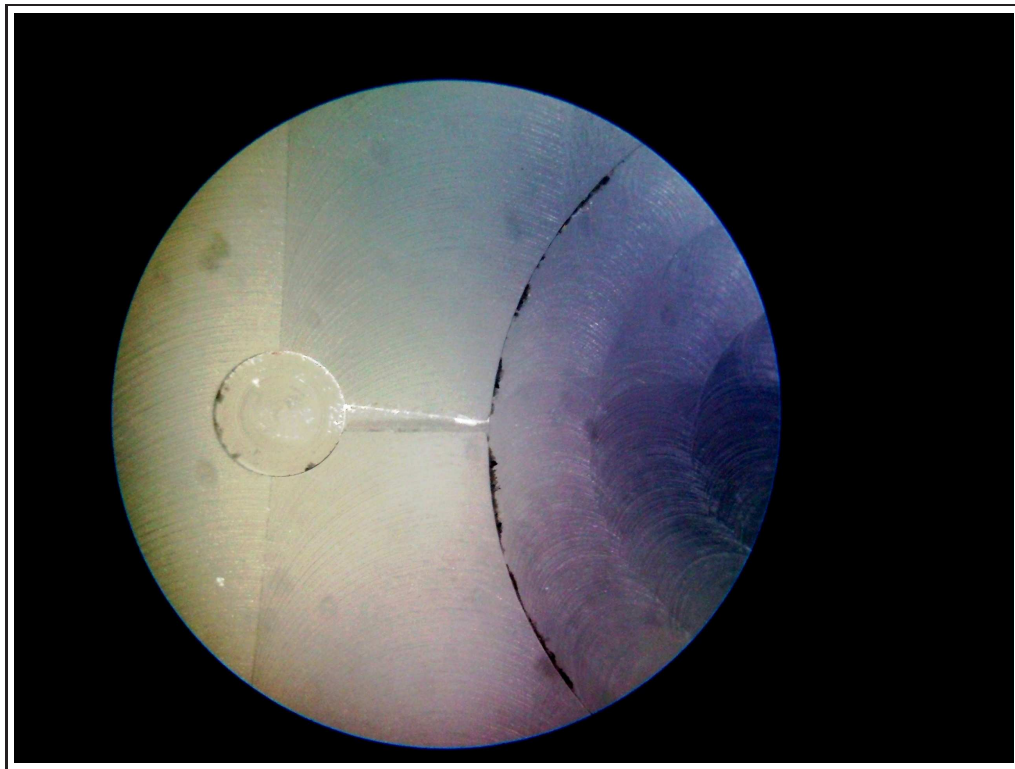


Figure A.3: The top of the diffuser / nozzle, viewed with 20× magnification.

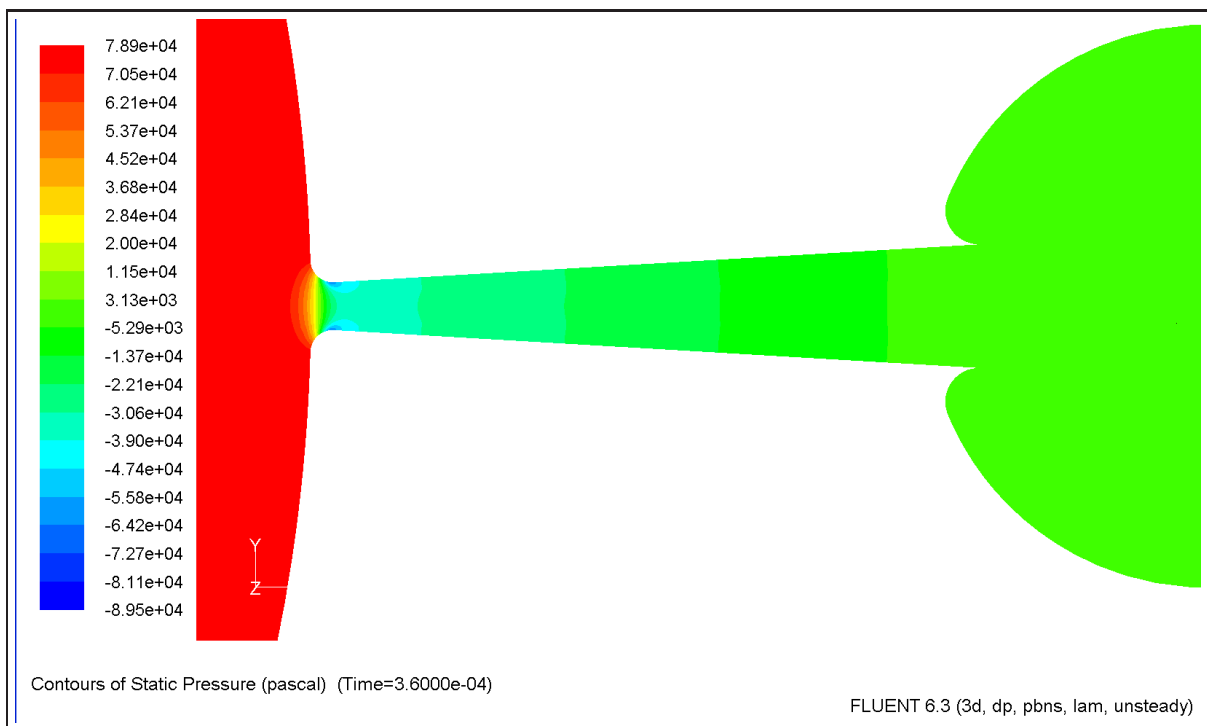


Figure A.4: Pressure contour plot of diffuser flow.

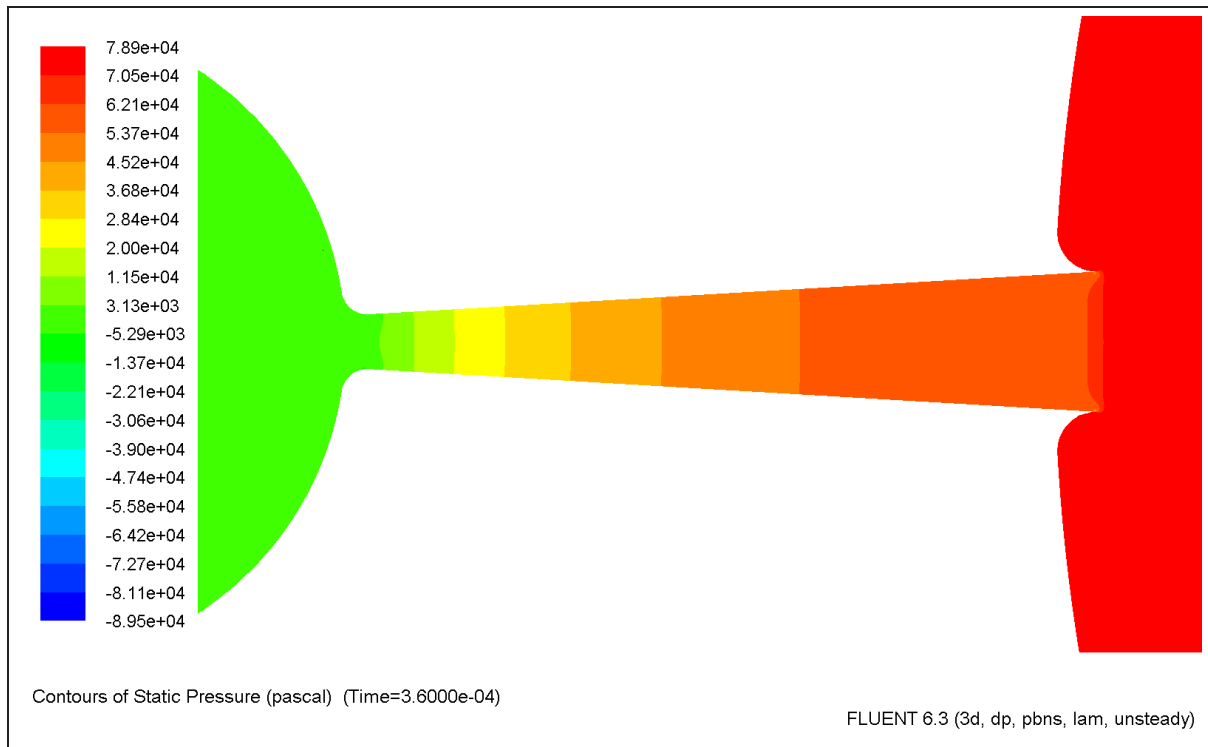


Figure A.5: Pressure contour plot of nozzle flow.

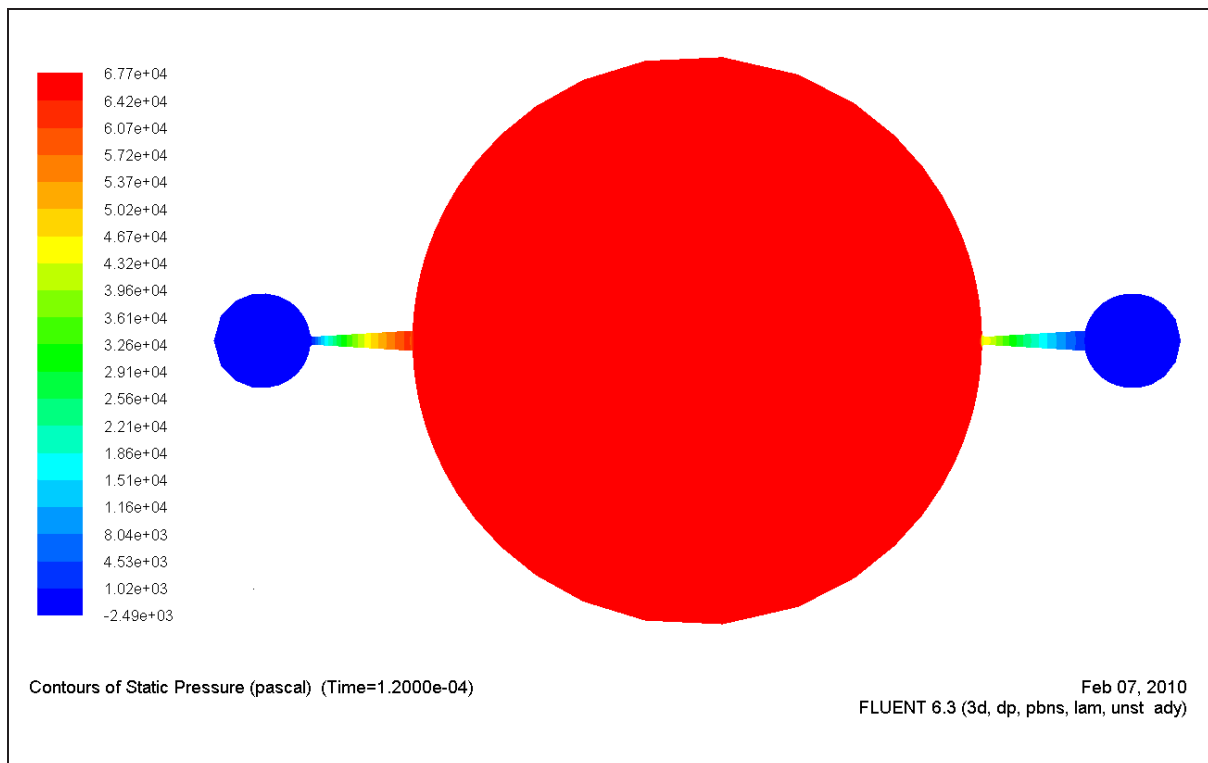


Figure A.6: Pressure contour plot @ 1 kHz.

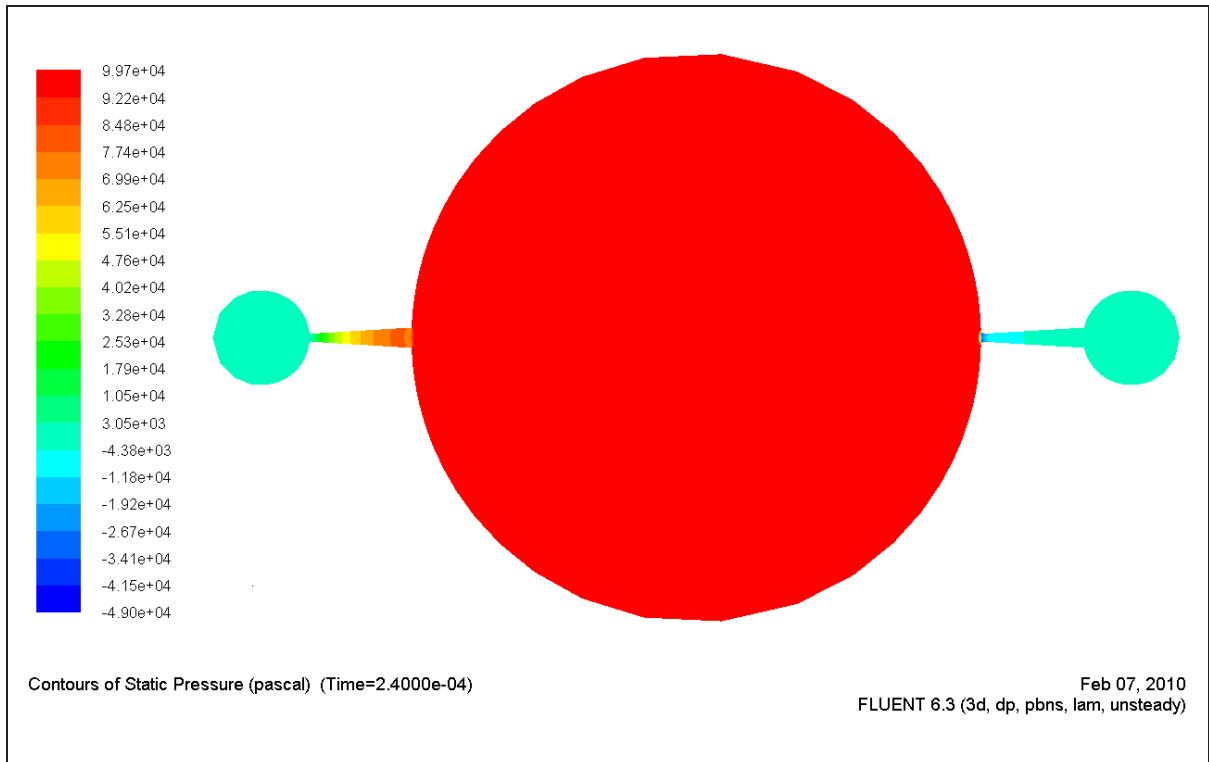


Figure A.7: Pressure contour plot @ 1 kHz.

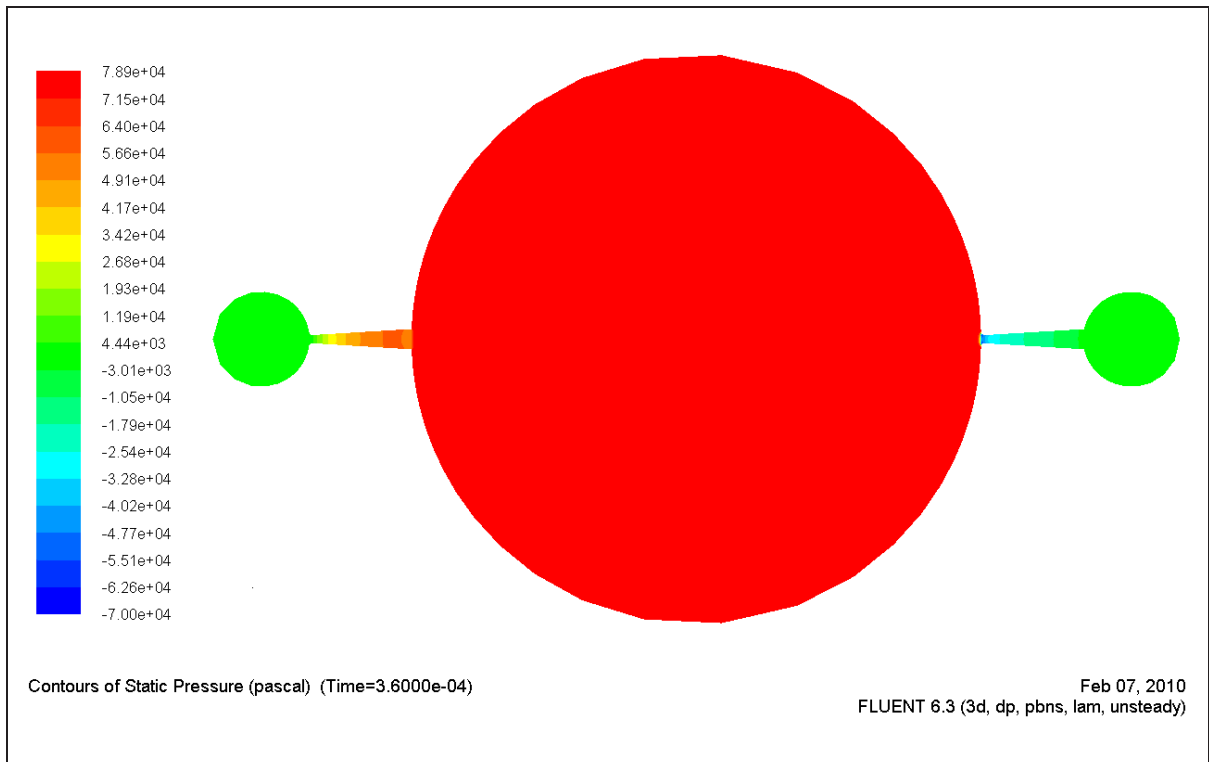


Figure A.8: Pressure contour plot @ 1 kHz.

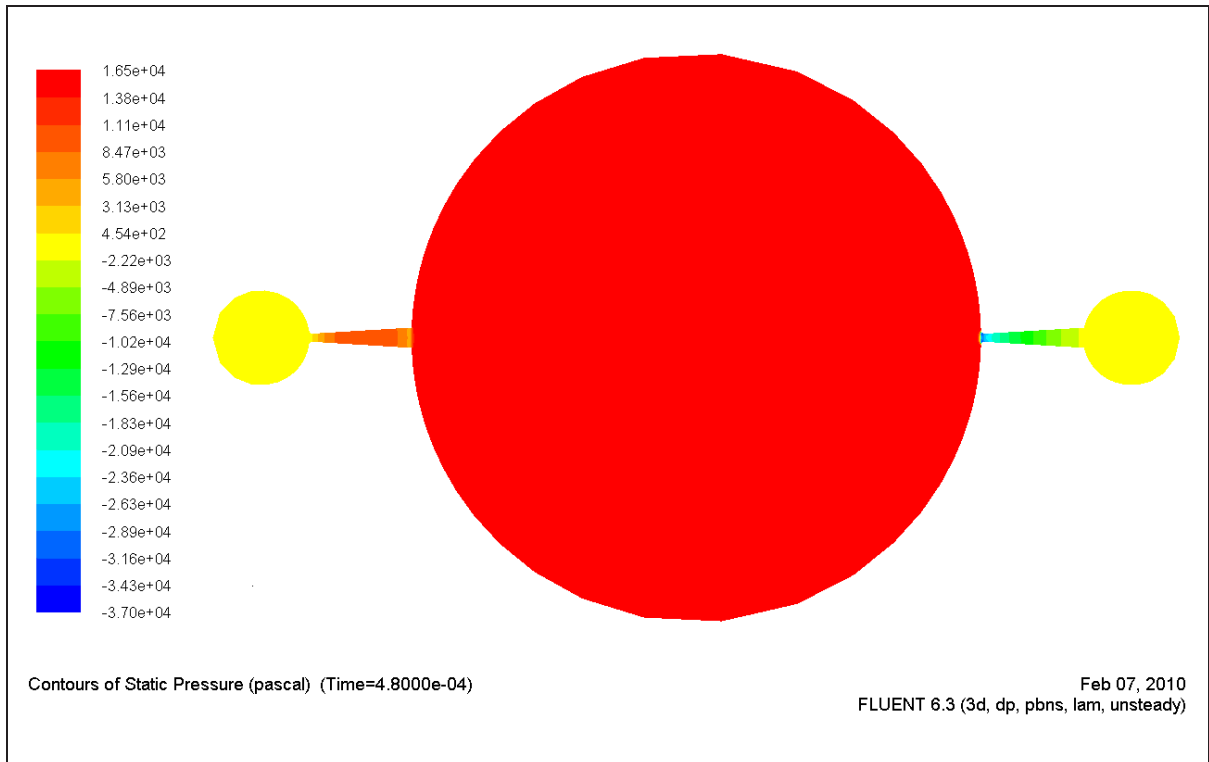


Figure A.9: Pressure contour plot @ 1 kHz.

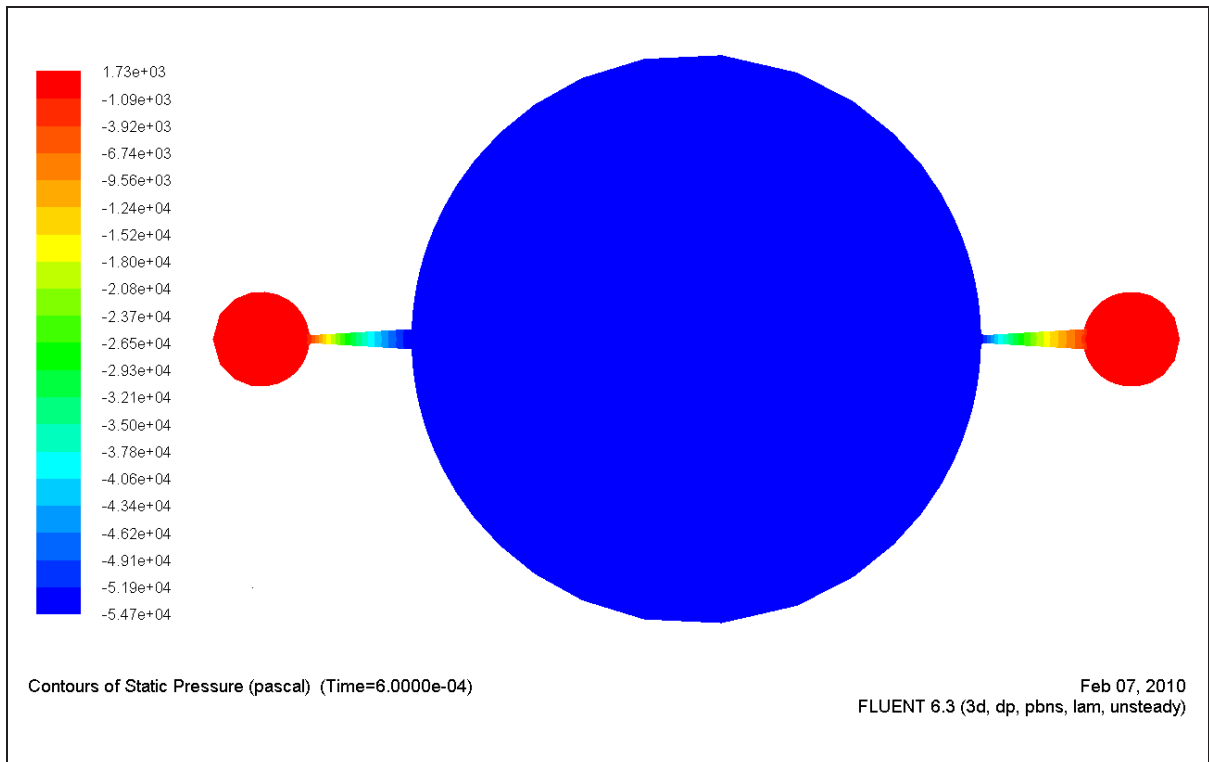


Figure A.10: Pressure contour plot @ 1 kHz.

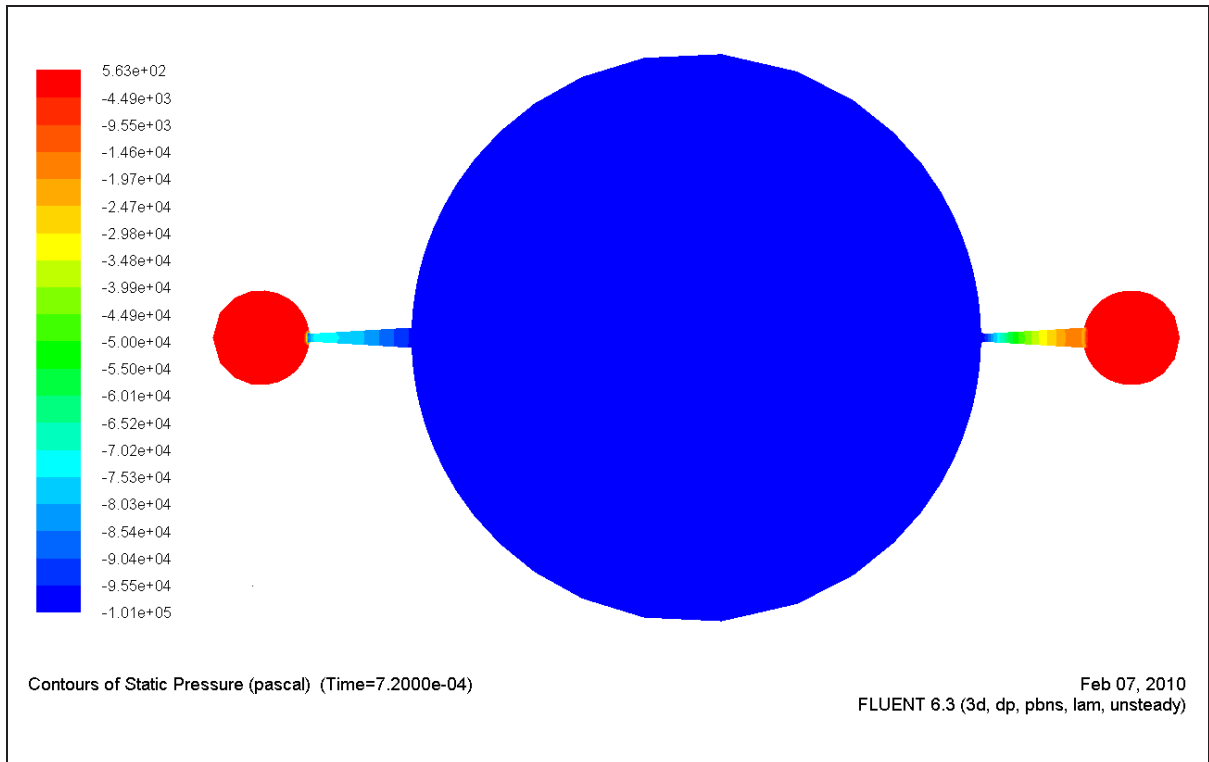


Figure A.11: Pressure contour plot @ 1 kHz.

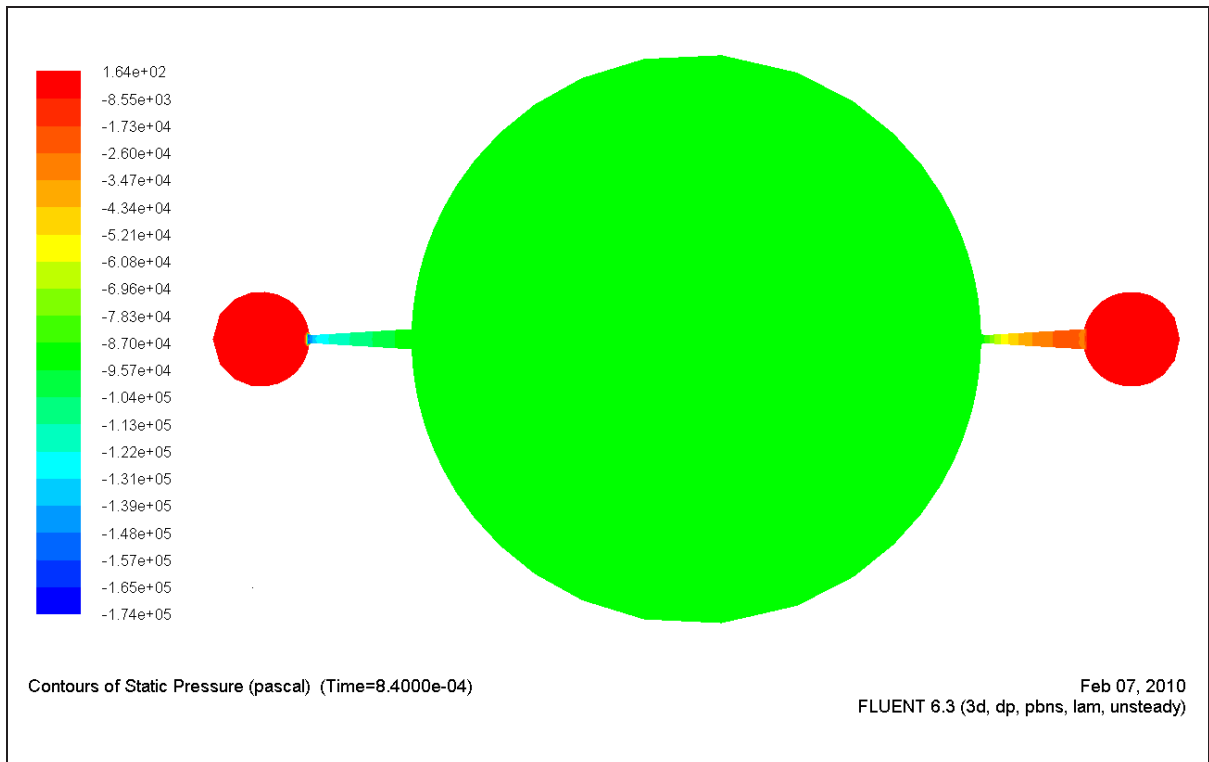


Figure A.12: Pressure contour plot @ 1 kHz.

A.4 Velocity contour plots

Flow development as depicted Figures A.13-A.19 shows velocity contour plots for one cycle @ 1 kHz. Plots were made every 12 time steps. Each time stem is $\Delta t = 0.01$ ms.

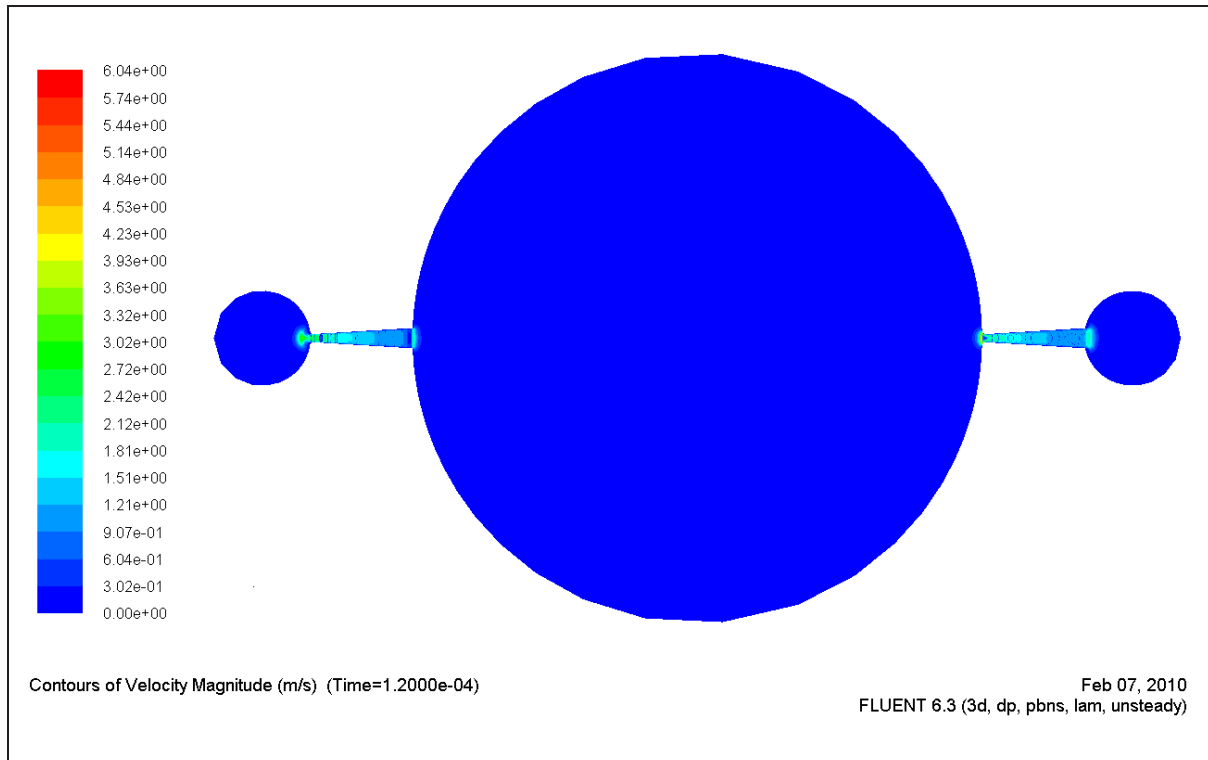


Figure A.13: Velocity magnitude contour plot @ 1 kHz.

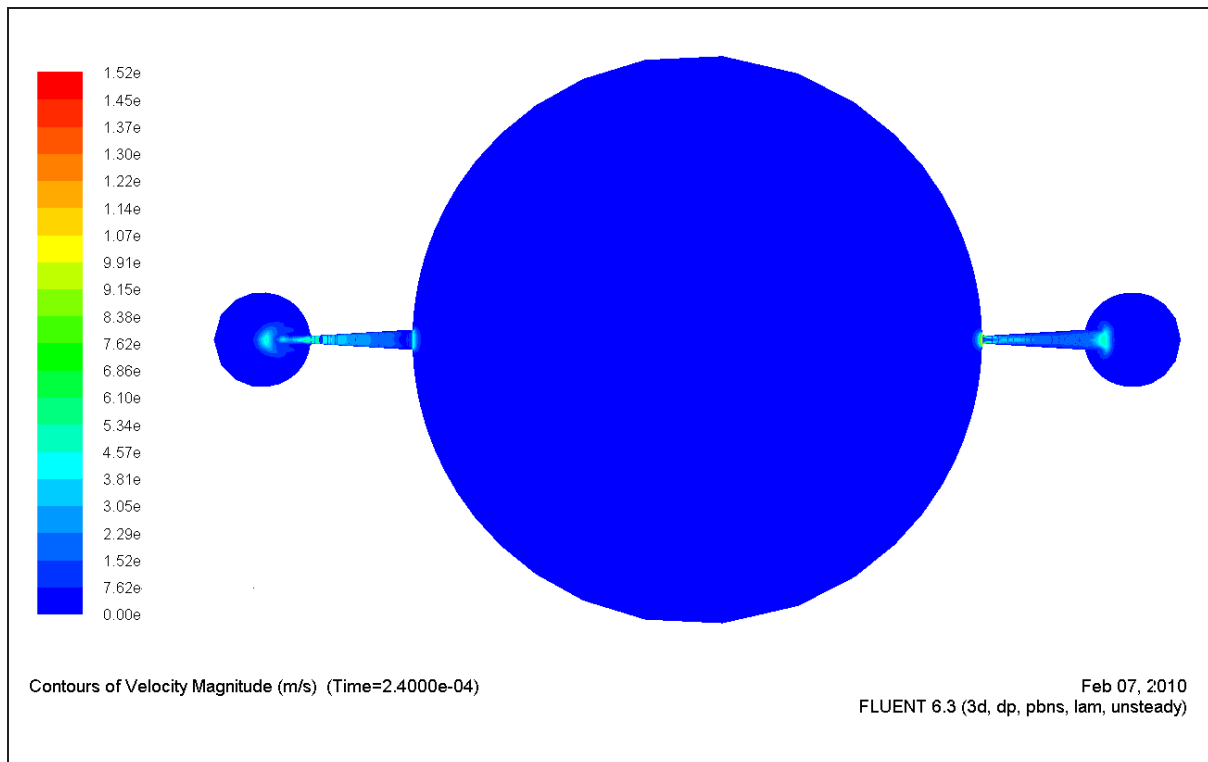


Figure A.14: Velocity magnitude contour plot @ 1 kHz.

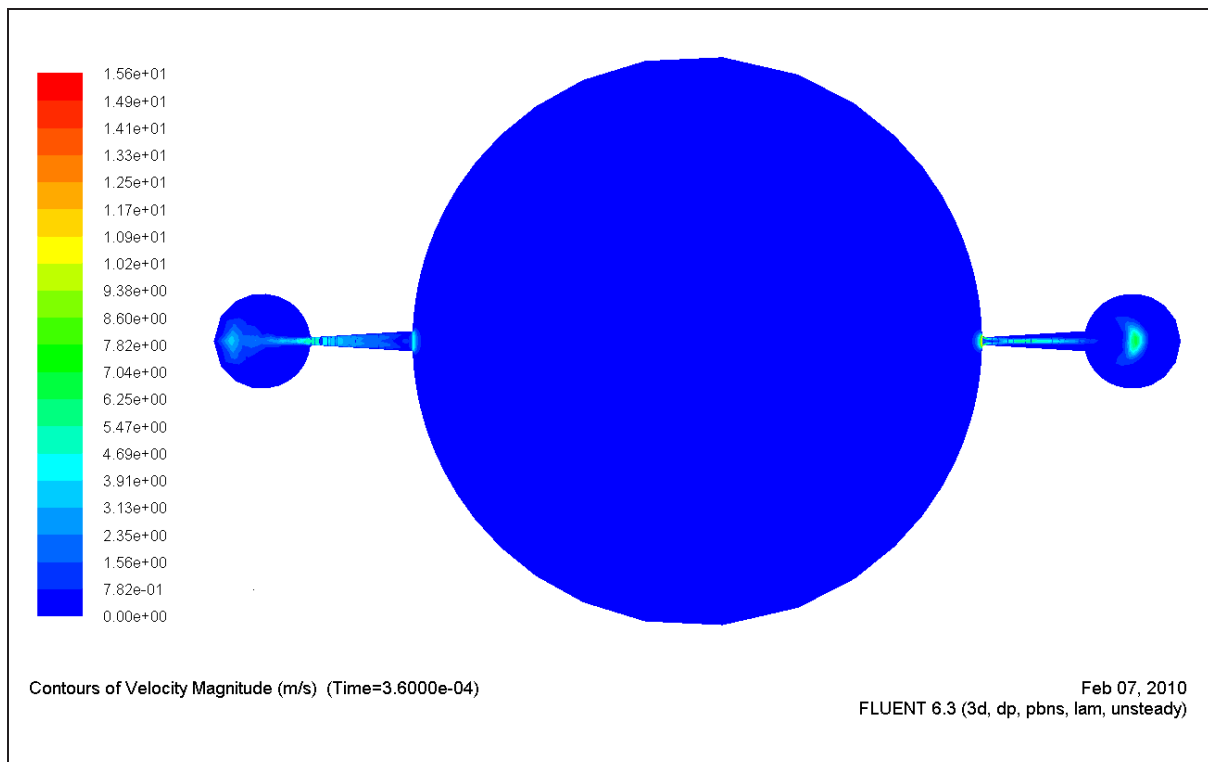


Figure A.15: Velocity magnitude contour plot @ 1 kHz.

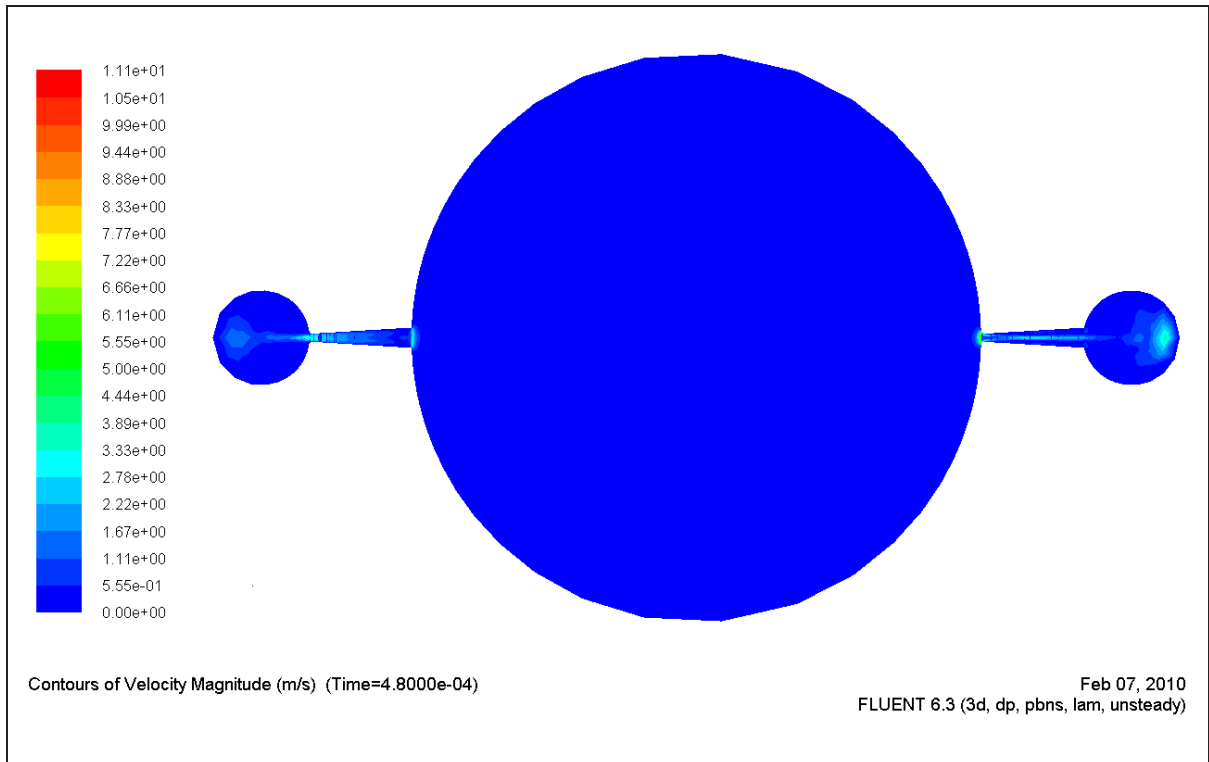


Figure A.16: Velocity magnitude contour plot @ 1 kHz.

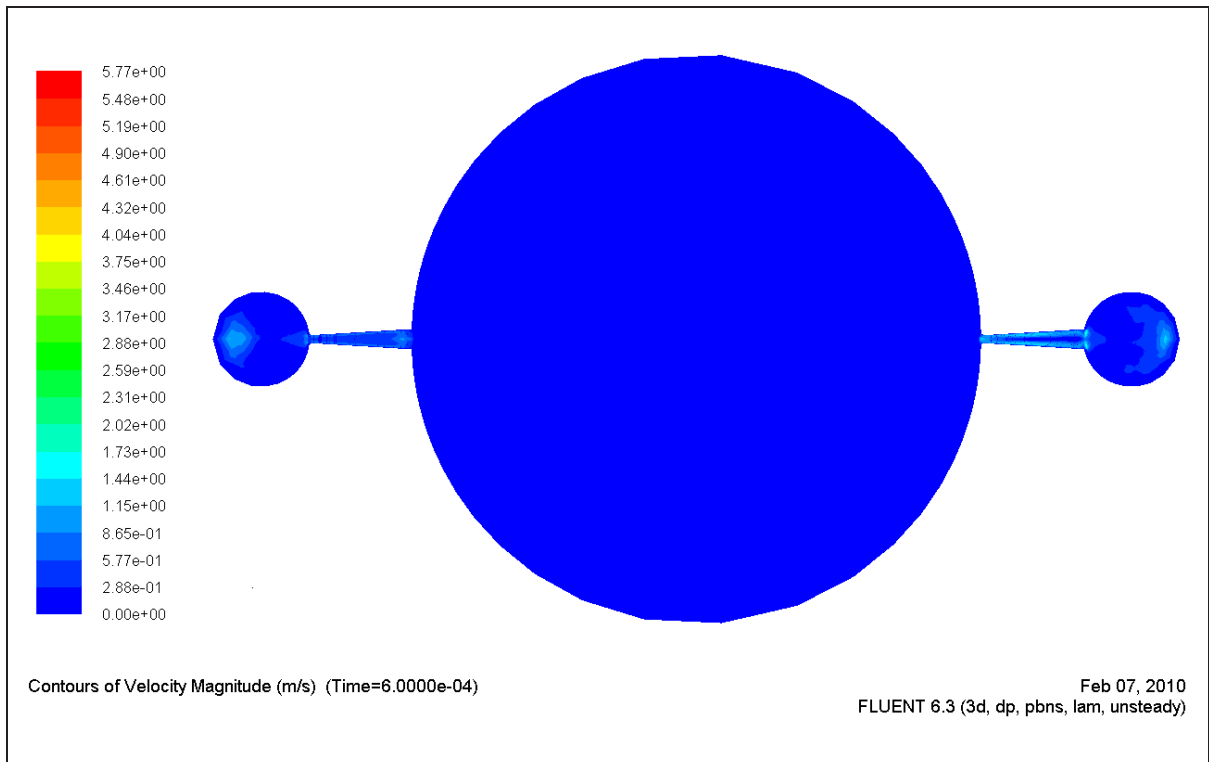


Figure A.17: Velocity magnitude contour plot @ 1 kHz.

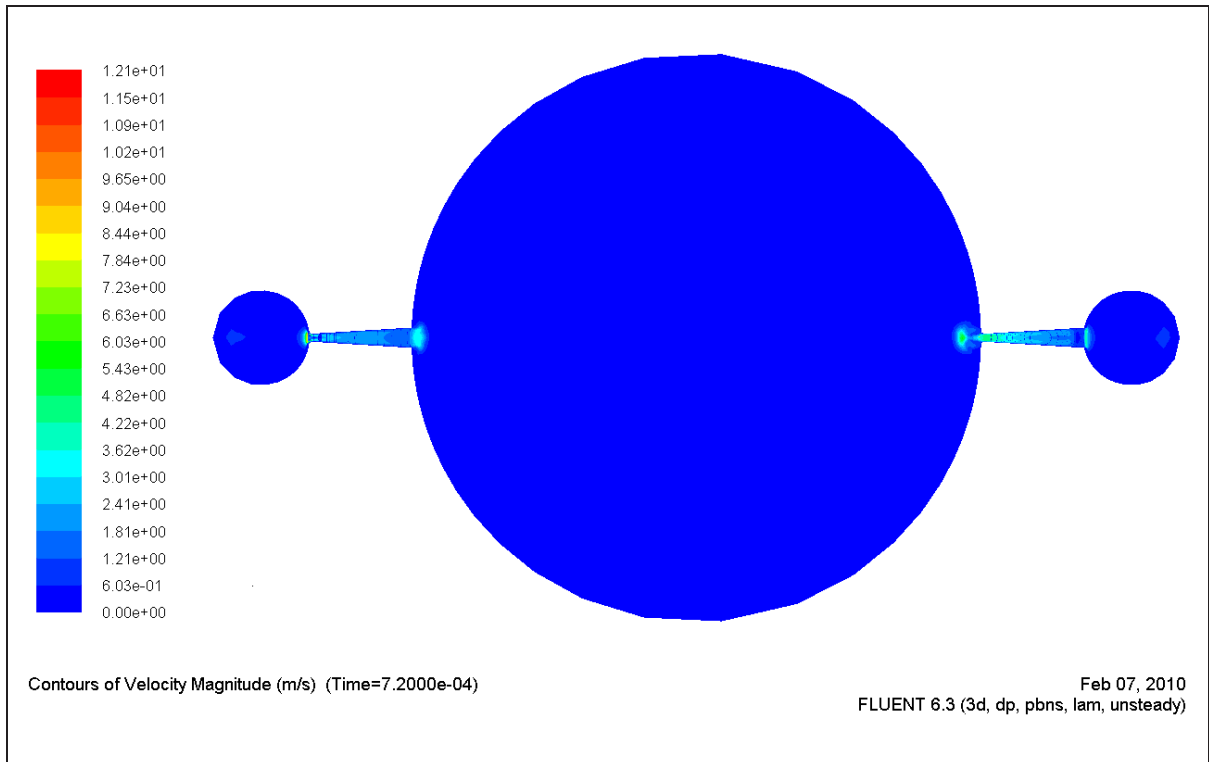


Figure A.18: Velocity magnitude contour plot @ 1 kHz.

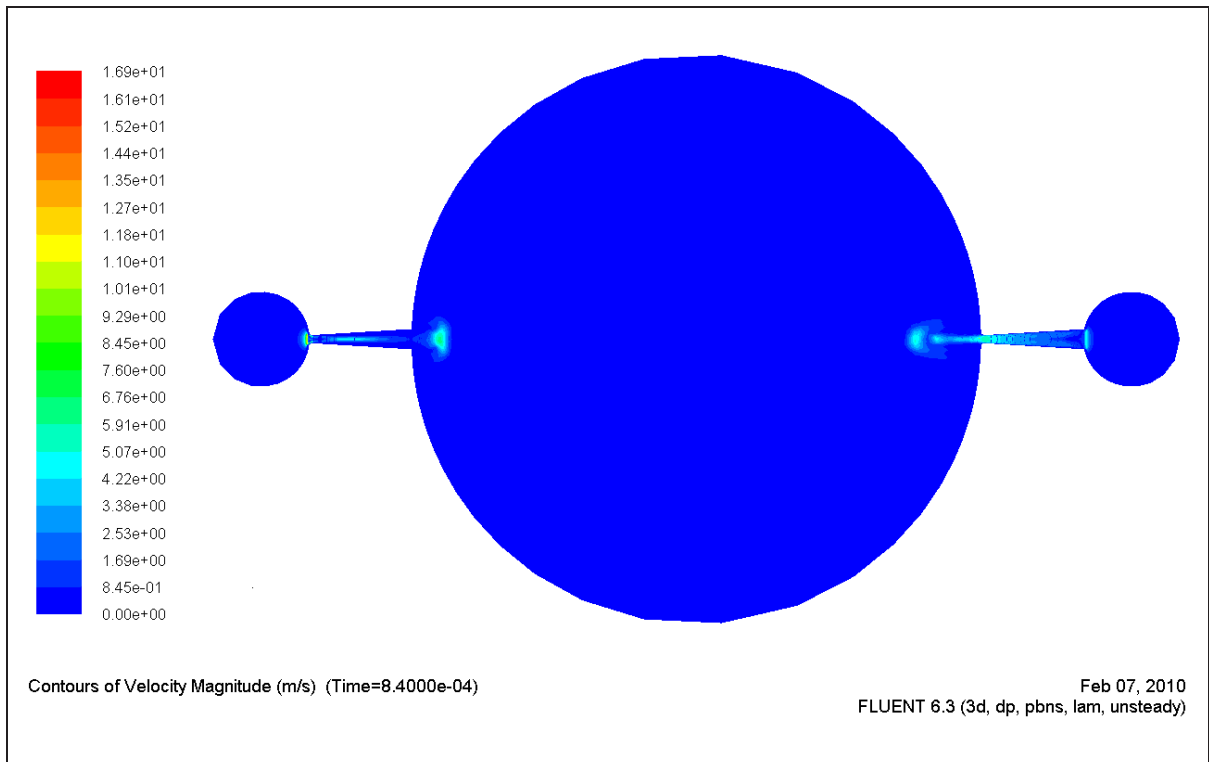


Figure A.19: Velocity magnitude contour plot @ 1 kHz.

A.5 Velocity profiles during flow cycle

Figures A.20 - A.26 depicts the velocity profiles during a flow cycle near the diffuser exit. Plots were made every 12 time steps. Each time stem is $\Delta t = 0.01$ ms.

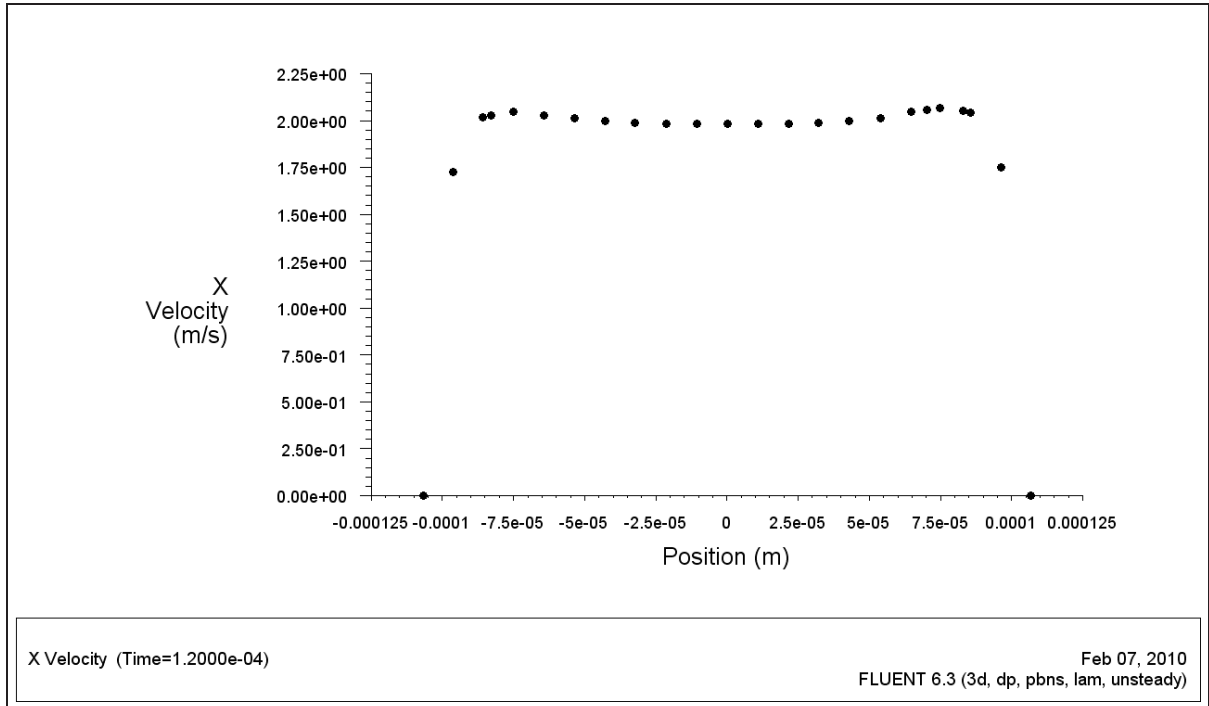


Figure A.20: Velocity profile in diffuser @ 1 kHz.

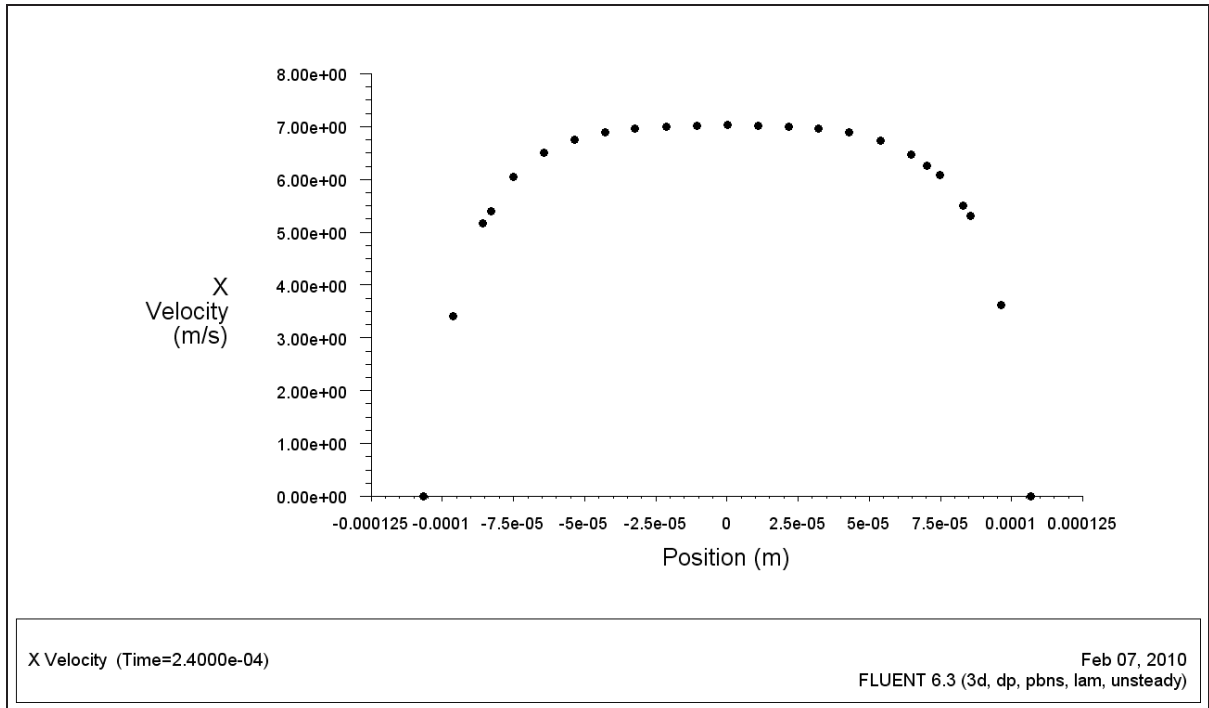


Figure A.21: Velocity profile in diffuser @ 1 kHz.

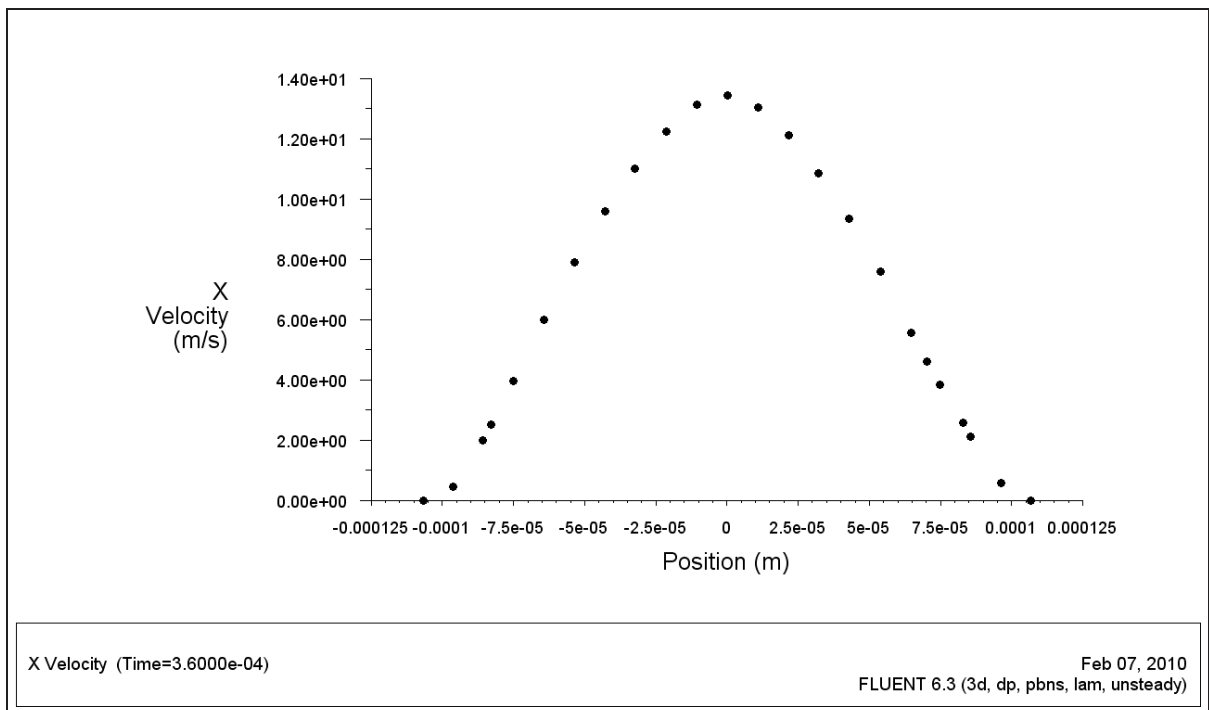


Figure A.22: Velocity profile in diffuser @ 1 kHz.

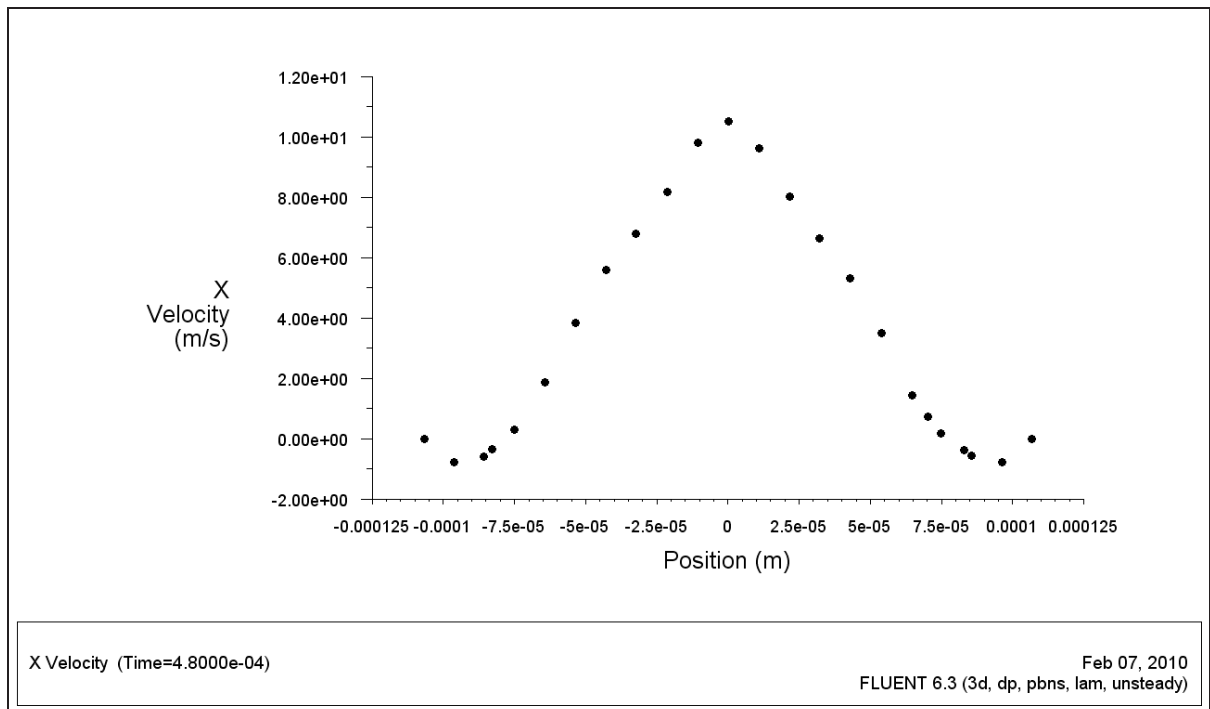


Figure A.23: Velocity profile in diffuser @ 1 kHz.

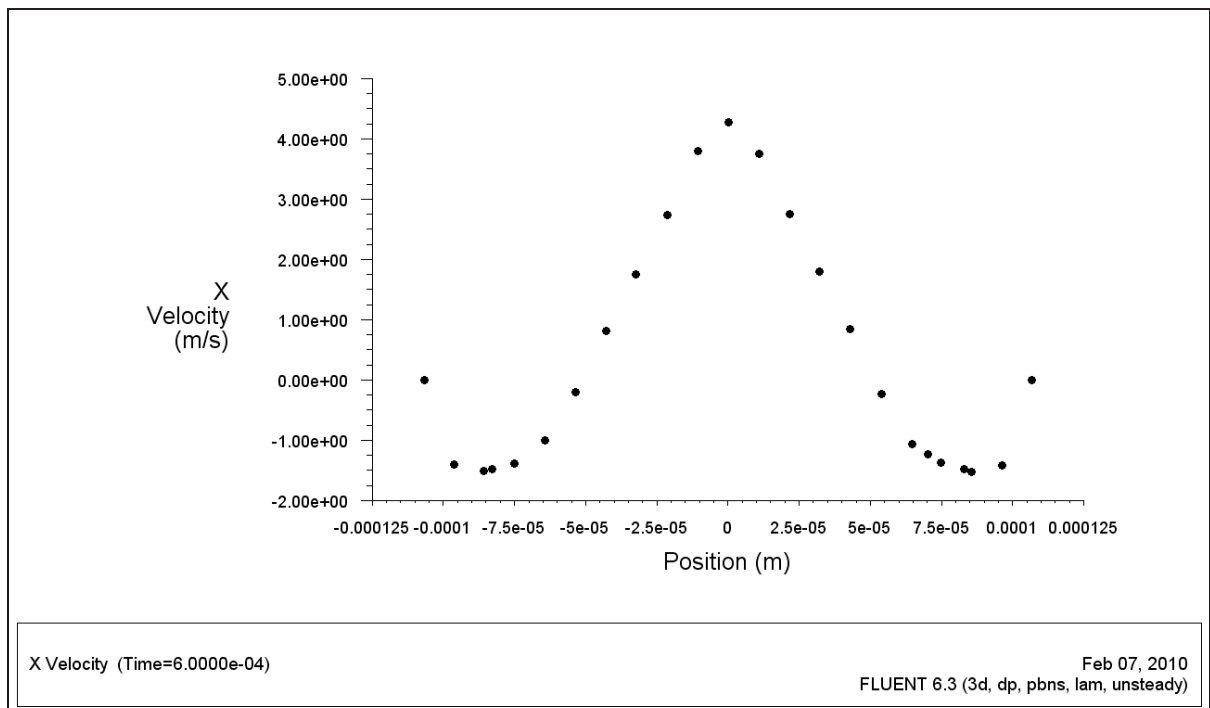


Figure A.24: Velocity profile in diffuser @ 1 kHz.

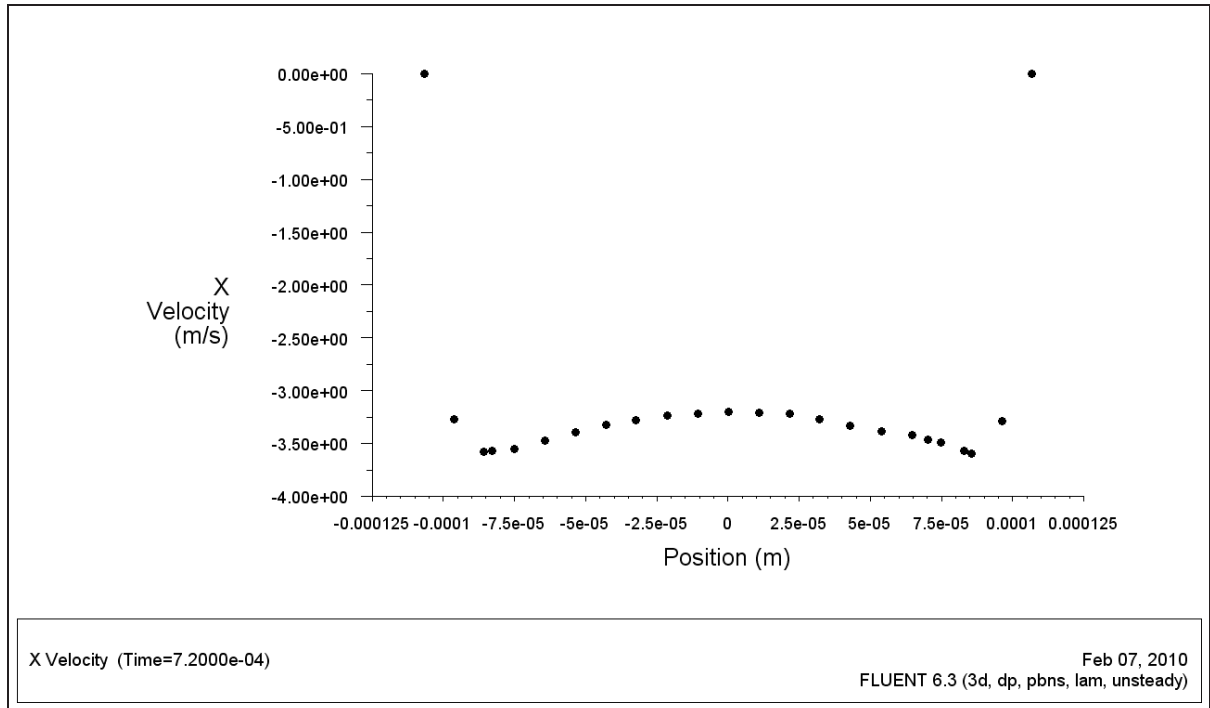


Figure A.25: Velocity profile in diffuser @ 1 kHz.

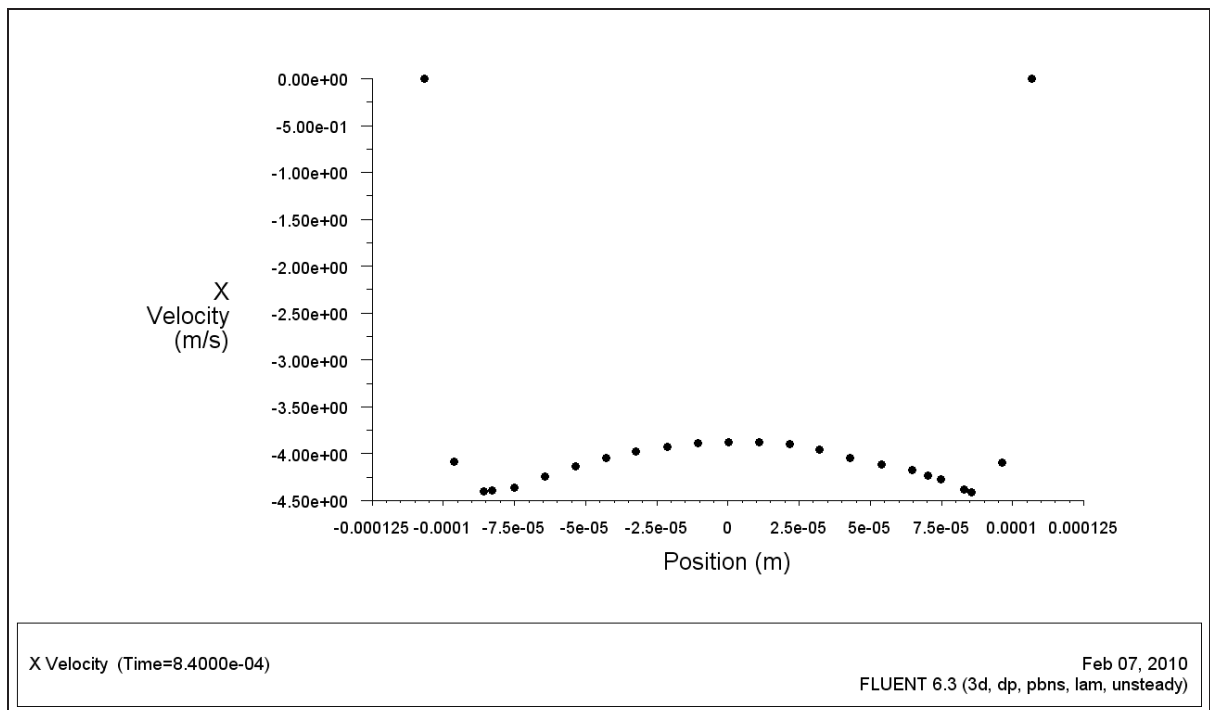


Figure A.26: Velocity profile in diffuser @ 1 kHz.